TIME INVARIANT MODELING OF HIGHER ORDER DC-DC CONVERTERS

by

LEI NIU

Presented to the Faculty of the Graduate School of

The University of Texas at Arlington in Partial Fulfillment

of the Requirements

for the Degree of

MASTER OF SCIENCE IN ELECTRICAL ENGINEERING

THE UNIVERSITY OF TEXAS AT ARLINGTON

May 2012

ACKNOWLEDGEMENTS

I would like to first thank my graduate advisor, Dr. Ali Davoudi, for offering me the opportunity and financial support to study in Renewable Energy and Vehicular Technology Lab at the University of Texas at Arlington. I am grateful for his guidance during the course of my studies. I also would like to thank Dr. Dan Popa and Dr. Zeynep Celik-Butler for their interest in my research and spending time to be in my thesis committee.

I must thank my colleages Hamid Behjati, Vahidreza Nasirian, Seyedali Moayedi, Ali Bidram, and Fatih Cingoz for their technical and moral support for the last few years.

Lastly, I must thank my parents for their sacrifice and encouragement throughout my academic career.

April 13, 2012

ABSTRACT

TIME INVARIANT MODELING OF HIGHER ORDER DC-DC CONVERTERS

LEI NIU, M.S.

The University of Texas at Arlington, 2012

Supervising Professor: Ali Davoudi

A time invariant modeling technique is proposed for higher order dc-dc converters, including Cuk, SEPIC, and Zeta converters. This thesis also investigates some issues involved in applying existing averaging techniques such as circuit averaging, state space averaging, generalized state space averaging, Krylov-Bogoliubov-Mitropolsky method, and Floquet theory, to model the dynamic behaviors of higher order converters. The proposed methodology is shown to provide better accuracy compared to existing techniques, and distinguishes between different types of carrier signals of modulation, for instance, sawtooth and isosceles triangle carrier signal. This thesis offers a straightforward systematic procedure and summarizes this procedure with a list of rules, which makes the conversion from the state space model to the proposed time invariant model much easier. Hence, high order time invariant models can be easily developed for system design and stability analysis purposes. Both closed-loop time domain responses and open-loop frequency domain responses have been simulated and compared with the detailed switching model to verify the proposed methodology. Moreover, the simulation results of Cuk converter model are validated by experimental data for a 20W Cuk converter in both time and frequency domains.

TABLE OF CONTENTS

APPENDIX

LIST OF ILLUSTRATIONS

ix

x

xi

LIST OF TABLES

CHAPTER 1

INTRODUCTION

Pulse-width modulation (PWM) DC-DC converters has been widely implemented in various applications, such as telecommunication system, computer system, portable electronic devices, uninterrupted power supplies (UPS), and solar energy harvesting system for its high switching frequency, high power density, high conversion efficiency, and compactness [1]-[7]. As the expectation of performance for different applications increases, the conventional PWM DC-DC converters such as buck, boost, and buck-boost converters have begun to show their limitations in applications that involves galvanic isolation, wide range of input-to-output conversion ratio, and non-pulsating input and output current [8]-[10]. These limitations often cause the system designers to add additional components to the conventional converters, and result in high unit cost and hampers of the overall system performance. For example, in most maximum power point tracking (MPPT) techniques such as perturb and observe (P&O) and incremental conductance (IncCond), the process of determining the global maximum power point (MPP) of the solar module involves scanning the P-V curve (power-voltage curve) of the solar module [6] and [11]. This scanning often requires MPP tracker, which mainly consists of a PWM converter, to operate the photovoltaic (PV) system for a wide range of voltage levels. In such cases, buck-boost type behavior of MPP tracker is generally desired for performing the scan. Although buck-boost converter has a wide range of conversion ratio, it has an inverting output voltage, and compared to higher order converters, it is difficult to employ galvanic isolation which is a safety requirement for grid integrated solar systems [12]-[13]. Also, buck-boost converter has pulsating input and output current which makes it a poor choice for fuel cell and light-emitting diode (LED) related applications [14]-[15].

These aforementioned limitations of the conventional converters have motivated researchers and system designers to investigate the feasibility of employing higher order converters, namely Cuk converter [16]-[18], single-ended primary inductance converter (SEPIC) [19]-[21] and zeta converter [22]-[24], into their particular applications. In general, higher order converters have wide range of input-to-output conversion ratio, better adaptability of integrating transformers for galvanic isolation, and non-pulsating input and output current. For example, since Cuk converter has both input and output inductors, it has non-pulsating input and output current that makes it a great candidate for fuel cell and LED related applications [15],[18] and [25]. In a fuel cell power system, when the fuel cell operates at full load, even small current ripple in addition to the average fuel cell current can overload the fuel cell, which results lifespan and capacity reduction of the fuel cell [26]. In LED load applications, current distortion can lower the efficiency of the LED, and also introduces voltage distortion that causes flickering lights which may cause eye discomfort, headache and other well-known problems [27] and [28]. However, one drawback of the Cuk converter is that the output voltage polarity is inverted. Different from the Cuk converter, SEPIC has a non-inverting output voltage. Also, SEPIC has non-pulsating input current which makes SEPIC topology a great candidate for PV related applications. For example, the authors in [14] and [19] have suggested that SEPIC topology is highly suitable for multiple-input DC-DC converter (MIC) because of its non-pulsating input current, grounded switched and non-inverting output voltages. Another example of higher order converters is zeta converter. Compared with SEPIC, zeta converter also has a non-inverting output voltage. Since zeta converter topology offers easy adaptability for galvanic isolation, non-pulsating output current and non-inverting output voltage, zeta converter topology has become a great candidate for applications such as grid-integrated PV system, and low power switch-mode power supplies (SMPS) [8], [12] and [22]. A comparison table that summarizes the basic characteristics of both conventional converters and higher order converters have been listed in

Table 1.1. A similar table has been presented in [10], but only few converters have been selected.

Table 1.1 Comparison Table of Conventional Converters and Higher Order Converters

	Conventional Converters			Higher Order Converters		
Characteristcs	Buck	Boost	Buck-Boost	Cuk	SEPIC	Zeta
Conversion Ratio	Narrow	Narrow	Wide	Wide	Wide	Wide
Input Current	Pulsating	Non-pulsating	Pulsating	Non-pulsating	Non-pulsating	Pulsating
Output Current	Non-pulsating	Pulsating	Pulsating	Non-pulsating	Pulsating	Non-pulsating
Output Voltage Polarity	Non-inverting	Non-inverting	Inverting	Inverting	Non-inverting	Non-inverting
Type of Switch	Floated	Grounded	Floated	Grounded	Grounded	Floated
Energy Storage Components	2	2	2	4	4	4

Although higher order converters have many advantages, they still suffers from the complex dynamic behaviors as the conventional PWM DC-DC converters. Due to switches and diodes, PWM DC-DC converters are piece-wise linear time-varying systems that exhibits complex phenomenon such as bifurcation and chaos [29] and [30]. These complex dynamic behaviors have made designing stabilizing controllers for PWM DC-DC converters, especially for higher order converters, a very difficult task [31] and [32]. The key in designing stabilizing controllers is to develop a model that reveals the insight of the dynamic behaviors and the stability of these converters [24] and [33]. As a result, for the last forty years, many modeling techniques for PWM DC-DC converters have been proposed. Circuit averaging (CA) [34], [35] and state space averaging (SSA) techniques [36]-[38] were among the first modeling techniques developed for PWM DC-DC converters. In CA, the switches are represented by their

linear equivalent circuits with implementing the DC transformer model, hence traditional circuit analysis tools such as Kirchhoff voltage law (KVL) and Kirchhoff current law (KCL) can be employed. The end result of CA is often the input-output characteristic equation in terms of the control input, which is used for designing purposes. In SSA, a state space model is derived from the piece-wise linear circuit for each switching state. The SSA model is formed by estimating the system state variables with their averages in a given switching period. Although both CA and SSA techniques are two different ways of modeling PWM converters, the results produced by both CA model and SSA model have shown to be same [38]. However, both CA and SSA techniques can only approximate the system dynamics with acceptable accuracy when the switching frequency is relatively much faster than the dynamics of the system [36]. Also both CA and SSA does not account for switching ripples, which makes them inferior tools for designing stabilizing controller [31]. Due to the limitations in CA and SSA, several other techniques such as generalized state space averaging (GSSA) [39]-[41], Krylov-Bogoliubov-Mitropolsky (KBM) method of generalized averaging [42]-[46], and Floquet theory [36] have been proposed for switching frequency dependent approximation and ripples estimation for the system state variables. GSSA has been developed based on frequency-selective averaging. The accuracy of GSSA model can be improved by including more orders of harmonics from each state variable. However, as the order of the converter and the order of the harmonics increase, deriving the GSSA model becomes very difficult. As a result, GSSA is not a good candidate for modeling higher order converters with higher orders of harmonics approximation. KBM method has been widely used to solve for weakly nonlinear partial differential equations. KBM method also provides ripple estimation of state variables. However, in order for KBM method to provide sufficient accuracy of approximation, the ratio between the switching period and the system time constant system must be very small. Floquet theory has focused on improving SSA modeling by offering ripple estimation for the steady state condition, but it does not expose any information about the transient response.

4

Due to the problems in the existing modeling techniques, a new technique, namely time-invariant multi-frequency (TIMF) modeling, has been introduced by P.L. Chapman, A. Davoudi, and Y. Chen in [47], [48]. TIMF modeling has been developed on the basis of quasi-Fourier series (QFS) representation of state variables and switching function that allows it to account for the effects of ripples. Different from existing techniques, TIMF provides precise modeling of the switching function by taking into account the carrier signal. In the original works, both sawtooth and isosceles triangular carrier signal have been studied. Although the triangular carrier has been rarely used for PWM DC-DC converter, it has been implemented in PWM inverters for less baseband distortion [47]. Moreover, because triangular carrier allows double edge control, it is more suitable for PWM controllers operated at switching frequency greater than 1MHz [49]. In [47], TIMF models for conventional PWM DC-DC converters have been developed. However, no experimental results were given. In [48], TIMF has been used to model multiple-input buck-boost converters. However, only time-domain analysis has been provided. In the original works, the development of TIMF of a given converter depends on coefficient matching of both sizes of state equations. The process can become tedious and mathematically involved as the order of the system and the order of harmonics increase.

This thesis is an extended work of the previous works in TIMF [47], [48]. In this thesis, TIMF has been used to model higher order converters such as Cuk converter, SEPIC and zeta converters. Both time domain analysis and frequency domain analysis have been obtained and compared with the detailed switching model for all three higher order converters. Experimental results have been obtained for Cuk converter to verify closed-loop time-domain and open-loop frequency domain responses. Comparison has been made between the existing modeling techniques and TIMF. For accelerating the process of developing the TIMF model, the procedure of developing the TIMF model has been summarized into a set of rules. By following these rules, high order TIMF model can be easily developed.

5

The structure of this thesis is as follows. Chapter 2 covers a literature review of existing modeling techniques. These techniques are introduced in the following order: CA, SSA, GSSA, KBM method, and Floquet Theory. Chapter 3 begins with the introduction of the TIMF modeling techniques. The rest of Chapter 3 presents the case studies of Cuk converter, SEPIC and zeta Converter. In the Cuk converter subsection, experimental results of both time domain and frequency domain have been given. The Cuk converter subsection also includes the comparison between the existing techniques and TIMF. Chapter 4 concludes the thesis and offers visions for future works on TIMF modeling technique.

CHAPTER 2

OVERVIEW OF EXISTING TIME INVARIANT TECHNIQUES

2.1 Circuit Averaging

The key concept in circuit averaging (CA) is to model the nonlinear behaviors of switching with linear circuit elements with the optimistic assumption that the linear equivalent circuit models will reveal the main characteristics of the dynamical behaviors [34]-[42]. Compared with state space averaging, CA offers a better physical insight of the converter, and the DC and small-signal characteristics of the converter can be easily developed by using traditional circuit analysis techniques such Kirchhoff voltage (KVL), Kirchhoff current law (KCL), inductor volt-second balance and capacitor charge balance. The expressions of inductor volt-second balance and capacitor charge balance are given in Equation 2.1 and 2.2, respectively

$$< v_L(t) > = \int_0^{T_s} v_L(t) = 0 \qquad\qquad (2.1)$$

$$< i_c(t) > = \int_0^{T_s} i_c(t) = 0 \, , \qquad\qquad (2.2)$$

where $< v_L >$ and $< i_C >$ are the averages of inductor voltage, $v_L(t)$, and capacitor current, $i_c(t)$, in a given switching period, T_s , respectively.

As discussed, the most important part of CA is to model the PWM switch with linear circuit elements such as dependent voltage source and current source [40]. Most PWM switches in DC-DC PWM converters can be considered as a three-terminal nonlinear device as presented in Figure 2.1. In Figure 2.1, terminals a , p and c are referred to as active, passive and common, respectively. In continuous conduction mode, there are two switching states for the switching device. In the first switching state, the switch is at Position 1 and stays at Position 1 during the time interval $0 < t < dT_s$, where d is the duty cycle. In the second switching state,

7

at $t = dT_s$ the switch changes its position to Position 2, and stay at Position 2 for the rest of the switching period. The relations of the instantaneous terminal voltages and currents during these two switching states are given by Equation 2.3 and 2.4.
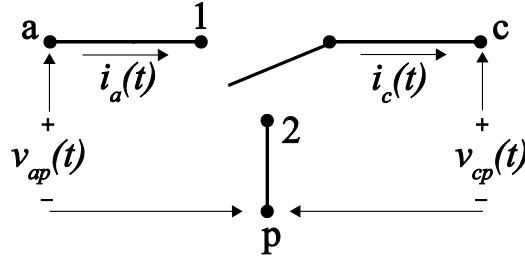
Figure 2.1 A three-terminal nonlinear device

$$i_a(t) = \begin{cases} i_c(t) & 0 \le t \le dT_s \\ 0 & dT_s < t \le T_s \end{cases} \tag{2.3}$$

$$v_{cp}(t) = \begin{cases} v_{ap}(t) & 0 \le t \le dT_s \\ 0 & dT_s < t \le T_s \end{cases} . \tag{2.4}$$

Since the CA mainly focus on the DC and small-signal characteristics of the converter, the relations of the average terminal voltages and currents are given by

$$< i_a > = d < i_c > \tag{2.5}$$

$$< v_{cp} > = d < v_{ap} > . \tag{2.6}$$

With the relations presented in Equation 2.5 and 2.6, the three-terminal nonlinear device, as shown in Figure 2.1, can be represented with linear circuit models by exploiting the concept of dependent voltage and current sources, as shown in Figure 2.2.
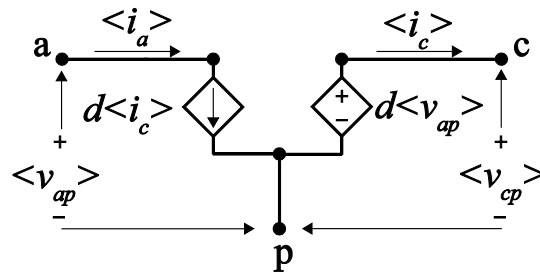
Figure 2.2 Dependent source representation of PWM switch

Replacing the PWM switch with the equivalent average circuit model, as shown in Figure 2.2, changes the nature of the PWM converter from a piece-wise linear time varying system to a linear time-invariant (LTI) system. The resulting system is much easier to analyze compared with the original system. However, the assumptions of small ripples and high switching frequency have led to substantial discrepancy at low switching frequencies between the CA model and the actual system [82].

Despite the shortcomings of CA model, CA model can easily include non-ideal behaviors of circuit components such as equivalent series resistances (ESR) of the inductors and capacitors, forward voltage drop and on-resistance of the switches and diodes by incorporating the DC transformer model of the PWM switch, as shown in Figure 2.3. Although real DC transformer does not exist, the benefit of implementing DC transformer model is that rules for solving circuits with transformers still apply here [34]. In [37], a systematic approach of including the parasitic elements has been presented.
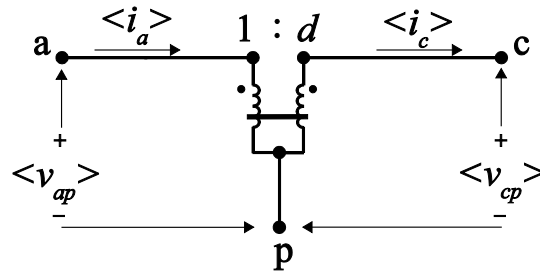
Figure 2.3 DC transformer model of PWM switch

In fact, Figure 2.1 shows only an example of PWM switch. Not all PWM switches are arranged as shown in Figure 2.1. As a result, the number of topologies is restricted for the CA techniques. In [36], a generalized PWM-switch model has been proposed.

2.2 State Space Averaging

As previously discussed in CA, DC transformer model has made analyzing non-ideal PWM converter easier. However, in CA, the average model of PWM switch is heavily dependent on the converter topology. In the case of a non-ideal PWM switch, in order to include

9

the on-resistance and forward bias voltage of the semiconductor devices, an extra step has been taken to derive the average model for these parasitic effects in the switching components. These limitations of CA have led a shift of interest to the state space averaging (SSA) technique [50]-[53]. In SSA, the linear equivalent circuit model corresponded to each switching state of PWM converter has been represented by a system of differential equations using the relations between time varying voltage and current in a given inductor and capacitor [43]-[45], [80]. Depending on the number of switching states, there are the same number of sets of system of differential equations. The state space model of the PWM converter is formed by taking time average of these sets of system of differential equations within a given switching period. Due to the convenience in computing for the input-to-output and control-to-output transfer functions in the state space model, SSA has also been widely used for analyzing systems with piece-wise linear networks and designing the controller for a dynamic system. Although CA and SSA models have been developed based on different theories, the results obtained from SSA and CA have been shown to be the identical [45]. The rest of this subsection will be devoted to deriving the SSA model of PWM converters in CCM.

As already described in CA, in CCM, the switch is on during $0 < t < dT_s$ and is off during $dT_s < t < T_s$, where d is the duty cycle and T_s is the switching period. Therefore, the state space model of PWM DC-DC converter in CCM can be represented as

$$\dot{\mathbf{x}}_1 = d(\mathbf{A}_1\mathbf{x}_1 + \mathbf{b}_1\mathbf{u}) \qquad 0 < t < dT_s \qquad\qquad (2.7)$$

$$\dot{\mathbf{x}}_2 = (1-d)(\mathbf{A}_2\mathbf{x}_2 + \mathbf{b}_2\mathbf{u}) \qquad dT_s < t < T_s \qquad\qquad (2.8)$$

in which $\mathbf{x}_1$ and $\mathbf{x}_2$ are vectors of state variables such as inductor currents and capacitor voltages in different switching states , $\dot{\mathbf{x}}_1$ and $\dot{\mathbf{x}}_2$ are the time derivatives of vector $\mathbf{x}_1$ and $\mathbf{x}_2$, respectively, $\mathbf{A}$ is the system matrix, $\mathbf{b}$ is the input matrix, and the subscript 1 and 2 corresponds the on and off state of switch, respectively. In Equation 2.7 and 2.8, $\mathbf{x_1}$ and $\mathbf{x_2}$ are

not the same vectors of state variables because they are from different linear circuit models. $\mathbf{x_1}$ relates to $\mathbf{x_2}$ at time $t = dT_s$ as stated in Equation 2.9.

$$\mathbf{x}_1(dT_s) = \mathbf{x}_2(dT_s) \tag{2.9}$$

As presented in Equations 2.7-2.9, in order to solve $\mathbf{x_2}$, one has to first solve for $\mathbf{x_1}$. And to solve for $\mathbf{x_1}$ for the next switching period, one needs the value of $\mathbf{x_2}$ at the previous switching period. The purpose of SSA is to simplify this procedure by finding the condition in which $\mathbf{x_1}$ and $\mathbf{x_2}$ can be represented by only one unknown vector $\mathbf{x_{av}}$, an average vector that closely related to both vectors. As a result, one can simply combine Equations 2.7 and 2.8 into one equation and solve for $\mathbf{x_{av}}$,

$$\dot{\mathbf{x}}_{av} = d(\mathbf{A}_1\mathbf{x}_{av} + \mathbf{b}_1\mathbf{u}) + (1 - d)(\mathbf{A}_2\mathbf{x}_{av} + \mathbf{b}_2\mathbf{u}). \tag{2.10}$$

To find such condition, one should first examine the cycle transition matrix as given in Equation 2.11. To make logical deduction easier, only the homogenous solution of Equation 2.8 for $0 < t < T_s$ has been considered (neglect the terms $\mathbf{b}_1\mathbf{u}$ and $\mathbf{b}_2\mathbf{u}$), which is given by

$$\mathbf{x_2} = e^{\mathbf{A}_2(1-d)T_s} e^{\mathbf{A}_1 dT_s} \mathbf{x}_1(0), \tag{2.11}$$

where $\mathbf{x}_1(0)$ is the initial conditions of state variable vector $\mathbf{x_1}$ in the first switching cycle. Similarly, the homogeneous solution of Equation 2.9 is given by

$$\mathbf{x}_{av} = e^{\mathbf{A}_2(1-d)T_s + \mathbf{A}_1 dT_s} \mathbf{x_{av}}(0), \tag{2.12}$$

where $\mathbf{x}_{av}(0)$ is the initial condition of $\mathbf{x}_{av}$ in the first switching cycle. Compared with Equation 2.12, Equation 2.11 involves the multiplication of two exponential matrices. Consequently, in order for Equation 2.10 to be valid, the following condition must be satisfied [75]

$$e^{\mathbf{A}_2(1-d)T_s} e^{\mathbf{A}_1 dT_s} \approx e^{\mathbf{A}_2(1-d)T_s + \mathbf{A}_1 dT_s}. \tag{2.13}$$

Approximating the exponential matrices by their first harmonics, the left hand side of Equation 2.13 becomes

$$e^{\mathbf{A}_2(1-d)T_s}e^{\mathbf{A}_1 dT_s} \approx \left[\mathbf{I} + \mathbf{A}_2(1-d)T_s\right]\left[I + \mathbf{A}_1 dT_s\right]$$

$$\approx \mathbf{I} + \mathbf{A}_2(1-d)T_s + \mathbf{A}_1 dT_s + \mathbf{A}_2\mathbf{A}_1(1-d)dT_s^2 \qquad (2.14)$$

and the right hand side of Equation 2.13 becomes

$$e^{\mathbf{A}_2(1-d)T_s + \mathbf{A}_1 dT_s} \approx \mathbf{I} + \mathbf{A}_2(1-d)T_s + \mathbf{A}_1 dT_s. \qquad (2.15)$$

After comparing Equation 2.14 with 2.15, one can easily conclude that Equation 2.14 will approximately equal to Equation 2.15 only if T_s is relatively small compared to time constants in $\mathbf{A}_1$ and $\mathbf{A}_2$. If this condition is true, then Equations 2.7 and 2.8 can be combined into Equation 2.10 without losing too much information about the system dynamics. Consequently, the output y is can be approximated as

$$y_{av} = \left(d\mathbf{c}_1^T + (1-d)\mathbf{c}_2^T\right)\mathbf{x}_{av}, \qquad (2.16)$$

where $\mathbf{c}^T$ is the output matrix. Equations 2.10 and 2.16 together forms the bases of the SSA modeling of PWM converters .

Different from the solving algebraic equations in CA, SSA often involves matrix calculation, which is more mathematically involved. However, SSA model offers a better insight of the dynamical behavior of the PWM converter. Since both CA and SSA models of PWM converters are frequency independent models that assume high switching frequency, if the switching frequency of PWM converter is relatively low, both models will become inaccurate [58]. Also, both modeling techniques cannot be used for large signal analysis due to their inability to account of ripples in the capacitor voltage and inductor currents. These shortcomings have made CA and SSA inferior tools for analyzing stability of a system, especially for higher order converters, which are systems that exhibit more complex dynamical behaviors. In response to these shortcomings of CA and SSA, modeling techniques that offer ripple estimation and large-signal characteristics have become the one of the major research areas in power electronics.

2.3 Generalized State Space Averaging

As in SSA technique, generalized state space averaging (GSSA) also assumes that the switching frequency of PWM converter is higher than the system dynamics. GSSA technique, as presented in [46]-[48], has been developed on basis of frequency-selective averaging. In frequency-selective averaging, due to periodic nature of the switching operation, circuit state variables such as inductor currents or capacitor voltage have been estimated by quasi-Fourier series (QFS). Different from original Fourier series, quasi-Fourier series contains time-dependent Fourier coefficients, namely the QFS coefficients. Consequently, GSSA modeling provides frequency dependent approximation and ripples estimation for the state variables. The accuracy of GSSA can be improved by increasing the order of harmonics in the model. Since GSSA produces large signal model for PWM circuits, it has been widely implemented in the fields such as modeling of resonant converters [80], [81], multiconverter [83], and power electronic loads [84]. The purpose of this section is to briefly review the concept of frequency-selective averaging and GSSA modeling.

In frequency-selective averaging, a signal $x(t)$ is represented in the exponential form of the Fourier series

$$x(t) = \sum_{n=-\infty}^{\infty} x_n(t) e^{jn\omega_s t} , \tag{2.17}$$

where ω_s is the radian frequency, n is the index number, and $x_n(t)$ is the complex QFS coefficient. Procedure in computing these complex Fourier coefficients is the same as computing the constant Fourier coefficients, which is given by

$$x_n(t) = \frac{1}{T} \int_{t-T}^{t} x(t) e^{-jn\omega_s \tau} d\tau , \tag{2.18}$$

where T is the period. Converting $x(t)$ from the complex form to trigonometric form of Fourier series in terms of $x_n(t)$ as defined in Equation 2.17 simply yields

13

$$x(t) = x_0 + 2\sum_{n=1}^{\infty} \Re\{x_n(t)\}\cos(n\omega_s t) - \Im\{x_n(t)\}\sin(n\omega_s t), \tag{2.19}$$

where $\Re\{x_n(t)\}$ and $\Im\{x_n(t)\}$ are the real part and imaginary part of $x_n(t)$. The process of the conversion are presented in [76]. In Equation 2.19, the DC component of the signal is given by

$$x_0 = \frac{1}{T}\int_{t-T}^{t} x(\tau)d\tau . \tag{2.20}$$

This DC component x_0 is the same as the average value of a state variable predicted in SSA. In order words, when the effects of harmonics are low, GSSA model can be reduced to SSA model. In order to apply the GSSA to any PWM DC-DC converter, two properties must be investigated: 1) the derivative of $x_n(t)$ with respect to time and 2) the product of the switching signal $q(t)$ and state variable $x(t)$.

The first property that must be investigated is the derivative of $x_n(t)$ with respect to time. According to Leibniz integral rule, differentiating Equation 2.18 yields

$$\frac{dx_n(t)}{dt} = \frac{1}{T}\int_{t-T}^{t}\left(\dot{x}(\tau)e^{-jn\omega_s\tau} - jn\omega_s x(\tau)e^{-jn\omega_s\tau}\right)d\tau , \tag{2.21}$$

$$+ \frac{1}{T}\left(x(t)e^{-jn\omega_s t} - x(t-T)e^{-jn\omega_s(t-T)}\right).$$

Since the signal is assumed to be periodic, the second part of Equation 2.21 can be neglected, and leaving

$$\frac{dx_n(t)}{dt} = \left\langle\frac{dx}{dt}\right\rangle_n - jn\omega_s x_n \tag{2.22}$$

as presented in [46]. Therefore, from Equation 2.22, the voltage-current relations for passive circuit elements, resistors, inductors, and capacitors are given by

$$v_n = Ri_n \tag{2.23}$$

$$L\frac{di_n}{dt} = v_n - jn\omega_s i_n \tag{2.24}$$

14

$$C\frac{dv_n}{dt} = i_n - jn\omega_s v_n \,,\tag{2.25}$$

respectively.

The second property that is required for constructing GSSA model is the product of the switching signal $q(t)$ and state variable $x(t)$. Consider a special case of the switching signal $q(t)$ and state variable $x(t)$ in complex exponential form are approximated by the first harmonic $n = 1$,

$$q(t) \approx q_0 + q_{-1}e^{-j\omega_s t} + q_1 e^{j\omega_s t}\tag{2.26}$$

$$x(t) \approx x_0 + x_{-1}e^{-j\omega_s t} + x_1 e^{j\omega_s t}\tag{2.27}$$

One can simply carry out the multiplication using expressions of $q(t)$ and $x(t)$ as presented in Equation 2.26 and 2.27, or using the discrete convolution method described in [46], the following products are obtained

$$\langle qx \rangle_0 = q_0 x_0 + q_{-1}x_1 + q_1 x_{-1}\tag{2.28}$$

$$\langle qx \rangle_1 = q_0 x_1 + q_1 x_0\tag{2.29}$$

$$\langle qx \rangle_{-1} = q_0 x_{-1} + q_{-1}x_0 \,,\tag{2.30}$$

where $\langle qx \rangle_0$ refers to the sum of products with common term e^0, $\langle qx \rangle_1$ the sum of products with common term $e^{j\omega_s t}$, and $\langle qx \rangle_{-1}$ the sum of products with common term $e^{-j\omega_s t}$. Given that q_1 and q_{-1}, x_1 and x_{-1} are complex conjugate pairs, Equations 2.28-2.30 can be written as

$$\langle qx \rangle_0 = q_0 x_0 + 2\left(q_1^R x_1^R + q_1^I x_1^I\right)\tag{2.31}$$

$$\langle qx \rangle_1^R = q_0 x_1^R + x_0 q_1^R\tag{2.32}$$

$$\langle qx \rangle_1^I = q_0 x_1^I + x_0 q_1^I \,,\tag{2.33}$$

where superscript R and I indicate the real and imaginary part of the complex number, respectively.

Using these two described properties, the state space model can be converted to GSSA model. However, as the order of harmonics considered increases, the process in deriving the products becomes very complicated. As a result, GSSA is not a good candidate for modeling higher order converters with higher orders of harmonics approximation. For comparison purpose, GSSA model of Cuk converter has been derived, and details are presented in Chapter 3.

2.4 Krylov-Bogoliubov-Mitropolsky Method of Generalized Averaging

Krylov-Bogoliubov-Mitropolsky (KBM) method of generalized averaging has been introduced in [49] and [50]. KBM method has been widely used to solve for weakly nonlinear partial differential equations, as discussed in [54]-[57]. Since KBM method computes ripple approximations for state variables, it has been used to model various converters, such as PWM converters, and PFC converters [58]-[65]. However KBM method also has its limitation. In order for KBM method to provide sufficient accuracy of approximation, a parameter ε which is related to the product of the switching period and the system time constant must be very small [47]. This concept can be illustrated by the following example, consider a simple first order differential equation [66]

$$\frac{dx}{dt} = -\varepsilon x.$$
(2.34)

The solution to Equation 2.34 is simply

$$x = Ce^{-\varepsilon t},$$
(2.35)

where C is a constant. Expanding the exponential term in Equation 2.35 yields

$$x = C\left(1 - \varepsilon t + \frac{\varepsilon^2 t^2}{2} - \cdots\right).$$
(2.36)

16

Obviously, if $\varepsilon \ll \dfrac{1}{t}$, then x can be approximated by using only one, two or three terms. This idea is the principal concept behind averaging method. The same concept has also been applied when using KBM to obtain analytical results from state space model of PWM converters. As discussed in [55] and [57], due to the periodic nature of PWM converters, their state space models can be described as

$$\dot{x} = \varepsilon F(t, x) \tag{2.37}$$

where $\varepsilon \ll 1$, and $F(t, x)$ is a function of t and x. The general solution of Equation 2.37 is given by

$$x = x_0 + \varepsilon x_1 + \varepsilon^2 x_2 + \cdots + \varepsilon^n x_n, \tag{2.38}$$

where x_n are the fundamental set of solutions for Equation 2.37. Equation 2.38 is also known as the asymptotic approximation of state variable x. By applying averaging to the right hand side of Equation 2.38 by defining

$$G(y) = \lim_{T \to \infty} \frac{1}{T} \int_0^T F(\tau, x) d\tau, \tag{2.39}$$

where $G(y)$ is the time average of $F(t, x)$. As a result, state space average model of Equation 2.37 is given by

$$\dot{y} = \varepsilon G(y). \tag{2.40}$$

Equation 2.40 is the time-invariant (TI) averaged system of Equation 2.37 [49]. Integrating Equation 2.37 and applying change of variables simply yields

$$x(t) = y(t) + \varepsilon \Psi_1(t, y) + \varepsilon^2 \Psi_2(t, y) + \cdots, \tag{2.41}$$

where Ψ_i are the zero-average functions of time that estimates ripples. Since $y(t)$ can be easily obtained from SSA model, the unknowns in Equation 2.41 are Ψ_i. With the help of Equation 2.40, the time invariant system of Equation 2.37 can also be written as

17

$$\dot{y} = \varepsilon G_1(y) + \varepsilon^2 G_2(y) + \cdots, \tag{2.42}$$

where G_n is the fundatmental set of solutions of Equation 2.40.

In order to find the unknown Ψ_i, first differentiating Equation 2.41, and substituting $\dot{y}$ with Equation 2.42 and $\dot{x}$ with Equation 2.37, then by equating the coefficients of ε, ε^2 and higher orders of ε, expressions for Ψ_i in terms of $G_i(y)$ can be found. The whole process is illustrated through an example of deriving KBM model for the open-loop Cuk converter, and details are presented in case study section of Cuk converter.

2.5 Floquet Theory of PWM Converter Modeling

Converter modeling using Floquet theory has been presented in [36], [67]-[70]. This method has aimed at improving SSA modeling by offering ripple estimation for the steady state response. A major limitation of this method is that it does not expose any information about the transient response. Consequently, it is not certain how this method can be applied for closed-loop control. Despite these limitations of Floquet theory, it has been used to analyze the stability of various converters [60], [62].

In CCM, a PWM DC-DC converter has two switching states, and the state space model can be represented by the following equation,

$$\dot{\mathbf{x}}(t) = \sum_{i=1}^{2} \mathbf{A}_i \mathbf{x}(t) + \mathbf{b}_i \tag{2.43}$$

where $x(t)$ is the state variable vector, $\mathbf{A_i}$ is the effective system matrix which includes the effects of the switching function, $\mathbf{b}_i$ is the excitation term that incorporates the inputs to the system, and i refers to the switching state. The time that the converter stays in every switching state is

$$\Delta t_i = d_i T, \tag{2.44}$$

where d_i is the duty cycle of ith switching state, and T is the switching period. From Equation 2.43, during the time interval $t_{i-1} < t < t_i$, solving $x(t)$ yields [36],

$$\mathbf{x}(t_i) = \mathbf{\Phi}_i \mathbf{x}(t_{i-1}) + \mathbf{\Gamma}_i \tag{2.45}$$

where

$$\mathbf{\Phi}_i = e^{\mathbf{A}_i d_i T}, \tag{2.46}$$

$$\mathbf{\Gamma}_i = \int_{t_{i-1}}^{t_i} e^{\mathbf{A}_i(t_i - \tau)} \mathbf{b}_i d\tau . \tag{2.47}$$

Assuming $\mathbf{A}_i$ is invertible, Equation 2.47 becomes

$$\mathbf{\Gamma}_i = \left(e^{\mathbf{A}_i d_i T} - \mathbf{I} \right) \mathbf{A}_i^{-1} \mathbf{b}_i . \tag{2.48}$$

By evaluating from Equation 2.45 through multiple iterations, $\mathbf{x}(t_i)$ can be related to $\mathbf{x}(t_0)$ as shown in the Equation 2.49

$$\mathbf{x}(t_i) = \mathbf{\Phi}_i \mathbf{\Phi}_{i-1} \cdots \mathbf{\Phi}_1 \mathbf{x}(t_0) + \mathbf{\Phi}_i \mathbf{\Phi}_{i-1} \cdots \mathbf{\Phi}_2 \mathbf{\Gamma}_1 + \cdots \mathbf{\Phi}_i \mathbf{\Gamma}_{i-1} + \mathbf{\Gamma}_i . \tag{2.49}$$

If the system exhibits a periodic behavior, then the solution for system described in Equation 2.44 also has the following property

$$\mathbf{x}(t_i) = \mathbf{x}(t_i - T) = \mathbf{x}(t_i - 2T) = \cdots = \mathbf{x}(t_0). \tag{2.50}$$

Because of the above assumption, Floquet theory can only be used for analyzing steady state response, and is not suitable for transient analysis. Thus, by combining Equations 2.49 and 2.50, the initial conditions of state variables can be found as

$$\mathbf{x}(t_0) = \left(\mathbf{I} - \mathbf{\Phi}_i \mathbf{\Phi}_{i-1} \cdots \mathbf{\Phi}_1 \right)^{-1} \left(\mathbf{\Phi}_i \mathbf{\Phi}_{i-1} \cdots \mathbf{\Phi}_2 \mathbf{\Gamma}_1 + \cdots + \mathbf{\Phi}_i \mathbf{\Gamma}_{i-1} + \mathbf{\Gamma}_i \right). \tag{2.51}$$

In order to simply the derivation, for each switching state i , the system can be represented as

$$\frac{d}{dt} \begin{bmatrix} \mathbf{x}(t) \\ 1 \end{bmatrix} = \begin{bmatrix} \mathbf{A}_i & \mathbf{b}_i \\ \mathbf{0} & \mathbf{0} \end{bmatrix} \begin{bmatrix} \mathbf{x}(t) \\ 1 \end{bmatrix} \tag{2.52}$$

or

19

$$\frac{d}{dt}\hat{\mathbf{x}}(t) = \hat{\mathbf{A}}_i \hat{\mathbf{x}}(t).$$ (2.53)

By solving Equation 2.53, two important equations can be obtained. The first equation relates the state variable at t_{i-1} to t_i by the following equation

$$\hat{\mathbf{x}}(t_i) = \hat{\boldsymbol{\Phi}}\hat{\mathbf{x}}(t_{i-1}),$$ (2.54)

where

$$\hat{\boldsymbol{\Phi}}_i = e^{\hat{\mathbf{A}}_i d_i T}.$$ (2.55)

The second equation relates $\hat{\mathbf{x}}(t_i)$ to $\hat{\mathbf{x}}(t_0)$

$$\hat{\mathbf{x}}(t_i) = \hat{\boldsymbol{\Phi}}_i \hat{\boldsymbol{\Phi}}_{i-1} \cdots \hat{\boldsymbol{\Phi}}_1 \hat{\mathbf{x}}(t_0) = \hat{\boldsymbol{\Phi}}_{tot} \hat{\mathbf{x}}(t_0).$$ (2.56)

By defining new variables $\boldsymbol{\Phi}_{tot}$ and $\boldsymbol{\Gamma}_{tot}$, Equation 2.51 simplifies into

$$\mathbf{x}(t_0) = (\mathbf{I} - \boldsymbol{\Phi}_{tot})^{-1} \boldsymbol{\Gamma}_{tot},$$ (2.57)

where

$$\boldsymbol{\Phi}_{tot} = \boldsymbol{\Phi}_i \boldsymbol{\Phi}_{i-1} \cdots \boldsymbol{\Phi}_1$$ (2.58)

$$\boldsymbol{\Gamma}_{tot=} \boldsymbol{\Phi}_i \boldsymbol{\Phi}_{i-1} \cdots \boldsymbol{\Phi}_2 \boldsymbol{\Gamma}_1 + \cdots + \boldsymbol{\Phi}_i \boldsymbol{\Gamma}_{i-1} + \boldsymbol{\Gamma}_i.$$ (2.59)

The new variables $\boldsymbol{\Phi}_{tot}$ and $\boldsymbol{\Gamma}_{tot}$ relate to $\hat{\boldsymbol{\Phi}}_{tot}$ as given in Equation 2.60

$$\hat{\boldsymbol{\Phi}}_{tot} = \begin{bmatrix} \mathbf{I} - \boldsymbol{\Phi}_{tot} & -\boldsymbol{\Gamma}_{tot} \\ \mathbf{0} & \mathbf{0} \end{bmatrix}.$$ (2.60)

Since the average steady state values of the state space vector $\mathbf{x}_{av}$ relates to $\mathbf{x}(t)$ as

$$\dot{\mathbf{x}}_{av} = \frac{1}{T}\mathbf{x}(t),$$ (2.61)

$\mathbf{x}_{av}$ can be found by introducing them to the state variable vector as presented in the following system

$$\frac{d}{dt}\begin{bmatrix} \mathbf{x}(t) \\ 1 \\ \mathbf{x}_{av} \end{bmatrix} = \begin{bmatrix} \mathbf{A}_i & \mathbf{b}_i & \mathbf{0} \\ \mathbf{0} & \mathbf{0} & \mathbf{0} \\ \dfrac{\mathbf{I}}{T} & \mathbf{0} & \mathbf{0} \end{bmatrix}\begin{bmatrix} \mathbf{x}(t) \\ 1 \\ \mathbf{x}_{av} \end{bmatrix}. \tag{2.62}$$

The ripples of each state variable can be estimated by finding the Fourier series coefficients c_k

$$c_k = \frac{1}{T}\int_{t_0}^{t_0+T} x(t)e^{-jk\omega t}\,dt, \tag{2.63}$$

where the index k refers to the number of harmonics. From Equations 2.44, 2.45 and 2.63, between t_i and t_{i-1}, $\mathbf{c}_k$ is defined as,

$$\mathbf{c}_k = \sum_{i=1}^{n}\int_{t_{i-1}}^{t_i} \frac{1}{T}e^{-jk\omega t_{i-1}}e^{\hat{\mathbf{A}}_i(t-t_{i-1})}e^{-jk\omega(t-t_{i-1})}\hat{\mathbf{x}}(t_{i-1})\,dt. \tag{2.64}$$

Rearranging Equation 2.64 yields

$$\mathbf{c}_k = \sum_{i=1}^{m}\mathbf{w}_k(t_i), \tag{2.65}$$

where

$$\mathbf{w}_k(t_i) = \int_{t_{i-1}}^{t_i} \frac{1}{T}e^{-jk\omega t_{i-1}}\mathbf{v}_k(t_i)\,dt \tag{2.66}$$

$$\mathbf{v}_k(t_i) = e^{(\hat{\mathbf{A}}_i - jk\omega\mathbf{I})(t_i-t_{i-1})}\hat{\mathbf{x}}(t_{i-1}). \tag{2.67}$$

From Equations 2.66 and 2.67, it can be clearly seen that

$$\mathbf{v}_k(t_{i-1}) = \hat{\mathbf{x}}(t_{i-1}) \tag{2.68}$$

$$\mathbf{w}_k(t_{i-1}) = 0. \tag{2.69}$$

From Equations 2.66 and 2.67, one can also conclude the following equation [36]

$$\frac{d}{dt}\begin{bmatrix} \mathbf{v}_k(t_i) \\ \mathbf{w}_k(t_i) \end{bmatrix} = \begin{bmatrix} \hat{\mathbf{A}}_i - jk\omega\mathbf{I} & \mathbf{0} \\ \dfrac{1}{T}e^{-jk\omega t_{i-1}}\mathbf{I} & \mathbf{0} \end{bmatrix}\begin{bmatrix} \mathbf{v}_k(t_i) \\ \mathbf{w}_k(t_i) \end{bmatrix}. \tag{2.70}$$

After integrating both sides in Equation 2.70, and substituting $v_k(t_{i-1})$ with Equation 2.68, the vector $\mathbf{w}_k(t_i)$ is found as

$$\mathbf{w}_k\big(t_i\big) = e^{\mathbf{\Lambda}_{i,k} d_i T}\,\hat{\mathbf{x}}\big(t_{i-1}\big),$$ (2.71)

where

$$\mathbf{\Lambda}_{i,k} = \begin{bmatrix} \hat{\mathbf{A}}_i - jk\omega\mathbf{I} & \mathbf{0} \\ \dfrac{1}{T}e^{-jk\omega t_{i-1}}\mathbf{I} & \mathbf{0} \end{bmatrix}.$$ (2.72)

With knowing average values of the state space vector $\mathbf{x}_{av}$, and the Fourier coefficients $\mathbf{c}_k$, one can easily estimate the steady state response of the system. Floquet theory has the capability of modeling PWM DC-DC converters in the discontinuous conduction mode (DCM), however as the number of switching states increases, Equation 2.50 will become extremely complicated. Thus, finding the state space vector $\mathbf{x}_{av}$, and the Fourier coefficients $\mathbf{c}_k$ becomes a very difficult task.

CHAPTER 3

TIME INVARIANT MULTI-FREQUENCY MODELING OF HIGHER ORDER CONVERTERS

In this chapter, the development of time invariant multi-frequency (TIMF) models has been reviewed. Case studies have been made for Cuk converter, Zeta converter and SEPIC. For each case study, converter model with parasitic elements has been constructed. By including the parasitic elements in the models, the dynamic performance of the converter can be predicted with better accuracy. Also in case studies, closed-loop time domain response and open-loop frequency domain response have been studied and compared with the detailed switching model. The difference between implementing sawtooth carrier signal and triangular signal has been examined. In the case study session for Cuk converter, the experimental results obtained from 20W Cuk converter has been used to validate the TIMF model in both time domain and frequency domain. In order to show the improvement of accuracy with the TIMF model, first order TIMF model of Cuk converter has been compared with existing averaging techniques. In order to show the improvements in accuracy by increasing the order of the TIMF, in the case study session for Zeta converter, sixth order TIMF model has been implemented and compared with second order TIMF model. As expected, ripple estimation has been greatly improved.

3.1 General Theory

Time-invariant multi-frequency (TIMF) modeling method, previously introduced by P.L. Chapman, A. Davoudi, and Y. Chen in [71], [72], has been developed based on the quasi-Fourier series (QFS) representation of the switching function, duty cycle command, inductor currents and capacitor voltages of a PWM DC-DC converter operated in the continuous conduction mode (CCM) under a constant switching frequency. As a result, TIMF has the ability

23

to achieve highly accurate estimation of the ripple effects by including higher order harmonics. Suppose a state variable $x(t)$, the quasi-Fourier series representation of $x(t)$ is given by

$$x(t) = x_0(t) + \sum_{n=1}^{N} x_{\alpha_n}(t)\cos(n\omega_{sw}t) + x_{\beta_n}(t)\sin(n\omega_{sw}t) \tag{3.1}$$

where ω_{sw} is the switching frequency in radians, $x_0(t)$, $x_{\alpha_n}(t)$, and $x_{\beta_n}(t)$ are time-dependent QFS coefficients, n is an index term, and N is the number of harmonics considered by QFS. The QFS has been first introduced in [40]. However, the complex exponential form has been replaced by trigonometric form for the simplicity in developing TIMF model. As presented in Equation 3.1, for every state variable $x(t)$, there are $2N+1$ QFS coefficients. The higher the number N, the better the approximation is. However, as N increases, the computation time also increases. From this point on, the time dependency of state variable will be expressed implicitly. In order to develop TIMF model for any PWM DC-DC converters, the following three important properties are indispensible: 1) first order time derivative of state variable x, 2) carrier signal dependent model of the switching function q, and 3) computation of the product of state variable x and switching function q.

3.1.1 First Order Time Derivative of State Variable x

Since in TIMF model, each state variable x is represented by QFS, it becomes inevitable that there should be a corresponding representation for the time derivative of state variable x. Differentiating both sides of Equation 3.1, the time derivative of variable x has the form

$$\frac{dx}{dt} = \frac{dx_0}{dt} + \sum_{n=1}^{N} -n\omega_{sw}x_{\alpha_n}\sin(n\omega_{sw}t) + n\omega_{sw}x_{\beta_n}\cos(n\omega_{sw}t) +$$

$$\frac{dx_{a_n}}{dt}\cos(n\omega_{sw}t) + \frac{dx_{\beta_n}}{dt}\sin(n\omega_{sw}t). \tag{3.2}$$

Equation 3.2 can be expressed in a more compact form

$$\frac{dx}{dt} = \mathbf{c}\left(-\mathbf{\Omega x} + \frac{d\mathbf{x}}{dt}\right) \tag{3.3}$$

where $\mathbf{x}$ is a vector of QFS coefficients, $\mathbf{c}$ is a vector of time-varying coefficients, and $\mathbf{\Omega}$ is a $(2N+1)$-by-$(2N+1)$ matrix. These newly introduced vectors and matrix have been expressed explicitly in Equation 3.4-3.6,

$$\mathbf{x}^T = \begin{bmatrix} x_0 & x_{\alpha_1} & x_{\beta_1} & \cdots & x_{\alpha_N} & x_{\beta_N} \end{bmatrix} \tag{3.4}$$

$$\mathbf{c} = \begin{bmatrix} 1 & \cos(\omega_{sw}t) & \sin(\omega_{sw}t) & \cdots & \cos(n\omega_{sw}t) & \sin(n\omega_{sw}t) \end{bmatrix} \tag{3.5}$$

$$\mathbf{\Omega} = \begin{bmatrix} 0 & 0 & 0 & 0 & 0 & \cdots & 0 & 0 \\ 0 & 0 & -\omega_{sw} & 0 & 0 & \cdots & 0 & 0 \\ 0 & \omega_{sw} & 0 & 0 & 0 & \cdots & 0 & 0 \\ 0 & 0 & 0 & 0 & -2\omega_{sw} & \cdots & 0 & 0 \\ 0 & 0 & 0 & 2\omega_{sw} & 0 & \cdots & 0 & 0 \\ \vdots & \vdots & \vdots & \vdots & \vdots & \ddots & \vdots & \vdots \\ 0 & 0 & 0 & 0 & 0 & 0 & 0 & -N\omega_{sw} \\ 0 & 0 & 0 & 0 & 0 & 0 & N\omega_{sw} & 0 \end{bmatrix}. \tag{3.6}$$

The characteristics of the matrix $\mathbf{\Omega}$ are summarized in Equation 3.7-3.9. For an given integer m that satisfies the condition $1 < m \le N$,

$$\mathbf{\Omega}_{2m,2m+1} = -m\omega_{sw} \tag{3.7}$$

$$\mathbf{\Omega}_{2m+1,2m} = m\omega_{sw}, \tag{3.8}$$

and otherwise,

$$\mathbf{\Omega}_{j,k} = 0 \tag{3.9}$$

where j and k correspond to the j-th row and k-th column of matrix $\mathbf{\Omega}$. Since the time derivative of x has been expressed with vectors and matrices, it would be convenient to also express x in a similar manner. After substituting Equation 3.4 and 3.5 into Equation 3.1, x can be represented as

$$x = \mathbf{c x}. \tag{3.10}$$

Applying Equation 3.10 to the state variables of DC-DC converter yields

$$v = \mathbf{cv} \tag{3.11}$$

$$i = \mathbf{ci} \tag{3.12}$$

where v and i represent the capacitor voltage and inductor current. Similarly, the switching function q and the duty cycle command d can be represented as

$$q = \mathbf{cq} \tag{3.13}$$

$$d = \mathbf{cd}. \tag{3.14}$$

3.1.2 Carrier Signal Dependent Model of the Switching Function q
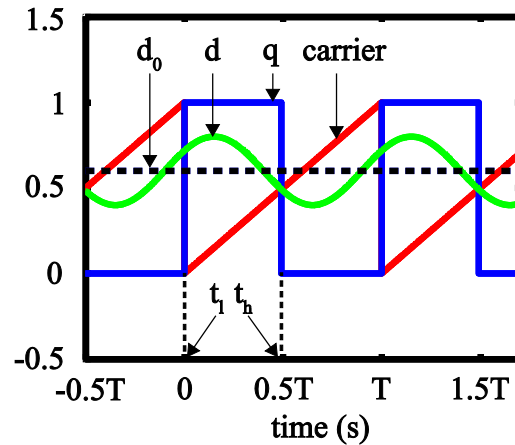
Figure 3.1 Switching function q, duty cycle command d, and sawtooth carrier signal

The model of switching function q is one of the major differences between GSSA and TIMF modeling techniques. In TIMF model, the switching function q is determined by comparing the duty cycle command and the carrier signal. This feature produces a carrier dependent switching function model, which is more realistic compared with the one in GSSA model. In a PWM converter, the switching function q can either be one or zero, representing the on and off state of the switch, respectively. As shown in Figure 3.1, when the duty cycle command d is greater than the carrier signal, q is set to one. Conversely, when the duty cycle

26

command d is less than the carrier signal, q is set to zero. The goal is to find a way to represent the switching function q that reflects this comparsion between the carrier signal and the duty cycle command. From Equation 3.1, the switching function q in QFS representation is given by

$$q = q_0 + \sum_{n=1}^{N} q_{\alpha_n} \cos(n\omega_{sw}t) + q_{\beta_n} \sin(n\omega_{sw}t) \tag{3.15}$$

where q_0, q_{α_n} and q_{β_n} are QFS coefficients. As shown in Figure 3.1, for a given switching period T, q is set to one between time t_l and t_h, and zero for the rest of the period. Hence, the QFS coefficients are computed as

$$q_0 = \frac{1}{T}\int_{t_l}^{t_h} q \cdot dt \tag{3.16}$$

$$q_{\alpha_n} = \frac{2}{T}\int_{t_l}^{t_h} q\cos(n\omega_{sw}t) \cdot dt \tag{3.17}$$

$$q_{\beta_n} = \frac{2}{T}\int_{t_l}^{t_h} q\sin(n\omega_{sw}t) \cdot dt. \tag{3.18}$$

Evaluating q_0, q_{α_n} and q_{β_n} yields

$$q_0 = \frac{t_h - t_l}{T} \tag{3.19}$$

$$q_{\alpha_n} = \frac{2}{n\omega_{sw}T}\left[\sin(n\omega_{sw}t_h) - \sin(n\omega_{sw}t_l)\right] \tag{3.20}$$

$$q_{\beta_n} = -\frac{2}{n\omega_{sw}T}\left[\cos(n\omega_{sw}t_h) - \cos(n\omega_{sw}t_l)\right]. \tag{3.21}$$

In order to simplify Equation 3.20 and 3.21, the following three properties are considered:

$$\sin u - \sin v = 2\cos\left(\frac{u+v}{2}\right)\sin\left(\frac{u-v}{2}\right) \tag{3.22}$$

$$\cos u - \cos v = -2\sin\left(\frac{u+v}{2}\right)\sin\left(\frac{u-v}{2}\right) \tag{3.23}$$

$$\omega_{sw} = \frac{2\pi}{T} \tag{3.24}$$

where u and v are any arbitrary functions or constants, Equation 3.20-3.21 evolve into

$$q_{\alpha_n} = \frac{2}{n\pi} \left[\cos\left(n\pi \frac{t_h + t_l}{T} \right) \sin\left(n\pi \frac{t_h - t_l}{T} \right) \right] \tag{3.25}$$

$$q_{\beta_n} = \frac{2}{n\pi} \left[\sin\left(n\pi \frac{t_h + t_l}{T} \right) \sin\left(n\pi \frac{t_h - t_l}{T} \right) \right]. \tag{3.26}$$

To further simplify the expressions for q_{α_n} and q_{β_n}, let

$$\delta = \frac{t_h - t_l}{T} \tag{3.27}$$

$$\phi = \pi \frac{t_h + t_l}{T}, \tag{3.28}$$

thus, Equation 3.25-3.26 become

$$q_{\alpha_n} = \frac{2}{n\pi} \left[\cos(n\phi)\sin(n\pi\delta) \right] \tag{3.29}$$

$$q_{\beta_n} = \frac{2}{n\pi} \left[\sin(n\phi)\sin(n\pi\delta) \right]. \tag{3.30}$$

If the values for t_l and t_h are known, then q_0, q_{α_n} and q_{β_n} can be determined for every period T using Equation 3.19, 3.29 and 3.30. This simplification from Equation 3.20 and 3.21 to Equation 3.29 and 3.30 may seem trivial at first glance, however a few good reasons make these extra steps meaningful. First, $\frac{t_h}{T}$ and $\frac{t_l}{T}$ are dimensionless numbers that represents fractions of the period T, which have a range between 0 and 1, whereas t_h and t_l from Equation 3.20 and 3.21 have units in seconds, which increase with simulation time and are difficult to solve for every single period. Second, $\frac{t_h + t_l}{T}$ and $\frac{t_h - t_l}{T}$, as will be discussed later, have special implications to the average of the duty cycle command, which can be used directly for simplifying the calculations.

28

In addition to trigonometric representation of the switching function q, as shown in Equation 3.15, q can also be expressed in the compact trigonometric form

$$q = q_0 + \sum_{n=1}^{N} q_{c_n} \cos(n\omega_{sw}t + \theta_n) \qquad (3.31)$$

where

$$q_{c_n} = \sqrt{q_{\alpha_n}^2 + q_{\beta_n}^2} \qquad (3.32)$$

$$\theta_n = \tan^{-1}\left(\frac{-q_{\beta_n}}{q_{\alpha_n}}\right). \qquad (3.33)$$

Substituting $q_{\alpha n}$ and $q_{\beta n}$ into Equation 3.32 and 3.33 with Equation 3.29 and 3.30 yields

$$q_{c_n} = \frac{2}{n\pi} \sin(n\pi\delta) \qquad (3.34)$$

$$\theta_n = -n\phi. \qquad (3.35)$$

By using Equation 3.27, 3.34 and 3.35, Equation 3.31 becomes

$$q = \delta + \sum_{n=1}^{N} \frac{2}{n\pi} \sin(n\pi\delta)\cos(n\omega_{sw}t - n\phi). \qquad (3.36)$$

This expression of the switching function q has been shown in many power electronics textbooks and related publications [46], [86]. This confirms that legitimacy of model of q developed in Equations 3.19, 3.29 and 3.30.

Continuing the discussion of the QFS coefficients of switching function q, since the switching frequency ω_{sw} is assumed to be constant in a given PWM DC-DC converter, the only unknowns in Equation 3.29 and 3.30 are δ and ϕ. As clearly shown in Equation 3.36, the symbol ϕ is the phase shift of the switching function. The graphical representation of ϕ is shown in Figure 3.2. In order to show this mathematically, expressing Equation 3.27 in terms of ω_{sw} yields

$$\phi = \omega_{sw} \frac{t_h + t_l}{2} .$$ (3.37)

Let $t_0 = \dfrac{t_h + t_l}{2}$, the phase shift becomes

$$\phi = \omega_{sw} t_0 .$$ (3.38)
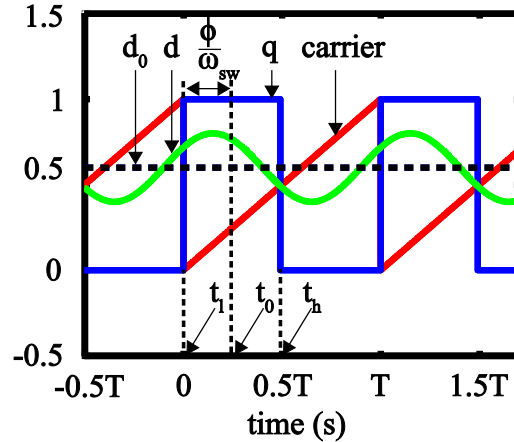
Figure 3.2 Switching function q , duty cycle command d , and sawtooth carrier signal and phase shift ϕ

The second unknown is δ . Based on expression of δ in Equation 3.27 and the observation made from Figure 3.2, one can conclude that δ is equivalent to duty cycle command d over a given switching period. However, there is a small difference between the two variables. δ is the duty cycle of switching function q over a given period T . On the other hand, d is the desired duty cycle at anytime t . Therefore, δ is in fact the average of d for a given period T .

In order to determine the values for ϕ and δ , one must locate t_l and t_h for a given switching period T of the switching signal. From Figure 3.2, it is obvious that the location of t_h is where the duty cycle command intersects with the sawtooth carrier signal, and the location of t_l is the beginning of every period. Since t_l is defined as the beginning of cycle of the switching signal q , for the case of sawtooth carrier signal, its relative position is always equals to zero in a period. In order to find t_h , one have to equate the duty cycle command d and the carrier

signal, then locate the point of intersection in relative to the switching period. By using Equation 3.1, the duty cycle command is expressed as

$$d = d_0 + \sum_{n=1}^{N} d_{\alpha_n} \cos(n\omega_{sw}t) + d_{\beta_n} \sin(n\omega_{sw}t)$$ (3.39)

where d_0, d_{α_n} and d_{β_n} are QFS coefficients, and d_0 is the average value of the duty cycle. In a given period T, the sawtooth carrier signal $s_{sawtooth}$ can be expressed as a continuous function of time

$$s_{sawtooth} = \frac{h_{sawtooth}}{T} t$$ (3.40)

where $h_{sawtooth}$ is the maximum height of the sawtooth signal and t is time in seconds. As shown in Figure 3.2, at $t = t_h$, Equation 3.39 equals to Equation 3.40, and by assuming $h_{sawtooth} = 1$, the resulting equation is give by

$$\frac{t_h}{T} = d_0 + \sum_{n=1}^{N} d_{\alpha_n} \cos(n\omega_{sw}t_h) + d_{\beta_n} \sin(n\omega_{sw}t_h).$$ (3.41)

Moving the duty cycle command to the left side in Equation 3.41 yields

$$\frac{t_h}{T} - \left[d_0 + \sum_{n=1}^{N} d_{\alpha_n} \cos(n\omega_{sw}t_h) + d_{\beta_n} \sin(n\omega_{sw}t_h) \right] = 0.$$ (3.42)

Finally, an expression with the only one unknown variable t_h has been established in Equation 3.42. However, analytically solving for t_h is quite complicated. For this reason an iterative method, Newton-Raphson's method [74], has been used to find t_h.

Newton Raphson's method is an iterative method to estimate the root x of a given function $f(x)$. The convergence of Newton Raphson's method depends on the nature of the function and the intial guess value for x. If the convergence exists, the root x can be found through iteration method

$$x_{i+1} = x_i - \frac{f(x_i)}{f'(x_i)},$$ (3.43)

where i is the number of iterations, and $f'(x)$ is the derivative with respect to x. As more iteration has been performed, x_i become closer and closer to the root of $f(x)$. As the result, the error between x_i and x_{i+1} also becomes smaller than the previous iteration. The iteration process terminates when the error reduces to a predetermined value.

In this thesis, Newton Raphson's method has been applied to Equation 3.42 for find $\frac{t_h}{T}$. First, one needs to define $f(x)$, which is in the form

$$f(x) = \frac{t_h}{T} - \left[d_0 + \sum_{n=1}^{N} d_{\alpha_n} \cos(n\omega_{sw}t_h) + d_{\beta_n} \sin(n\omega_{sw}t_h) \right].$$ (3.44)

Since $x_i = \frac{t_h}{T}$, rewriting Equation 3.44 as

$$f(x) = \frac{t_h}{T} - \left[d_0 + \sum_{n=1}^{N} d_{\alpha_n} \cos\left(2\pi n \frac{t_h}{T}\right) + d_{\beta_n} \sin\left(2\pi n \frac{t_h}{T}\right) \right].$$ (3.45)

For simplicity, only the first harmonic of the duty cycle command is considered ($N = 1$). This assumption is valid because the first harmonic often dominates the ripples in the state variables, and in a closed-loop controlled DC-DC converter, a low pass filter is often employed in the feedback loop of the controller signal, thus further reduces the impact of higher frequency components of the duty cycle command signal. For $N = 1$, the derivative of Equation 3.46 with respect to $\frac{t_h}{T}$ is given by

$$f'(x) = 1 + 2\pi d_{\alpha_1} \sin\left(2\pi \frac{t_h}{T}\right) - 2\pi d_{\beta_1} \cos\left(2\pi \frac{t_h}{T}\right).$$ (3.46)

Consequently, with the initial guess $\frac{t_h}{T} = d_0$, the value of $\frac{t_h}{T}$ can be approximated by the following expression,

32

$$\frac{t_h}{T} \approx d_0 + \frac{d_{\alpha_1} \cos(2\pi d_0) + d_{\beta_1} \sin(2\pi d_0)}{1 + 2\pi d_{\alpha_1} \sin(2\pi d_0) - 2\pi d_{\beta_1} \cos(2\pi d_0)}.$$ (3.47)

Therefore,

$$t_h \approx T\left(d_0 + \frac{d_{\alpha_1} \cos(2\pi d_0) + d_{\beta_1} \sin(2\pi d_0)}{1 + 2\pi d_{\alpha_1} \sin(2\pi d_0) - 2\pi d_{\beta_1} \cos(2\pi d_0)} \right).$$ (3.48)

With knowing the values of t_l and t_h in the sawtooth carrier signal, the QFS coefficients of switching function q can be found using Equations 3.19, 3.25 and 3.26.

Another type of carrier signal is the isosceles triangular carrier. Although isosceles triangular carrier is rarely used for DC-DC converter, it has proven to be useful for other types of PWM converters. For instance, in PWM inverters, implementing a triangular carrier signal can reduce the baseband distortion [71]. Also, comparing to sawtooth carrier, triangular carrier is more suitable for PWM controllers operated at high switching frequency (greater than 1MHz) because two control actions can be taken in one switching period. The fast reset in sawtooth carrier has been replaced by the two equal ramps in triangular carrier for better stability and control. [61].
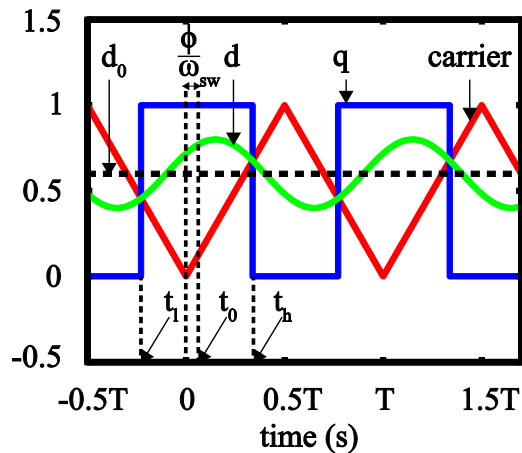
Figure 3.3 Switching function q, duty cycle command d, and isosceles triangular carrier signal and phase shift ϕ

As demonstrated in Figure 3.3, when the triangular carrier signal is used, the switching function q still equals to one between t_l and t_h, and equals to zero otherwise. However, t_l no longer equals to zero. Therefore, in order to model the switching function q with the triangular carrier signal, one has to first solve for both t_l and t_h. From Figure 3.3, it is obvious that the isosceles triangular carrier signal $s_{triangular}$ consists of two piece-wise linear function for every period of T

$$s_{triangular} = -\frac{h_{triangular}}{0.5T}t + h_{triangular} \qquad -\frac{T}{2} < t \le 0 \tag{3.49}$$

$$s_{triangular} = \frac{h_{triangular}}{0.5T}t \qquad 0 < t \le \frac{T}{2} \tag{3.50}$$

During $-\frac{T}{2} < t \le 0$, an expression with only t_l can be found by equating the carrier signal $s_{triangular}$ (Equation 3.49) with the duty cycle command d (Equation 3.39) at time $t = t_l - (-0.5T)$, as shown in Equation 3.47. Similarly, an expression with only t_h is found by equating Equation 3.50 and Equation 3.39 at time $t = t_h$, as presented in Equation 3.52.

$$-\frac{h_{triangular}}{0.5T}\left(t_l - (-0.5T)\right) + h_{triangular} = d_0 + \sum_{n=1}^{N} d_{\alpha_n} \cos\left(n\omega_{sw}\left(t_l - (-0.5T)\right)\right) +$$

$$d_{\beta_n} \sin\left(n\omega_{sw}\left(t_l - (-0.5T)\right)\right) \tag{3.51}$$

$$\frac{h_{triangular}}{0.5T}t_h = d_0 + \sum_{n=1}^{N} d_{\alpha_n} \cos\left(n\omega_{sw}t_h\right) + d_{\beta_n} \sin\left(n\omega_{sw}t_h\right) \tag{3.52}$$

Similar to the sawtooth carrier case, in Equation 3.51 and 3.52, ω_{sw} has been replaced with $\frac{2\pi}{T}$. Assuming $h_{triangular} = 1$, and $N = 1$, the simplified version of Equation 3.51 and 3.52 are given by

$$-2\frac{t_l}{T} \approx d_0 + d_{\alpha_1} \cos\left(2\pi \frac{t_l}{T} + \pi\right) + d_{\beta_1} \sin\left(2\pi \frac{t_l}{T} + \pi\right) \tag{3.53}$$

$$2\frac{t_h}{T} \approx d_0 + d_{\alpha_1} \cos\left(2\pi \frac{t_h}{T}\right) + d_{\beta_1} \sin\left(2\pi \frac{t_h}{T}\right). \tag{3.54}$$

In order to use Newton Raphson's method, moving the right hand sides of Equations 3.53 and 3.54 to the left hand sides yields

$$-2\frac{t_l}{T} - \left[d_0 - d_{\alpha_1} \cos\left(2\pi \frac{t_l}{T}\right) - d_{\beta_1} \sin\left(2\pi \frac{t_l}{T}\right)\right] = 0 \tag{3.55}$$

$$2\frac{t_h}{T} - \left[d_0 + d_{\alpha_1} \cos\left(2\pi \frac{t_h}{T}\right) + d_{\beta_1} \sin\left(2\pi \frac{t_h}{T}\right)\right] = 0. \tag{3.56}$$

By applying Newton Raphson's method with initial guesses $\frac{t_l}{T} = -\frac{d_0}{2}$ and $\frac{t_h}{T} = \frac{d_0}{2}$, the estimation for $\frac{t_l}{T}$ and $\frac{t_h}{T}$ are given by

$$\frac{t_l}{T} \approx -\frac{d_0}{2} - \left(\frac{d_{\alpha_1} \cos(-\pi d_0) + d_{\beta_1} \sin(-\pi d_0)}{-2 - 2\pi d_{\alpha_1} \sin(-\pi d_0) + 2\pi d_{\beta_1} \cos(-\pi d_0)}\right) \tag{3.57}$$

$$\frac{t_h}{T} \approx \frac{d_0}{2} - \left(\frac{-d_{\alpha_1} \cos(\pi d_0) - d_{\beta_1} \sin(\pi d_0)}{2 + 2\pi d_{\alpha_1} \sin(\pi d_0) - 2\pi d_{\beta_1} \cos(\pi d_0)}\right). \tag{3.58}$$

Therefore,

$$t_l \approx T\left[-\frac{d_0}{2} - \left(\frac{d_{\alpha_1} \cos(\pi d_0) - d_{\beta_1} \sin(\pi d_0)}{-2 + 2\pi d_{\alpha_1} \sin(\pi d_0) + 2\pi d_{\beta_1} \cos(\pi d_0)}\right)\right] \tag{3.59}$$

$$t_h \approx T\left[\frac{d_0}{2} - \left(\frac{-d_{\alpha_1} \cos(\pi d_0) - d_{\beta_1} \sin(\pi d_0)}{2 + 2\pi d_{\alpha_1} \sin(\pi d_0) - 2\pi d_{\beta_1} \cos(\pi d_0)}\right)\right]. \tag{3.60}$$

By substituting the expressions of t_l and t_h into Equation 3.19, 3.25 and 3.26, QFS coefficients q_0, q_{α_1} and q_{β_1} can be solved. This concludes the model of the switching function q in the case of isosceles triangular carrier signal.

3.1.3 Computation of the Product of State Variable x and Switching Function q

The state space model of PWM converters often involves the multiplication of the switching function q and state variable x. For this reason, this sub-section is dedicated to finding the TIMF representation of the product of the switching function q and the state variable x. The product g of the switching function q and any state variable x is given by

$$g = qx . \tag{3.61}$$

Due to the dynamic behavior of g, it can also be represented by QFS. Hence,

$$g = g_0 + \sum_{n=1}^{N} g_{\alpha_1} \cos(n\omega_{sw}t) + g_{\beta_1} \sin(n\omega_{sw}t), \tag{3.62}$$

where g_0, g_{α_1} and g_{β_1} are the QFS coefficients of g. The objective is to define these QFS coefficients in terms of QFS coefficients of q and x. For accomplishing this objective, first substituting x with Equation 3.1 and q with Equation 3.15 into Equation 3.61 yields

$$g = \left(q_0 + \sum_{n=1}^{N} q_{\alpha_n} \cos(n\omega_{sw}t) + q_{\beta_n} \sin(n\omega_{sw}t) \right) \cdot$$

$$\left(x_0 + \sum_{n=1}^{N} x_{\alpha_n} \cos(n\omega_{sw}t) + x_{\beta_n} \sin(n\omega_{sw}t) \right) \tag{3.63}$$

In many cases, this product g can be well approximated by only two harmonics. For this reason, with assumption of $N = 2$, Equation 3.63 becomes

$$g = \left(q_0 + q_{\alpha_1} \cos(\omega_{sw}t) + q_{\beta_1} \sin(\omega_{sw}t) + q_{\alpha_2} \cos(2\omega_{sw}t) + q_{\beta_2} \sin(2\omega_{sw}t) \right) \cdot$$

$$\left(x_0 + x_{\alpha_1}\cos(\omega_{sw}t) + x_{\beta_1}\sin(\omega_{sw}t) + x_{\alpha_2}\cos(2\omega_{sw}t) + x_{\beta_2}\sin(2\omega_{sw}t)\right). \tag{3.64}$$

By applying distributive property of multiplication to Equation 3.64, the result is given by Equation 3.65.

$$g = q_0 x_0 + q_{\alpha_1} x_0 \cos(\omega_{sw}t) + q_{\beta_1} x_0 \sin(\omega_{sw}t) + q_{\alpha_2} x_0 \cos(2\omega_{sw}t) +$$

$$q_{\beta_2} x_0 \sin(2\omega_{sw}t) + q_0 x_{\alpha_1}\cos(\omega_{sw}t) + q_{\alpha_1} x_{\alpha_1}\cos^2(\omega_{sw}t) +$$

$$q_{\beta_1} x_{\alpha_1}\sin(\omega_{sw}t)\cos(\omega_{sw}t) + q_{\alpha_2} x_{\alpha_1}\cos(2\omega_{sw}t)\cos(\omega_{sw}t) +$$

$$q_{\beta_2} x_{\alpha_1}\sin(2\omega_{sw}t)\cos(\omega_{sw}t) + q_0 x_{\beta_1}\sin(\omega_{sw}t) +$$

$$q_{\alpha_1} x_{\beta_1}\cos(\omega_{sw}t)\sin(\omega_{sw}t) + q_{\beta_1} x_{\beta_1}\sin^2(\omega_{sw}t) +$$

$$q_{\alpha_2} x_{\beta_1}\cos(2\omega_{sw}t)\sin(\omega_{sw}t) + q_{\beta_2} x_{\beta_1}\sin(2\omega_{sw}t)\sin(\omega_{sw}t) +$$

$$q_0 x_{\alpha_2}\cos(2\omega_{sw}t) + q_{\alpha_1} x_{\alpha_2}\cos(\omega_{sw}t)\cos(2\omega_{sw}t) +$$

$$q_{\beta_1} x_{\alpha_2}\sin(\omega_{sw}t)\cos(2\omega_{sw}t) + q_{\alpha_2} x_{\alpha_2}\cos^2(2\omega_{sw}t) +$$

$$q_{\beta_2} x_{\alpha_2}\sin(2\omega_{sw}t)\cos(2\omega_{sw}t) + q_0 x_{\beta_2}\sin(2\omega_{sw}t) +$$

$$q_{\alpha_1} x_{\beta_2}\cos(\omega_{sw}t)\sin(2\omega_{sw}t) + q_{\beta_1} x_{\beta_2}\sin(\omega_{sw}t)\sin(2\omega_{sw}t) +$$

$$q_{\alpha_2} x_{\beta_2}\cos(2\omega_{sw}t)\sin(2\omega_{sw}t) + q_{\beta_2} x_{\beta_2}\sin^2(2\omega_{sw}t). \tag{3.65}$$

In order to identity different frequency components, by applying the trigonometric properties as given in Equations 3.66-3.73 to Equation 3.62, the result is given in Equation 3.74.

$$\sin u \sin v = \frac{1}{2}[\cos(u-v) - \cos(u+v)] \tag{3.66}$$

$$\cos u \cos v = \frac{1}{2}[\cos(u-v) + \cos(u+v)] \tag{3.67}$$

$$\sin^2(u) = \frac{1-\cos(2u)}{2} \tag{3.68}$$

$$\cos^2(u) = \frac{1 + \cos(2u)}{2} \tag{3.69}$$

$$\sin u \cos v = \frac{1}{2}[\sin(u + v) + \sin(u - v)] \tag{3.70}$$

$$\cos u \sin v = \frac{1}{2}[\sin(u + v) - \sin(u - v)] \tag{3.71}$$

$$\cos(-u) = \cos u \tag{3.72}$$

$$\sin(-u) = -\sin u \tag{3.73}$$

where u and v are any arbitrary functions or constants.

$$g = q_0 x_0 + q_{\alpha_1} x_0 \cos(\omega_{sw} t) + q_{\beta_1} x_0 \sin(\omega_{sw} t) + q_{\alpha_2} x_0 \cos(2\omega_{sw} t) +$$

$$q_{\beta_2} x_0 \sin(2\omega_{sw} t) + q_0 x_{\alpha_1} \cos(\omega_{sw} t) + \frac{q_{\alpha_1} x_{\alpha_1}}{2} + \frac{q_{\alpha_1} x_{\alpha_1}}{2} \cos(2\omega_{sw} t) +$$

$$\frac{q_{\beta_1} x_{\alpha_1}}{2} \sin(2\omega_{sw} t) + \frac{q_{\alpha_2} x_{\alpha_1}}{2} \cos(\omega_{sw} t) + \frac{q_{\alpha_2} x_{\alpha_1}}{2} \cos(3\omega_{sw} t) +$$

$$\frac{q_{\beta_2} x_{\alpha_1}}{2} \sin(3\omega_{sw} t) + \frac{q_{\beta_2} x_{\alpha_1}}{2} \sin(\omega_{sw} t) + q_0 x_{\beta_1} \sin(\omega_{sw} t) +$$

$$\frac{q_{\alpha_1} x_{\beta_1}}{2} \sin(2\omega_{sw} t) + \frac{q_{\beta_1} x_{\beta_1}}{2} - \frac{q_{\beta_1} x_{\beta_1}}{2} \cos(2\omega_{sw} t) +$$

$$\frac{q_{\alpha_2} x_{\beta_1}}{2} \sin(3\omega_{sw} t) - \frac{q_{\alpha_2} x_{\beta_1}}{2} \sin(\omega_{sw} t) + \frac{q_{\beta_2} x_{\beta_1}}{2} \cos(\omega_{sw} t) -$$

$$\frac{q_{\beta_2} x_{\beta_1}}{2} \cos(3\omega_{sw} t) + q_0 x_{\alpha_2} \cos(2\omega_{sw} t) + \frac{q_{\alpha_1} x_{\alpha_2}}{2} \cos(\omega_{sw} t) +$$

$$\frac{q_{\alpha_1} x_{\alpha_2}}{2} \cos(3\omega_{sw} t) + \frac{q_{\beta_1} x_{\alpha_2}}{2} \sin(3\omega_{sw} t) - \frac{q_{\beta_1} x_{\alpha_2}}{2} \sin(\omega_{sw} t) + \frac{q_{\alpha_2} x_{\alpha_2}}{2} +$$

$$\frac{q_{\alpha_2} x_{\alpha_2}}{2} \cos(4\omega_{sw} t) + \frac{q_{\beta_2} x_{\alpha_2}}{2} \sin(4\omega_{sw} t) + q_0 x_{\beta_2} \sin(2\omega_{sw} t) +$$

$$\frac{q_{\alpha_1} x_{\beta_2}}{2} \sin(3\omega_{sw} t) + \frac{q_{\alpha_1} x_{\beta_2}}{2} \sin(\omega_{sw} t) + \frac{q_{\beta_1} x_{\beta_2}}{2} \cos(\omega_{sw} t) -$$

$$\frac{q_{\beta_1} x_{\beta_2}}{2} \cos(3\omega_{sw}t) + \frac{q_{\alpha_2} x_{\beta_2}}{2} \sin(4\omega_{sw}t) + \frac{q_{\beta_2} x_{\beta_2}}{2} - \frac{q_{\beta_2} x_{\beta_2}}{2} \cos(4\omega_{sw}t).$$ (3.74)

Since only harmonics of $N \le 2$ are considered, the terms in Equation 3.74 with $\cos(3\omega_{sw}t)$, $\sin(3\omega_{sw}t)$, $\cos(4\omega_{sw}t)$, and $\sin(4\omega_{sw}t)$ are discarded. Therefore,

$$g = q_0 x_0 + q_{\alpha_1} x_0 \cos(\omega_{sw}t) + q_{\beta_1} x_0 \sin(\omega_{sw}t) + q_{\alpha_2} x_0 \cos(2\omega_{sw}t) +$$

$$q_{\beta_2} x_0 \sin(2\omega_{sw}t) + q_0 x_{\alpha_1} \cos(\omega_{sw}t) + \frac{q_{\alpha_1} x_{\alpha_1}}{2} + \frac{q_{\alpha_1} x_{\alpha_1}}{2} \cos(2\omega_{sw}t) +$$

$$\frac{q_{\beta_1} x_{\alpha_1}}{2} \sin(2\omega_{sw}t) + \frac{q_{\alpha_2} x_{\alpha_1}}{2} \cos(\omega_{sw}t) + \frac{q_{\beta_2} x_{\alpha_1}}{2} \sin(\omega_{sw}t) +$$

$$q_0 x_{\beta_1} \sin(\omega_{sw}t) + \frac{q_{\alpha_1} x_{\beta_1}}{2} \sin(2\omega_{sw}t) + \frac{q_{\beta_1} x_{\beta_1}}{2} - \frac{q_{\beta_1} x_{\beta_1}}{2} \cos(2\omega_{sw}t) -$$

$$\frac{q_{\alpha_2} x_{\beta_1}}{2} \sin(\omega_{sw}t) + \frac{q_{\beta_2} x_{\beta_1}}{2} \cos(\omega_{sw}t) + q_0 x_{\alpha_2} \cos(2\omega_{sw}t) +$$

$$\frac{q_{\alpha_1} x_{\alpha_2}}{2} \cos(\omega_{sw}t) - \frac{q_{\beta_1} x_{\alpha_2}}{2} \sin(\omega_{sw}t) + \frac{q_{\alpha_2} x_{\alpha_2}}{2} + q_0 x_{\beta_2} \sin(2\omega_{sw}t) +$$

$$\frac{q_{\alpha_1} x_{\beta_2}}{2} \sin(\omega_{sw}t) + \frac{q_{\beta_1} x_{\beta_2}}{2} \cos(\omega_{sw}t) + \frac{q_{\beta_2} x_{\beta_2}}{2}.$$ (3.75)

After equating the QFS coefficients in the product g described in Equation 3.62 and Equation 3.75, the result is given by

$$g_0 = q_0 x_0 + \frac{q_{\alpha_1} x_{\alpha_1}}{2} + \frac{q_{\beta_1} x_{\beta_1}}{2} + \frac{q_{\alpha_2} x_{\alpha_2}}{2} + \frac{q_{\beta_2} x_{\beta_2}}{2},$$ (3.76)

$$g_{\alpha_1} = q_{\alpha_1} x_0 + q_0 x_{\alpha_1} + \frac{q_{\alpha_2} x_{\alpha_1}}{2} + \frac{q_{\beta_2} x_{\beta_1}}{2} + \frac{q_{\alpha_1} x_{\alpha_2}}{2} + \frac{q_{\beta_1} x_{\beta_2}}{2},$$ (3.77)

$$g_{\beta_1} = q_{\beta_1} x_0 + \frac{q_{\beta_2} x_{\alpha_1}}{2} + q_0 x_{\beta_1} - \frac{q_{\alpha_2} x_{\beta_1}}{2} - \frac{q_{\beta_1} x_{\alpha_2}}{2} + \frac{q_{\alpha_1} x_{\beta_2}}{2},$$ (3.78)

$$g_{\alpha_2} = q_{\alpha_2} x_0 + \frac{q_{\alpha_1} x_{\alpha_1}}{2} - \frac{q_{\beta_1} x_{\beta_1}}{2} + q_0 x_{\alpha_2},$$ (3.79)

$$g_{\beta_2} = q_{\beta_2} x_0 + \frac{q_{\beta_1} x_{\alpha_1}}{2} + \frac{q_{\alpha_1} x_{\beta_1}}{2} + q_0 x_{\beta_2} .$$ (3.80)

Finally, g can be represented in the compact form as

$$g = \mathbf{cg} ,$$ (3.81)

where

$$\mathbf{c} = \begin{bmatrix} 1 & \cos(\omega_{sw}t) & \sin(\omega_{sw}t) & \cos(2\omega_{sw}t) & \sin(2\omega_{sw}t) \end{bmatrix} ,$$ (3.82)

and

$$\mathbf{g} = \begin{bmatrix} q_0 x_0 + \dfrac{q_{\alpha_1} x_{\alpha_1}}{2} + \dfrac{q_{\beta_1} x_{\beta_1}}{2} + \dfrac{q_{\alpha_2} x_{\alpha_2}}{2} + \dfrac{q_{\beta_2} x_{\beta_2}}{2} \\[2mm] q_{\alpha_1} x_0 + q_0 x_{\alpha_1} + \dfrac{q_{\alpha_2} x_{\alpha_1}}{2} + \dfrac{q_{\beta_2} x_{\beta_1}}{2} + \dfrac{q_{\alpha_1} x_{\alpha_2}}{2} + \dfrac{q_{\beta_1} x_{\beta_2}}{2} \\[2mm] q_{\beta_1} x_0 + \dfrac{q_{\beta_2} x_{\alpha_1}}{2} + q_0 x_{\beta_1} - \dfrac{q_{\alpha_2} x_{\beta_1}}{2} - \dfrac{q_{\beta_1} x_{\alpha_2}}{2} + \dfrac{q_{\alpha_1} x_{\beta_2}}{2} \\[2mm] q_{\alpha_2} x_0 + \dfrac{q_{\alpha_1} x_{\alpha_1}}{2} - \dfrac{q_{\beta_1} x_{\beta_1}}{2} + q_0 x_{\alpha_2} \\[2mm] q_{\beta_2} x_0 + \dfrac{q_{\beta_1} x_{\alpha_1}}{2} + \dfrac{q_{\alpha_1} x_{\beta_1}}{2} + q_0 x_{\beta_2} \end{bmatrix} .$$ (3.83)

After recalling the vector representation of QFS coefficients $\mathbf{x}$ as defined in Equation 3.4, Equation 3.83 can be also expressed as

$$\mathbf{g} = \mathbf{Qx} ,$$ (3.84)

where $\mathbf{Q}$ is a 5 by 5 matrix, given by

$$\mathbf{Q} = \begin{bmatrix} q_0 & \dfrac{q_{\alpha_1}}{2} & \dfrac{q_{\beta_1}}{2} & \dfrac{q_{\alpha_2}}{2} & \dfrac{q_{\beta_2}}{2} \\[2mm] q_{\alpha_1} & q_0 + \dfrac{q_{\alpha_2}}{2} & \dfrac{q_{\beta_2}}{2} & \dfrac{q_{\alpha_1}}{2} & \dfrac{q_{\beta_1}}{2} \\[2mm] q_{\beta_1} & \dfrac{q_{\beta_2}}{2} & q_0 - \dfrac{q_{\alpha_2}}{2} & -\dfrac{q_{\beta_1}}{2} & \dfrac{q_{\alpha_1}}{2} \\[2mm] q_{\alpha_2} & \dfrac{q_{\alpha_1}}{2} & -\dfrac{q_{\beta_1}}{2} & q_0 & 0 \\[2mm] q_{\beta_2} & \dfrac{q_{\beta_1}}{2} & \dfrac{q_{\alpha_1}}{2} & 0 & q_0 \end{bmatrix} .$$ (3.85)

This separation of the QFS coefficients of the state variable x from the product g is an essential part of the TIMF model, because TIMF model describes the system with QFS coefficients of the state variable, not the state variable itself as in the original state space model. Conversely, if the QFS coefficients vector of the switching function q is given by

$$\mathbf{q}^{\mathrm{T}} = \begin{bmatrix} q_0 & q_{\alpha_1} & q_{\beta_1} & q_{\alpha_2} & q_{\beta_2} \end{bmatrix}, \tag{3.86}$$

then Equation 3.74 can also be written as

$$\mathbf{g} = \mathbf{X}\mathbf{q}, \tag{3.87}$$

where $\mathbf{X}$ is a 5 by 5 matrix

$$\mathbf{X} = \begin{bmatrix} x_0 & \dfrac{x_{\alpha_1}}{2} & \dfrac{x_{\beta_1}}{2} & \dfrac{x_{\alpha_2}}{2} & \dfrac{x_{\beta_2}}{2} \\[2mm] x_{\alpha_1} & x_0 + \dfrac{x_{\alpha_2}}{2} & \dfrac{x_{\beta_2}}{2} & \dfrac{x_{\alpha_1}}{2} & \dfrac{x_{\beta_1}}{2} \\[2mm] x_{\beta_1} & \dfrac{x_{\beta_2}}{2} & x_0 - \dfrac{x_{\alpha_2}}{2} & -\dfrac{x_{\beta_1}}{2} & \dfrac{x_{\alpha_1}}{2} \\[2mm] x_{\alpha_2} & \dfrac{x_{\alpha_1}}{2} & -\dfrac{x_{\beta_1}}{2} & x_0 & 0 \\[2mm] x_{\beta_2} & \dfrac{x_{\beta_1}}{2} & \dfrac{x_{\alpha_1}}{2} & 0 & x_0 \end{bmatrix}. \tag{3.88}$$

Equation 3.87 becomes useful when one tries to linearize the TIMF model. Details of linearization is discussed in [46]. Due to neglect of higher order harmonics, g can be estimated as

$$g \approx \mathbf{c}(\mathbf{Q}\mathbf{x}), \tag{3.89}$$

or

$$g \approx \mathbf{c}(\mathbf{X}\mathbf{q}). \tag{3.90}$$

<u>3.2 Case Study for Cuk Converter</u>

3.2.1 Model Construction

The schematic of the Cuk converter with parasitic elements is shown in Figure 3.4. In CCM, the Cuk converter has two switching states. In the first switching state, as shown in

41

Figure 3.5(a), the switching function q is on, and the diode is reversely biased. As a result, the MOSFET is replaced by a resistor r_m to account for the conduction loss, and the branch containing the diode is opened. In the second switching state, as shown in Figure 3.5(b), the switching function q is off, and the diode conducts. Thus, the MOSFET branch is opened, and the diode is replaced by a resistor r_d to account for the conduction loss, and a voltage source v_d to account for the forward voltage drop.
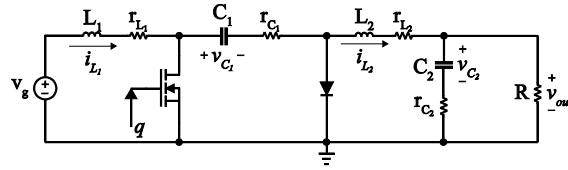
Figure 3.4 Cuk converter with parasitic elements

(a)

(b)
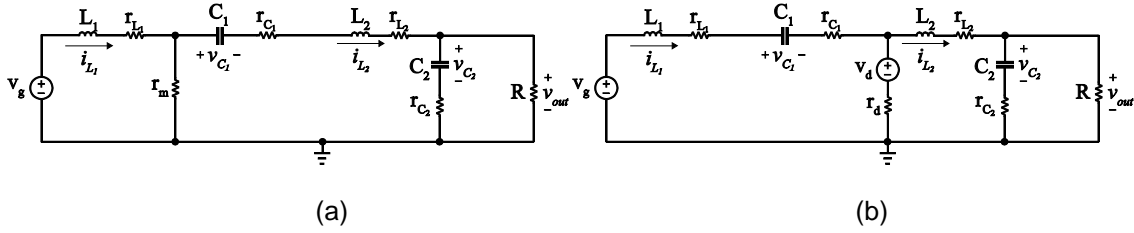
Figure 3.5 Cuk converter in CCM: (a) when q is on and (b) when q is off

Therefore, the state space model of the Cuk converter is given by

$$L_1 \frac{di_{L_1}}{dt} = q\left[v_g - r_{L_1}i_{L_1} - r_m\left(i_{L_1} - i_{L_2}\right)\right] +$$

$$\left(1 - q\right)\left[v_g - v_{C_1} - \left(r_{L_1} + r_{C_1}\right)i_{L_1} - v_d - r_d\left(i_{L_1} - i_{L_2}\right)\right] \tag{3.91}$$

$$L_2 \frac{di_{L_2}}{dt} =$$

$$q\left[-v_{C_1} - r_{C_1}i_{L_2} - r_{L_2}i_{L_2} - v_{C_2} - r_{C_2}\left(i_{L_2} - \frac{v_{C_2} + r_{C_2}i_{L_2}}{r_{C_2} + R}\right) - r_m\left(i_{L_2} - i_{L_1}\right)\right] +$$

42

$$(1-q)\left[-r_{L_2}i_{L_2} - v_{C_2} - r_{C_2}\left(i_{L_2} - \frac{v_{C_2} + r_{C_2}i_{L_2}}{r_{C_2} + R}\right) + v_d - r_d\left(i_{L_2} - i_{L_1}\right)\right] \tag{3.92}$$

$$C_1 \frac{dv_{C_1}}{dt} = qi_{L_2} + (1-q)i_{L_1} \tag{3.93}$$

$$C_2 \frac{dv_{C_2}}{dt} = q\left(i_{L_2} - \frac{v_{C_2} + r_{C_2}i_{L_2}}{r_{C_2} + R}\right) + (1-q)\left(i_{L_2} - \frac{v_{C_2} + r_{C_2}i_{L_2}}{r_{C_2} + R}\right). \tag{3.94}$$

As shown in Equation 3.94, the capacitor current remains the same expression in both switching states. Further simplifying Equations 3.91-3.94 yields

$$L_1 \frac{di_{L_1}}{dt} = q\left[-\left(r_{L_1} + r_m\right)i_{L_1} + r_m i_{L_2}\right] +$$

$$(1-q)\left[-\left(r_{L_1} + r_{C_1} + r_d\right)i_{L_1} + r_d i_{L_2} - v_{C_1}\right] + \left[qv_g + (1-q)\left(v_g - v_d\right)\right] \tag{3.95}$$

$$L_2 \frac{di_{L_2}}{dt} =$$

$$q\left[r_m i_{L_1} - \left(r_{C_1} + r_{L_2} + r_{C_2} - \frac{r_{C_2}^2}{r_{C_2} + R} + r_m\right)i_{L_2} - v_{C_1} - \left(1 - \frac{r_{C_2}}{r_{C_2} + R}\right)v_{C_2}\right] +$$

$$(1-q)\left[r_d i_{L_1} - \left(r_{L_2} + r_{C_2} - \frac{r_{C_2}^2}{r_{C_2} + R} + r_d\right)i_{L_2} - \left(1 - \frac{r_{C_2}}{r_{C_2} + R}\right)v_{C_2}\right] + (1-q)v_d \tag{3.96}$$

$$C_1 \frac{dv_{C1}}{dt} = qi_{L_2} + (1-q)i_{L1} \tag{3.97}$$

$$C_2 \frac{dv_{C_2}}{dt} = \left(1 - \frac{r_{C_2}}{r_{C_2} + R}\right)i_{L_2} - \frac{1}{r_{C_2} + R}v_{C_2}. \tag{3.98}$$

In TIMF model, state variable is modeled by a vector of its QFS coefficients as shown in Equation 3.4. Knowing the vector of the QFS coefficients, one can easily reconstruct the state variable using Equation 3.1. Recall the time derivative of a state variable x can be represented by Equation 3.3, therefore the left hand sides of Equation 3.95-3.98 becomes the following

43

$$L_1 \frac{di_{L_1}}{dt} = L_1 \mathbf{c} \left(-\mathbf{\Omega} \mathbf{i}_{\mathbf{L_1}} + \frac{d\mathbf{i}_{\mathbf{L_1}}}{dt} \right) \qquad (3.99)$$

$$L_2 \frac{di_{L_2}}{dt} = L_2 \mathbf{c} \left(-\mathbf{\Omega} \mathbf{i}_{\mathbf{L_2}} + \frac{d\mathbf{i}_{\mathbf{L_2}}}{dt} \right) \qquad (3.100)$$

$$C_1 \frac{dv_{C_1}}{dt} = C_1 \mathbf{c} \left(-\mathbf{\Omega} \mathbf{v}_{\mathbf{C_1}} + \frac{d\mathbf{v}_{\mathbf{C_1}}}{dt} \right) \qquad (3.101)$$

$$C_2 \frac{dv_{C_2}}{dt} = C_2 \mathbf{c} \left(-\mathbf{\Omega} \mathbf{v}_{\mathbf{C_2}} + \frac{d\mathbf{v}_{\mathbf{C_2}}}{dt} \right), \qquad (3.102)$$

where $\mathbf{i}_{\mathbf{L_1}}$, $\mathbf{i}_{\mathbf{L_2}}$, $\mathbf{v}_{\mathbf{C_1}}$ and $\mathbf{v}_{\mathbf{C_2}}$ are vectors of QFS coefficients of state variables i_{L_1}, i_{L_2}, v_{C_1}, and v_{C_2}, the vector $\mathbf{c}$ has been previously defined in Equation 3.56, and $\mathbf{\Omega}$ is defined in Equation 3.6 . For $N = 2$,

$$\mathbf{i}_{\mathbf{L_1}}^{\mathsf{T}} = \left[i_{L_1\_0} \quad i_{L_1\_\alpha_1} \quad i_{L_1\_\beta_1} \quad i_{L_1\_\alpha_2} \quad i_{L_1\_\beta_2} \right] \qquad (3.103)$$

$$\mathbf{i}_{\mathbf{L_2}}^{\mathsf{T}} = \left[i_{L_2\_0} \quad i_{L_2\_\alpha_1} \quad i_{L_2\_\beta_1} \quad i_{L_2\_\alpha_2} \quad i_{L_2\_\beta_2} \right] \qquad (3.104)$$

$$\mathbf{v}_{\mathbf{C_1}}^{\mathsf{T}} = \left[v_{C_1\_0} \quad v_{C_1\_\alpha_1} \quad v_{C_1\_\beta_1} \quad v_{C_1\_\alpha_2} \quad v_{C_1\_\beta_2} \right] \qquad (3.105)$$

$$\mathbf{v}_{\mathbf{C_2}}^{\mathsf{T}} = \left[v_{C_2\_0} \quad v_{C_2\_\alpha_1} \quad v_{C_2\_\beta_1} \quad v_{C_2\_\alpha_2} \quad v_{C_2\_\beta_2} \right], \qquad (3.106)$$

and

$$\mathbf{\Omega} = \begin{bmatrix} 0 & 0 & 0 & 0 & 0 \\ 0 & 0 & -\omega_{sw} & 0 & 0 \\ 0 & \omega_{sw} & 0 & 0 & 0 \\ 0 & 0 & 0 & 0 & -2\omega_{sw} \\ 0 & 0 & 0 & 2\omega_{sw} & 0 \end{bmatrix}. \qquad (3.107)$$

Using Equations 3.11-3.13, one can convert the right hand sides of Equations 3.95-3.98 into vector representation. Hence,

$$L_1 \mathbf{c} \left(-\mathbf{\Omega} \mathbf{i}_{\mathbf{L_1}} + \frac{d\mathbf{i}_{\mathbf{L_1}}}{dt} \right) = \mathbf{cq} \left[-\left(r_{L_1} + r_m \right) \mathbf{c} \mathbf{i}_{\mathbf{L_1}} + r_m \mathbf{c} \mathbf{i}_{\mathbf{L_2}} \right] +$$

44

$$\left(1-\mathbf{cq}\right)\!\left[-\left(r_{L_1}+r_{C_1}+r_d\right)\mathbf{ci_{L_1}}+r_d\mathbf{ci_{L_2}}-\mathbf{cv_{C_1}}\right]+\left[\mathbf{cq}v_g+\left(1-\mathbf{cq}\right)\!\left(v_g-v_d\right)\right] \tag{3.108}$$

$$L_2\mathbf{c}\!\left(-\mathbf{\Omega i_{L_2}}+\frac{d\mathbf{i_{L_2}}}{dt}\right)=$$

$$\mathbf{cq}\!\left[r_m\mathbf{ci_{L_1}}-\left(r_{C_1}+r_{L_2}+r_{C_2}-\frac{r_{C_2}^2}{r_{C_2}+R}+r_m\right)\mathbf{ci_{L_2}}-\mathbf{cv_{C_1}}-\left(1-\frac{r_{C_2}}{r_{C_2}+R}\right)\mathbf{cv_{C_2}}\right]+$$

$$\left(1-\mathbf{cq}\right)\!\left[r_d\mathbf{ci_{L_1}}-\left(r_{L_2}+r_{C_2}-\frac{r_{C_2}^2}{r_{C_2}+R}+r_d\right)\mathbf{ci_{L_2}}-\left(1-\frac{r_{C_2}}{r_{C_2}+R}\right)\mathbf{cv_{C_2}}\right]+\left(1-\mathbf{cq}\right)v_d \tag{3.109}$$

$$C_1\mathbf{c}\!\left(-\mathbf{\Omega v_{C_1}}+\frac{d\mathbf{v_{C_1}}}{dt}\right)=\left(\mathbf{cq}\right)\!\left(\mathbf{ci_{L_2}}\right)+\left(1-\mathbf{cq}\right)\mathbf{ci_{L_1}} \tag{3.110}$$

$$C_2\mathbf{c}\!\left(-\mathbf{\Omega v_{C_2}}+\frac{d\mathbf{v_{C_2}}}{dt}\right)=\left(1-\frac{r_{C_2}}{r_{C_2}+R}\right)\mathbf{ci_{L_2}}-\frac{1}{r_{C_2}+R}\mathbf{cv_{C_2}}. \tag{3.111}$$

Rearranging Equations 3.108-3.111 yields

$$L_1\mathbf{c}\,\frac{d\mathbf{i_{L_1}}}{dt}=-\left(r_{L_1}+r_m\right)\!\left(\mathbf{cq}\right)\!\left(\mathbf{ci_{L_1}}\right)+r_m\left(\mathbf{cq}\right)\!\left(\mathbf{ci_{L_2}}\right)-$$

$$\left(r_{L_1}+r_{C_1}+r_d\right)\mathbf{ci_{L_1}}+r_d\mathbf{ci_{L_2}}-\mathbf{cv_{C_1}}-$$

$$\left(r_{L_1}+r_{C_1}+r_d\right)\!\left(-\mathbf{cq}\right)\!\left(\mathbf{ci_{L_1}}\right)+r_d\left(-\mathbf{cq}\right)\!\left(\mathbf{ci_{L_2}}\right)-\left(-\mathbf{cq}\right)\!\left(\mathbf{cv_{C_1}}\right)+$$

$$\mathbf{cq}v_g+\left(v_g-v_d\right)+\left(-\mathbf{cq}\right)\!\left(v_g-v_d\right)+\mathbf{c}L_1\mathbf{\Omega i_{L_1}} \tag{3.112}$$

$$L_2\mathbf{c}\,\frac{d\mathbf{i_{L_2}}}{dt}=r_m\left(\mathbf{cq}\right)\!\left(\mathbf{ci_{L_1}}\right)-\left(r_{C_1}+r_{L_2}+r_{C_2}-\frac{r_{C_2}^2}{r_{C_2}+R}+r_m\right)\!\left(\mathbf{cq}\right)\!\left(\mathbf{ci_{L_2}}\right)-$$

$$\left(\mathbf{cq}\right)\!\left(\mathbf{cv_{C_1}}\right)-\left(1-\frac{r_{C_2}}{r_{C_2}+R}\right)\!\left(\mathbf{cq}\right)\!\left(\mathbf{cv_{C_2}}\right)+$$

$$r_d\mathbf{ci_{L_1}}-\left(r_{L_2}+r_{C_2}-\frac{r_{C_2}^2}{r_{C_2}+R}+r_d\right)\mathbf{ci_{L_2}}-\left(1-\frac{r_{C_2}}{r_{C_2}+R}\right)\mathbf{cv_{C_2}}+$$

$$r_d(-\mathbf{cq})(\mathbf{ci_{L_1}}) - \left(r_{L_2} + r_{C_2} - \frac{r_{C_2}^2}{r_{C_2} + R} + r_d\right)(-\mathbf{cq})(\mathbf{ci_{L_2}}) -$$

$$\left(1 - \frac{r_{C_2}}{r_{C_2} + R}\right)(-\mathbf{cq})(\mathbf{cv_{C_2}}) + v_d + (-\mathbf{cq})v_d + \mathbf{c}L_2\Omega\mathbf{i_{L_2}} \tag{3.113}$$

$$C_1\mathbf{c}\frac{d\mathbf{v_{C_1}}}{dt} = (\mathbf{cq})(\mathbf{ci_{L_2}}) + \mathbf{ci_{L_1}} + (-\mathbf{cq})(\mathbf{ci_{L_1}}) + \mathbf{c}C_1\Omega\mathbf{v_{C_1}} \tag{3.114}$$

$$C_2\mathbf{c}\frac{d\mathbf{v_{C_2}}}{dt} = \left(1 - \frac{r_{C_2}}{r_{C_2} + R}\right)\mathbf{ci_{L_2}} - \frac{1}{r_{C_2} + R}\mathbf{cv_{C_2}} + \mathbf{c}C_2\Omega\mathbf{v_{C_2}} \tag{3.115}$$

In Equations 3.112-3.115, the products of the switching function q and variable state variables x have been observed. After substituting Equation 3.89 into Equations 3.112-3.115, the equations become

$$L_1\mathbf{c}\frac{d\mathbf{i_{L_1}}}{dt} = -(r_{L1} + r_m)\mathbf{c}(\mathbf{Qi_{L_1}}) + r_m\mathbf{c}(\mathbf{Qi_{L_2}}) -$$

$$(r_{L_1} + r_{C_1} + r_d)\mathbf{ci_{L_1}} + r_d\mathbf{ci_{L_2}} - \mathbf{cv_{C_1}} -$$

$$(r_{L_1} + r_{C_1} + r_d)\mathbf{c}(-\mathbf{Qi_{L_1}}) + r_d\mathbf{c}(-\mathbf{Qi_{L_2}}) - \mathbf{c}(-\mathbf{Qv_{C_1}}) +$$

$$\mathbf{cq}v_g + (v_g - v_d) + (-\mathbf{cq})(v_g - v_d) + \mathbf{c}L_1\Omega\mathbf{i_{L_1}} \tag{3.116}$$

$$L_2\mathbf{c}\frac{d\mathbf{i_{L_2}}}{dt} = r_m\mathbf{c}(\mathbf{Qi_{L_1}}) - \left(r_{C_1} + r_{L_2} + r_{C_2} - \frac{r_{C_2}^2}{r_{C_2} + R} + r_m\right)\mathbf{c}(\mathbf{Qi_{L_2}}) -$$

$$\mathbf{c}(\mathbf{Qv_{C_1}}) - \left(1 - \frac{r_{C_2}}{r_{C_2} + R}\right)\mathbf{c}(\mathbf{Qv_{C_2}}) +$$

$$r_d\mathbf{ci_{L_1}} - \left(r_{L_2} + r_{C_2} - \frac{r_{C_2}^2}{r_{C_2} + R} + r_d\right)\mathbf{ci_{L_2}} - \left(1 - \frac{r_{C_2}}{r_{C_2} + R}\right)\mathbf{cv_{C_2}} +$$

46

$$r_d\mathbf{c}\left(-\mathbf{Qi_{L_1}}\right)-\left(r_{L_2}+r_{C_2}-\frac{r_{C_2}^2}{r_{C_2}+R}+r_d\right)\mathbf{c}\left(-\mathbf{Qi_{L_2}}\right)-$$

$$\left(1-\frac{r_{C_2}}{r_{C_2}+R}\right)\mathbf{c}\left(-\mathbf{Qv_{C_2}}\right)+v_d+\left(-\mathbf{cq}\right)v_d+\mathbf{c}L_2\Omega\mathbf{i_{L_2}} \qquad (3.117)$$

$$C_1\mathbf{c}\frac{d\mathbf{v_{C_1}}}{dt}=\mathbf{c}\left(\mathbf{Qi_{L_2}}\right)+\mathbf{ci_{L_1}}+\mathbf{c}\left(-\mathbf{Qi_{L_1}}\right)+\mathbf{c}C_1\Omega\mathbf{v_{C_1}} \qquad (3.118)$$

$$C_2\mathbf{c}\frac{d\mathbf{v_{C_2}}}{dt}=\left(1-\frac{r_{C_2}}{r_{C_2}+R}\right)\mathbf{ci_{L_2}}-\frac{1}{r_{C_2}+R}\mathbf{cv_{C_2}}+\mathbf{c}C_2\Omega\mathbf{v_{C_2}} \qquad (3.119)$$

In Equations 3.116-3.119, with the exceptions of constants, all of the terms are multiplied with the vector $\mathbf{c}$ from the left. In order to simplify the derivation for TIMF model, one can also define a constant z as a multiplication of two vectors as

$$z=\mathbf{cz}, \qquad (3.120)$$

where the vector $\mathbf{c}$ as defined in Equation 3.56 and

$$\mathbf{z^T}=\begin{bmatrix}z & 0 & 0 & 0 & 0\end{bmatrix}. \qquad (3.121)$$

Finally,

$$L_1\mathbf{c}\frac{d\mathbf{i_{L_1}}}{dt}=-\left(r_{L1}+r_m\right)\mathbf{c}\left(\mathbf{Qi_{L_1}}\right)+r_m\mathbf{c}\left(\mathbf{Qi_{L_2}}\right)-$$

$$\left(r_{L_1}+r_{C_1}+r_d\right)\mathbf{ci_{L_1}}+r_d\mathbf{ci_{L_2}}-\mathbf{cv_{C_1}}-$$

$$\left(r_{L_1}+r_{C_1}+r_d\right)\mathbf{c}\left(-\mathbf{Qi_{L_1}}\right)+r_d\mathbf{c}\left(-\mathbf{Qi_{L_2}}\right)-\mathbf{c}\left(-\mathbf{Qv_{C_1}}\right)+$$

$$\mathbf{cq}v_g+\mathbf{c}\left(\mathbf{v_g}-\mathbf{v_d}\right)+\left(-\mathbf{cq}\right)\left(v_g-v_d\right)+\mathbf{c}L_1\Omega\mathbf{i_{L_1}} \qquad (3.122)$$

$$L_2\mathbf{c}\frac{d\mathbf{i_{L_2}}}{dt}=r_m\mathbf{c}\left(\mathbf{Qi_{L_1}}\right)-\left(r_{C_1}+r_{L_2}+r_{C_2}-\frac{r_{C_2}^2}{r_{C_2}+R}+r_m\right)\mathbf{c}\left(\mathbf{Qi_{L_2}}\right)-$$

$$\mathbf{c}\left(\mathbf{Q}\mathbf{v}_{\mathbf{C_1}}\right)-\left(1-\frac{r_{C_2}}{r_{C_2}+R}\right)\mathbf{c}\left(\mathbf{Q}\mathbf{v}_{\mathbf{C_2}}\right)+$$

$$r_d\mathbf{c}\mathbf{i}_{\mathbf{L_1}}-\left(r_{L_2}+r_{C_2}-\frac{r_{C_2}^2}{r_{C_2}+R}+r_d\right)\mathbf{c}\mathbf{i}_{\mathbf{L_2}}-\left(1-\frac{r_{C_2}}{r_{c2}+R}\right)\mathbf{c}\mathbf{v}_{\mathbf{C_2}}+$$

$$r_d\mathbf{c}\left(-\mathbf{Q}\mathbf{i}_{\mathbf{L_1}}\right)-\left(r_{L_2}+r_{C_2}-\frac{r_{C_2}^2}{r_{C_2}+R}+r_d\right)\mathbf{c}\left(-\mathbf{Q}\mathbf{i}_{\mathbf{L_2}}\right)-$$

$$\left(1-\frac{r_{C_2}}{r_{C_2}+R}\right)\mathbf{c}\left(-\mathbf{Q}\mathbf{v}_{\mathbf{C_2}}\right)+\mathbf{c}\mathbf{v}_{\mathbf{d}}+\left(-\mathbf{c}\mathbf{q}\right)v_d+\mathbf{c}L_2\mathbf{\Omega}\mathbf{i}_{\mathbf{L_2}} \tag{3.123}$$

$$C_1\mathbf{c}\frac{d\mathbf{v}_{\mathbf{C_1}}}{dt}=\mathbf{c}\left(\mathbf{Q}\mathbf{i}_{\mathbf{L_2}}\right)+\mathbf{c}\mathbf{i}_{\mathbf{L_1}}+\mathbf{c}\left(-\mathbf{Q}\mathbf{i}_{\mathbf{L_1}}\right)+\mathbf{c}C_1\mathbf{\Omega}\mathbf{v}_{\mathbf{C_1}} \tag{3.124}$$

$$C_2\mathbf{c}\frac{d\mathbf{v}_{\mathbf{C_2}}}{dt}=\left(1-\frac{r_{C_2}}{r_{C_2}+R}\right)\mathbf{c}\mathbf{i}_{\mathbf{L_2}}-\frac{1}{r_{C_2}+R}\mathbf{c}\mathbf{v}_{\mathbf{C_2}}+\mathbf{c}C_2\mathbf{\Omega}\mathbf{v}_{\mathbf{C_2}}. \tag{3.125}$$

Now all the terms on both sides of Equations 3.122-3.125 are multiplied by vector **c** from the left, one can simply factor out the vector **c** from both sides, and equating the coefficients. Thus, the TIMF model of the Cuk converter has the form of

$$L_1\frac{d\mathbf{i}_{\mathbf{L_1}}}{dt}=-\left(r_{L1}+r_m\right)\left(\mathbf{Q}\mathbf{i}_{\mathbf{L_1}}\right)+r_m\left(\mathbf{Q}\mathbf{i}_{\mathbf{L_2}}\right)-$$

$$\left(r_{L_1}+r_{C_1}+r_d\right)\mathbf{i}_{\mathbf{L_1}}+r_d\mathbf{i}_{\mathbf{L_2}}-\mathbf{v}_{\mathbf{C_1}}-$$

$$\left(r_{L_1}+r_{C_1}+r_d\right)\left(-\mathbf{Q}\mathbf{i}_{\mathbf{L_1}}\right)+r_d\left(-\mathbf{Q}\mathbf{i}_{\mathbf{L_2}}\right)-\left(-\mathbf{Q}\mathbf{v}_{\mathbf{C_1}}\right)+$$

$$\mathbf{q}v_g+\left(\mathbf{v_g}-\mathbf{v_d}\right)+\left(-\mathbf{q}\right)\left(v_g-v_d\right)+L_1\mathbf{\Omega}\mathbf{i}_{\mathbf{L_1}} \tag{3.126}$$

$$L_2\frac{d\mathbf{i}_{\mathbf{L_2}}}{dt}=r_m\left(\mathbf{Q}\mathbf{i}_{\mathbf{L_1}}\right)-\left(r_{C_1}+r_{L_2}+r_{C_2}-\frac{r_{C_2}^2}{r_{C_2}+R}+r_m\right)\left(\mathbf{Q}\mathbf{i}_{\mathbf{L_2}}\right)-$$

48

$$\left(\mathbf{Q}\mathbf{v_{C_1}}\right) - \left(1 - \frac{r_{C_2}}{r_{C_2} + R}\right)\left(\mathbf{Q}\mathbf{v_{C_2}}\right) +$$

$$r_d \mathbf{i_{L_1}} - \left(r_{L_2} + r_{C_2} - \frac{r_{C_2}^2}{r_{C_2} + R} + r_d\right)\mathbf{i_{L_2}} - \left(1 - \frac{r_{C_2}}{r_{C_2} + R}\right)\mathbf{v_{C_2}} +$$

$$r_d\left(-\mathbf{Q}\mathbf{i_{L_1}}\right) - \left(r_{L_2} + r_{C_2} - \frac{r_{C_2}^2}{r_{C_2} + R} + r_d\right)\left(-\mathbf{Q}\mathbf{i_{L_2}}\right) -$$

$$\left(1 - \frac{r_{C_2}}{r_{C_2} + R}\right)\left(-\mathbf{Q}\mathbf{v_{C_2}}\right) + \mathbf{v_d} + \left(-\mathbf{q}\right)v_d + L_2\mathbf{\Omega}\mathbf{i_{L_2}} \tag{3.127}$$

$$C_1 \frac{d\mathbf{v_{C_1}}}{dt} = \left(\mathbf{Q}\mathbf{i_{L_2}}\right) + \mathbf{i_{L_1}} + \left(-\mathbf{Q}\mathbf{i_{L_1}}\right) + C_1\mathbf{\Omega}\mathbf{v_{C_1}} \tag{3.128}$$

$$C_2 \frac{d\mathbf{v_{C_2}}}{dt} = \left(1 - \frac{r_{C_2}}{r_{C_2} + R}\right)\mathbf{i_{L_2}} - \frac{1}{r_{C_2} + R}\mathbf{v_{C_2}} + C_2\mathbf{\Omega}\mathbf{v_{C_2}} . \tag{3.129}$$

In the original state space model (Equations 3.91-3.94) has four unknown state variables (i_{L_1}, i_{L_2}, v_{C_1}, and v_{C_2}), and four equations. In TIMF model, there are 20 unknown QFS coefficients and 20 equations. These extra coefficients and equations enable TIMF to perform ripple estimation, which the SSA is not able to achieve. Further simplification of Equations 3.126-3.129 yields

$$L_1 \frac{d\mathbf{i_{L_1}}}{dt} = \mathbf{Q}\left[-\left(r_{L_1} + r_m\right)\mathbf{i_{L_1}} + r_m\mathbf{i_{L_2}}\right] +$$

$$\left(\mathbf{I_5} - \mathbf{Q}\right)\left[-\left(r_{L_1} + r_{C_1} + r_d\right)\mathbf{i_{L_1}} + r_d\mathbf{i_{L_2}} - \mathbf{v_{C_1}}\right] +$$

$$\left(\mathbf{v_g} - \mathbf{v_d}\right) + \mathbf{q}v_d + L_1\mathbf{\Omega}\mathbf{i_{L_1}} \tag{3.130}$$

$$L_2 \frac{d\mathbf{i_{L_2}}}{dt} =$$

$$\mathbf{Q}\left[r_m\mathbf{i_{L_1}} - \left(r_{C_1} + r_{L_2} + r_{C_2} - \frac{r_{C_2}^2}{r_{C_2} + R} + r_m\right)\mathbf{i_{L2}} - \mathbf{v_{C_1}} - \left(1 - \frac{r_{C_2}}{r_{C_2} + R}\right)\mathbf{v_{C_2}}\right] +$$

$$\left(\mathbf{I_5} - \mathbf{Q}\right)\left[r_d\mathbf{i_{L_1}} - \left(r_{L_2} + r_{C_2} - \frac{r_{C_2}^2}{r_{C_2} + R} + r_d\right)\mathbf{i_{L_2}} - \left(1 - \frac{r_{C_2}}{r_{C_2} + R}\right)\mathbf{v_{C_2}}\right] +$$

$$\mathbf{v_d} - \mathbf{q}v_d + L_2\mathbf{\Omega i_{L_2}} \tag{3.131}$$

$$C_1\frac{d\mathbf{v_{C_1}}}{dt} = \mathbf{Qi_{L_2}} + \left(\mathbf{I_5} - \mathbf{Q}\right)\mathbf{i_{L_1}} + C_1\mathbf{\Omega v_{C_1}} \tag{3.132}$$

$$C_2\frac{d\mathbf{v_{C_2}}}{dt} = \left(1 - \frac{r_{C_2}}{r_{C_2} + R}\right)\mathbf{i_{L_2}} - \frac{1}{r_{C_2} + R}\mathbf{v_{C_2}} + C_2\mathbf{\Omega v_{C_2}} , \tag{3.133}$$

where $\mathbf{I_5}$ is an 5-by-5 identity matrix. Adapting TIMF in the matrix form becomes

$$\frac{d}{dt}\begin{bmatrix} \mathbf{i_{L_1}} \\ \mathbf{i_{L_2}} \\ \mathbf{v_{C_1}} \\ \mathbf{v_{C_2}} \end{bmatrix} = \begin{bmatrix} \mathbf{A_{11}} & \mathbf{A_{12}} & \mathbf{A_{13}} & \mathbf{A_{14}} \\ \mathbf{A_{21}} & \mathbf{A_{22}} & \mathbf{A_{23}} & \mathbf{A_{24}} \\ \mathbf{A_{31}} & \mathbf{A_{32}} & \mathbf{A_{33}} & \mathbf{A_{34}} \\ \mathbf{A_{41}} & \mathbf{A_{42}} & \mathbf{A_{43}} & \mathbf{A_{44}} \end{bmatrix}\begin{bmatrix} \mathbf{i_{L_1}} \\ \mathbf{i_{L_2}} \\ \mathbf{v_{C_1}} \\ \mathbf{v_{C_2}} \end{bmatrix} + \begin{bmatrix} \left(\mathbf{v_g} - \mathbf{v_d}\right) + \mathbf{q}v_d \\ \mathbf{v_d} - \mathbf{q}v_d \\ \mathbf{0} \\ \mathbf{0} \end{bmatrix}. \tag{3.134}$$

where $\mathbf{0} = \begin{bmatrix} 0 & 0 & 0 & 0 & 0 \end{bmatrix}^T$ and

$$\mathbf{A_{11}} = -\frac{1}{L_1}\mathbf{Q}\left(r_{L_1} + r_m\right) - \frac{1}{L_1}\left(\mathbf{I_5} - \mathbf{Q}\right)\left(r_{L_1} + r_{C_1} + r_d\right) + \mathbf{\Omega} \tag{3.135}$$

$$\mathbf{A_{12}} = \frac{1}{L_1}\mathbf{Q}r_m + \frac{1}{L_1}\left(\mathbf{I_5} - \mathbf{Q}\right)r_d \tag{3.136}$$

$$\mathbf{A_{13}} = -\frac{1}{L_1}\left(\mathbf{I_5} - \mathbf{Q}\right) \tag{3.137}$$

$$\mathbf{A_{14}} = \mathbf{I_5} \cdot 0 \tag{3.138}$$

$$\mathbf{A_{21}} = \mathbf{Q}r_m + \left(\mathbf{I_5} - \mathbf{Q}\right)r_d \tag{3.139}$$

$$\mathbf{A_{22}} = -\frac{1}{L_2}\mathbf{Q}\left(r_{C_1} + r_{L_2} + r_{C_2} - \frac{r_{C_2}^2}{r_{C2} + R} + r_m\right)$$

$$\frac{1}{L_2}(\mathbf{I_5} - \mathbf{Q})\left(r_{L_2} + r_{C_2} - \frac{r_{C_2}^2}{r_{C_2} + R} + r_d\right) + \mathbf{\Omega} \tag{3.140}$$

$$\mathbf{A_{23}} = -\frac{1}{L_2}\mathbf{Q} \tag{3.141}$$

$$\mathbf{A_{24}} = -\frac{1}{L_2}\left(1 - \frac{r_{C_2}}{r_{C_2} + R}\right)\mathbf{I_5} \tag{3.142}$$

$$\mathbf{A_{31}} = \frac{1}{C_1}(\mathbf{I_5} - \mathbf{Q}) \tag{3.143}$$

$$\mathbf{A_{32}} = \frac{1}{C_1}\mathbf{Q} \tag{3.144}$$

$$\mathbf{A_{33}} = \mathbf{\Omega} \tag{3.145}$$

$$\mathbf{A_{34}} = \mathbf{I_5} \cdot 0 \tag{3.146}$$

$$\mathbf{A_{41}} = \mathbf{I_5} \cdot 0 \tag{3.147}$$

$$\mathbf{A_{42}} = \frac{1}{C_2}\left(1 - \frac{r_{C_2}}{r_{C_2} + R}\right)\mathbf{I_5} \tag{3.148}$$

$$\mathbf{A_{43}} = \mathbf{I_5} \cdot 0 \tag{3.149}$$

$$\mathbf{A_{44}} = -\frac{1}{C_2}\left(\frac{1}{r_{C_2} + R}\right)\mathbf{I_5} + \mathbf{\Omega} \, . \tag{3.150}$$

In order to simplify the process of converting from the state space model to TIMF, one can develop a set of rules from comparing the original state space model (Equations 3.91-3.94) to the TIMF model.

Table 3.1 Rules for Converting State Space Model to TIMF Model

Rules	Descriptions	Examples
$x \rightarrow \mathbf{x}$	The state variable is replaced by its QFS coefficient vector	$i_{L_2} \rightarrow \mathbf{i_{L_2}}$
$\dfrac{dx}{dt} \rightarrow -\mathbf{\Omega x} + \dfrac{d\mathbf{x}}{dt}$	The time derivative of the state variable is replaced by the time derivative of its QFS coefficient vector minus the an extra term $\mathbf{\Omega x}$	$L_1 \dfrac{di_{L_1}}{dt} \rightarrow L_1\left(-\mathbf{\Omega i_{L_1}} + \dfrac{d\mathbf{i_{L_1}}}{dt}\right)$
$q \rightarrow \mathbf{Q}$	The switching function is replaced by a square matrix of the size $2N+1$ as presented in Equation 3.85	$(1-q) \rightarrow (\mathbf{I_5} - \mathbf{Q})$
$z \rightarrow \mathbf{z}$	Constants terms without state variables such as input voltage, input current and forward bias voltage of the diode are replaced by its vector form as presented in Equation 3.121	$v_d \rightarrow \mathbf{v}_d = \begin{bmatrix} v_d \\ 0 \\ 0 \\ 0 \\ 0 \end{bmatrix}$

For the purpose of this comparison, reorganize Equations 3.130-3.133 to the following form

$$L_1\left(-\mathbf{\Omega i_{L_1}} + \frac{d\mathbf{i_{L_1}}}{dt}\right) = \mathbf{Q}\left[\mathbf{v_g} - \left(r_{L_1} + r_m\right)\mathbf{i_{L_1}} + r_m\mathbf{i_{L_2}}\right] +$$

$$(\mathbf{I_5} - \mathbf{Q})\left[-\left(r_{L_1} + r_{C_1} + r_d\right)\mathbf{i_{L_1}} + r_d\mathbf{i_{L_2}} - \mathbf{v_{C_1}} + \mathbf{v_g} - \mathbf{v_d}\right]$$

(3.151)

$$L_2\left(-\mathbf{\Omega i_{L_2}} + \frac{d\mathbf{i_{L_2}}}{dt}\right) =$$

$$\mathbf{Q}\left[r_m\mathbf{i_{L_1}} - \left(r_{C_1} + r_{L_2} + r_{C_2} - \frac{r_{C_2}^2}{r_{C_2} + R} + r_m\right)\mathbf{i_{L_2}} - \mathbf{v_{C_1}} - \left(1 - \frac{r_{C_2}}{r_{C_2} + R}\right)\mathbf{v_{C_2}}\right] +$$

$$(\mathbf{I_5} - \mathbf{Q})\left[r_d\mathbf{i_{L_1}} - \left(r_{L_2} + r_{C_2} - \frac{r_{C_2}^2}{r_{C_2} + R} + r_d\right)\mathbf{i_{L_2}} - \left(1 - \frac{r_{C_2}}{r_{C_2} + R}\right)\mathbf{v_{C_2}} + \mathbf{v_d}\right]$$

(3.152)

$$C_1\left(-\boldsymbol{\Omega}\mathbf{v_{C_1}} + \frac{d\mathbf{v_{C_1}}}{dt}\right) = \mathbf{Q}\mathbf{i_{L_2}} + \left(\mathbf{I_5} - \mathbf{Q}\right)\mathbf{i_{L_1}}$$ (3.153)

$$C_2\left(-\boldsymbol{\Omega}\mathbf{v_{C_2}} + \frac{d\mathbf{v_{C_2}}}{dt}\right) = \left(1 - \frac{r_{C_2}}{r_{C_2} + R}\right)\mathbf{i_{L_2}} - \frac{1}{r_{C_2} + R}\mathbf{v_{C_2}} .$$ (3.154)

As a result of the comparison, Table 3.1 shows a set of rules from converting from state space model to TIMF model.

3.2.2 Proportional-Intergral Control Scheme

This sub-section focuses on the modeling of proportional-integral (PI) controller for TIMF model in the voltage controlled mode (VCM). Similar modeling of PI controller has already been discussed in [71] and [78]. In VCM, the output voltage v_{out} tracks a reference voltage v_{ref} by feeding back the difference of them into the PI compensator. The PI compensator produces the duty cycle command d that reduces this difference, thus

$$d = k_p(v_{out} - v_{ref}) + k_i \int (v_{out} - v_{ref})dt ,$$ (3.155)

where k_p and k_i are the proportional gain and the integral gain, respectively. Since both the duty cycle command d and the output voltage v_{out} can be represented by QFS, therefore Equation 3.155 becomes

$$d_0 + \sum_{n=1}^{N} d_{\alpha_n} \cos(n\omega_{sw}t) + d_{\beta_n} \sin(n\omega_{sw}t) =$$

$$k_p\left(v_{out\_0} + \sum_{n=1}^{N} v_{out\_\alpha_n} \cos(n\omega_{sw}t) + v_{out\_\beta_n} \sin(n\omega_{sw}t) - v_{ref}\right) +$$

$$k_i \int \left(v_{out\_0} + \sum_{n=1}^{N} v_{out\_\alpha_n} \cos(n\omega_{sw}t) + v_{out\_\beta_n} \sin(n\omega_{sw}t) - v_{ref}\right) dt ,$$ (3.156)

where v_{ref} is a DC voltage. Reorganizing Equation 3.156 yields

$$d_0 + \sum_{n=1}^{N} d_{\alpha_n} \cos(n\omega_{sw}t) + d_{\beta_n} \sin(n\omega_{sw}t) =$$

$$k_p \left(v_{out\_0} - v_{ref} + \sum_{n=1}^{N} v_{out\_\alpha_n} \cos(n\omega_{sw}t) + v_{out\_\beta_n} \sin(n\omega_{sw}t) \right) +$$

$$k_i \int (v_{out\_0} - v_{ref})dt + k_i \int \left(\sum_{n=1}^{N} v_{out\_\alpha_n} \cos(n\omega_{sw}t) + v_{out\_\beta_n} \sin(n\omega_{sw}t) \right) dt . \qquad (3.157)$$

The integral of sine and cosine terms on the right hand side can be evaluated by integration by parts as shown in Equation 3.158.

$$k_i \int \left(\sum_{n=1}^{N} v_{out\_\alpha_n} \cos(n\omega_{sw}t) + v_{out\_\beta_n} \sin(n\omega_{sw}t) \right) dt =$$

$$k_i \left(\sum_{n=1}^{N} \frac{v_{out\_\alpha_n}}{n\omega_{sw}} \sin(n\omega_{sw}t) - \frac{v_{out\_\beta_n}}{n\omega_{sw}} \cos(n\omega_{sw}t) \right) -$$

$$k_i \int \left(\sum_{n=1}^{N} \frac{dv_{out\_\alpha_n}}{dt} \frac{1}{n\omega_{sw}} \sin(n\omega_{sw}t) - \frac{dv_{out\_\beta_n}}{dt} \frac{1}{n\omega_{sw}} \cos(n\omega_{sw}t) \right) dt . \qquad (3.158)$$

Applying integration by parts again,

$$k_i \int \left(\sum_{n=1}^{N} v_{out\_\alpha_n} \cos(n\omega_{sw}t) + v_{out\_\beta_n} \sin(n\omega_{sw}t) \right) dt =$$

$$k_i \left(\sum_{n=1}^{N} \frac{v_{out\_\alpha_n}}{n\omega_{sw}} \sin(n\omega_{sw}t) - \frac{v_{out\_\beta_n}}{n\omega_{sw}} \cos(n\omega_{sw}t) \right) -$$

$$k_i \int \left(\sum_{n=1}^{N} \frac{dv_{out\_\alpha_n}}{dt} \frac{1}{(n\omega_{sw})^2} \cos(n\omega_{sw}t) + \frac{dv_{out\_\beta_n}}{dt} \frac{1}{(n\omega_{sw})^2} \sin(n\omega_{sw}t) \right) +$$

$$k_i \int \left(\sum_{n=1}^{N} \frac{d^2 v_{out\_\alpha_n}}{dt^2} \frac{1}{(n\omega_{sw})^2} \cos(n\omega_{sw}t) + \frac{d^2 v_{out\_\beta_n}}{dt^2} \frac{1}{(n\omega_{sw})^2} \sin(n\omega_{sw}t) \right) dt \qquad (3.159)$$

In Equation 3.159, for higher harmonics and high switching frequency, $(n\omega_{sw})^2$ will become extremely large. Thus, Equation 3.159 reduces to

$$k_i \int \left(\sum_{n=1}^{N} v_{out\_\alpha_n} \cos(n\omega_{sw}t) + v_{out\_\beta_n} \sin(n\omega_{sw}t) \right) dt =$$

$$k_i \left(\sum_{n=1}^{N} \frac{v_{out\_\alpha_n}}{n\omega_{sw}} \sin(n\omega_{sw}t) - \frac{v_{out\_\beta_n}}{n\omega_{sw}} \cos(n\omega_{sw}t) \right). \tag{3.160}$$

Substituting Equation 3.160 back into Equation 3.157 yields

$$d_0 + \sum_{n=1}^{N} d_{\alpha_n} \cos(n\omega_{sw}t) + d_{\beta_n} \sin(n\omega_{sw}t) =$$

$$k_p \left(v_{out\_0} - v_{ref} + \sum_{n=1}^{N} v_{out\_\alpha_n} \cos(n\omega_{sw}t) + v_{out\_\beta_n} \sin(n\omega_{sw}t) \right) +$$

$$k_i \int \left(v_{out\_0} - v_{ref} \right) dt + k_i \left(\sum_{n=1}^{N} \frac{v_{out\_\alpha_n}}{n\omega_{sw}} \sin(n\omega_{sw}t) - \frac{v_{out\_\beta_n}}{n\omega_{sw}} \cos(n\omega_{sw}t) \right). \tag{3.161}$$

Since there is often a low pass filter in the feedback loop of VCM PWM converters, the duty cycle command signal d can be well approximated by $N = 1$. Thus,

$$d_0 + d_{\alpha_1} \cos(\omega_{sw}t) + d_{\beta_1} \sin(\omega_{sw}t) =$$

$$k_p (v_{out\_0} - v_{ref} + v_{out\_\alpha_1} \cos(\omega_{sw}t) + v_{out\_\beta_1} \sin(\omega_{sw}t)) +$$

$$k_i \int \left(v_{out\_0} - v_{ref} \right) dt + k_i \left(\frac{v_{out\_\alpha_1}}{\omega_{sw}} \sin(\omega_{sw}t) - \frac{v_{out\_\beta_1}}{\omega_{sw}} \cos(\omega_{sw}t) \right). \tag{3.162}$$

Equating the coefficients on both sides of Equation 3.162 yields

$$d_0 = k_p \left(v_{out\_0} - v_{ref} \right) + k_i \int \left(v_{out\_0} - v_{ref} \right) dt \tag{3.163}$$

$$d_{\alpha 1} = k_p v_{out\_\alpha_1} - k_i \frac{v_{out\_\beta_1}}{\omega_{sw}} \tag{3.164}$$

$$d_{\beta 1} = k_p v_{out\_\beta_1} + k_i \frac{v_{out\_\alpha_1}}{\omega_{sw}} \; . \tag{3.165}$$

If the tracking function is

$$d = k_p \left(v_{ref} - v_{out} \right) + k_i \int \left(v_{ref} - v_{out} \right) dt \; , \tag{3.166}$$

then simply inverting the signs on the right side of Equation 3.142-3.145 yields

$$d_0 = k_p \left(v_{ref} - v_{out\_0} \right) + k_i \int \left(v_{ref} - v_{out\_0} \right) dt \tag{3.167}$$

$$d_{\alpha 1} = -k_p v_{out\_\alpha_1} + k_i \frac{v_{out\_\beta_1}}{\omega_{sw}} \tag{3.168}$$

$$d_{\beta 1} = -k_p v_{out\_\beta_1} - k_i \frac{v_{out\_\alpha_1}}{\omega_{sw}} \; . \tag{3.169}$$

3.2.3 Closed-Loop Time Domain Analysis

The schematic of PI controlled Cuk converter, as illustrated in Figure 3.6, has been implemented for both detailed switching model and second order TIMF model in SIMULINK program. In the detailed switching model, the switch has been simulated by a relational operator which outputs either zero or one by comparing the duty cycle command with the carrier signal. Details of SIMULINK block diagrams and codes are attached in Appendix B. The simulated circuit parameters are listed in Table 3.2. One important principle of selecting the parameter values is that the converter must operates in CCM. Depending on the load resistance, one should choose the appropriate inductors for operating the converter in CCM. For simulation configuration parameters, the max step size is set to 1 μs with relative tolerance of 10^{-3}, and the solver is chosen to be ode45 (Dormand-Prince). This setting is the same for all simulations that will be discussed in case study section of Cuk converter. The sawtooth and triangular carrier signals in the detailed switching model are simulated by using modulators from PLECS toolbox. For the transient study, the load resistance undergoes a step change from 15 Ω to 10 Ω at

$t = 0.5\,\text{sec}$. The transient responses of detailed switching model and TIMF model with sawtooth carrier signal are shown in Figure 3.7. TIMF model match well with the detailed switching model in the steady state as well as in the transient. The zero order term of TIMF model is related to the average value of each state variable. For inductor currents i_{L_1} and i_{L_2}, and the capacitor voltage v_{C_1}, the detailed switched model shows slightly larger ripples than TIMF model. This error can be reduced by considering higher order of harmonics. Due to the equivalent series resistance (ESR) in output capacitor, v_{out} contains larger ripples than v_{C_2}.

The detailed switching model of the Cuk converter has also compared with its TIMF model for the case of triangular carrier signal, as shown in Figure 3.8. As clearly shown in Figure 3.8, TIMF model has well estimated the response of the detailed switched model. The only slight difference between using a sawtooth carrier signal and triangular carrier signal is the fact that their phase angles are different.
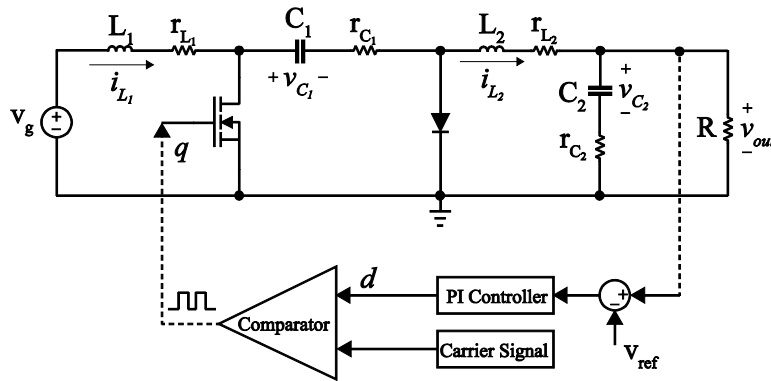
Figure 3.6 The schematic of PI controlled Cuk converter

Table 3.2 Parameter values of Cuk converter used in time-domain analysis

Parameter	v_g	L_1	L_2	C_1	C_2	f_{SW}	v_d	r_d
Value	9 V	363 µH	363 µH	15 µF	56 µF	10kHz	0.4 V	14 mΩ

Parameter	r_m	r_{L_1}	r_{L_2}	r_{C_1}	r_{C_2}	v_{ref}	k_p	k_i
Value	0.7 Ω	64.6mΩ	58.6mΩ	66.4mΩ	478.5mΩ	-15 V	$2.9*10^{-4}$	5

Figure 3.7 Transient response of detailed switching model and TIMF with sawtooth carrier: (a) complete transient response and (b) close-up view
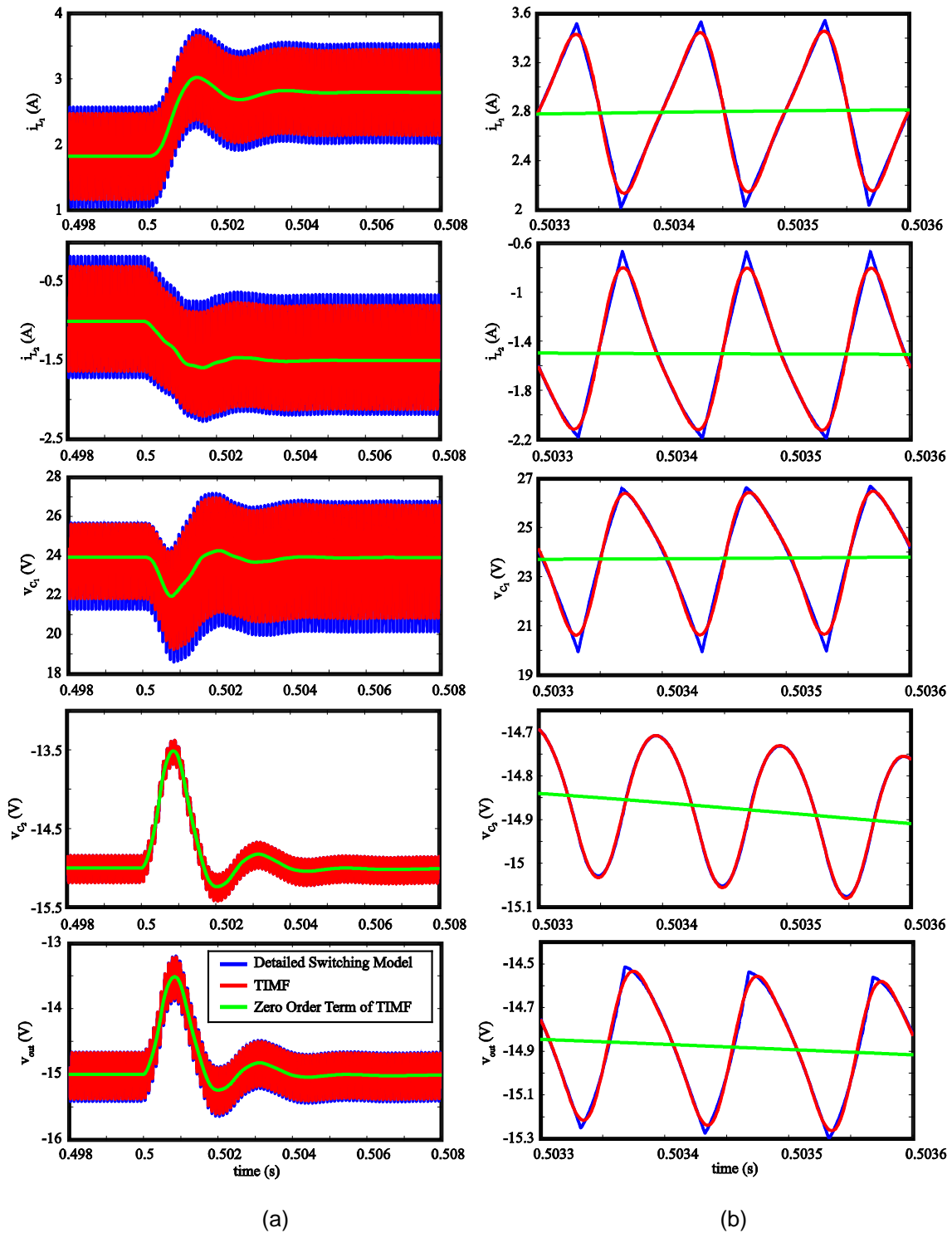
Figure 3.8 Transient response of detailed switching model and TIMF with triangular carrier: (a) complete transient response and (b) close-up view

59

3.2.4 Open-Loop Frequency Domain Analysis

In this sub-section, by using SIMULINK the open-loop Cuk converter shown in Figure 3.4 has been constructed for both TIMF model and detailed switching model. The small-signal input-to-output transfer function $\frac{\hat{v}_{out}}{\hat{v}_g}$ and small-signal control-to-output transfer function $\frac{\hat{v}_{out}}{\hat{d}}$ have been extracted from the simulations with both sawooth and triangular carrier signals for verifying TIMF model against detailed switching model. The parameter values of the Cuk converter are shown in Table 3.3. As shown in Table 3.3, most parameter values are the same as in the time-domain analysis with the exception of the load resistance R, which is set to a constant value of 15Ω. For extracting the transfer functions in the detailed switching model, small signal injection and frequency sweep methods have been implemented. For extracting the transfer functions from TIMF model, the TIMF model is linearized at the same operating points as the detailed switching model by means of MATLAB build-in function linmod. The transfer functions are examined up to 5 kHz, which is one-half of its switching frequency f_{sw}. The results beyond 5 kHz are distorted due to the cross-interference between the switching of the circuit and the injected perturbations [77].
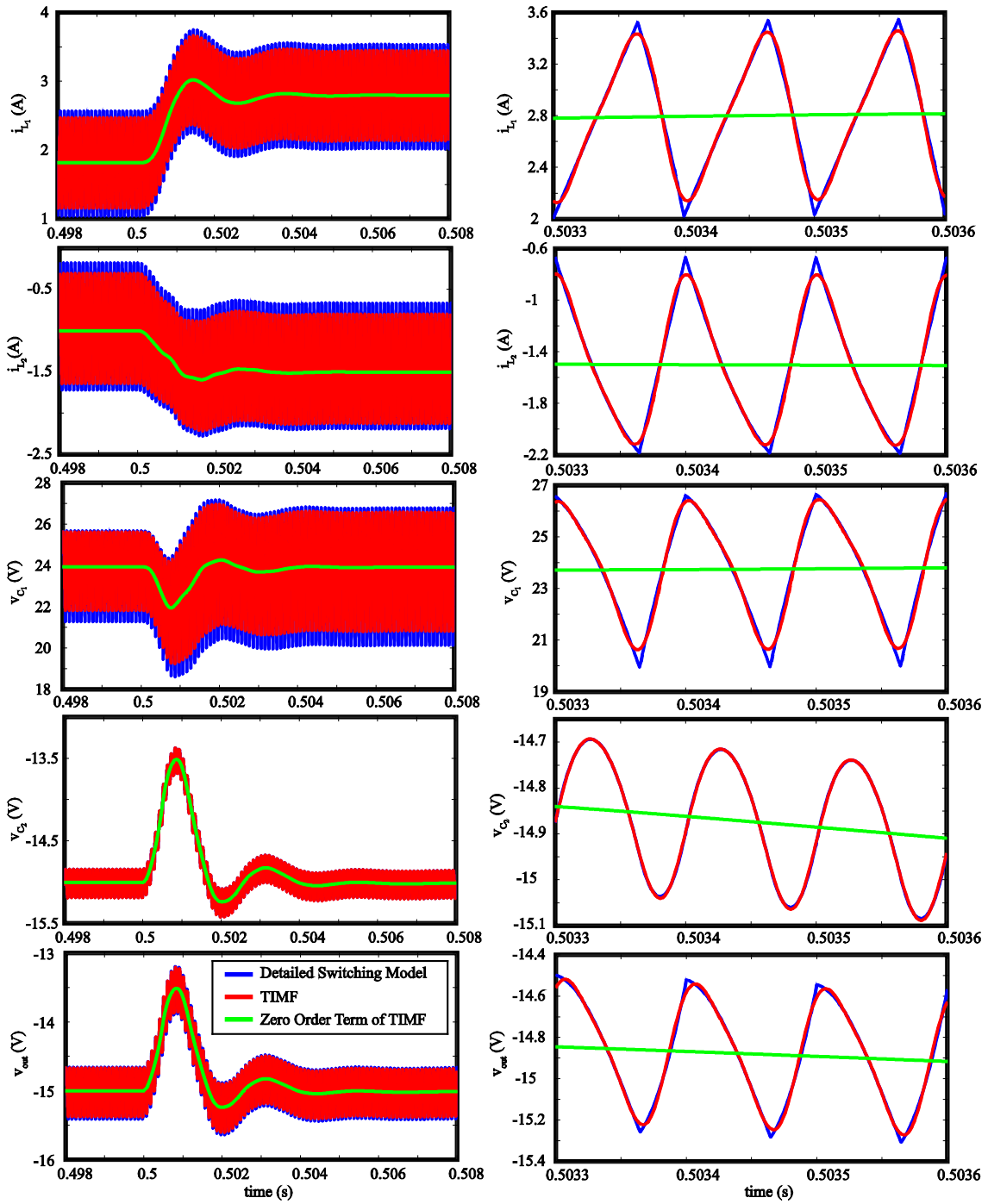
Table 3.3 Parameter values of Cuk converter used in frequency-domain analysis

Parameter	v_g	L_1	L_2	C_1	C_2	f_{sw}	v_d	r_d
Value	9 V	363 µH	363 µH	15 µF	56 µF	10kHz	0.4 V	14 mΩ

Parameter	r_m	r_{L_1}	r_{L_2}	r_{C_1}	r_{C_2}	R	D	
Value	0.7 Ω	64.6mΩ	58.6mΩ	66.4mΩ	478.5mΩ	15 Ω	0.641	

In order to extract the small-signal input-to-output transfer function $\frac{\hat{v}_{out}}{\hat{v}_g}$ in the detailed switching model, a small sine wave of magnitude 0.1V of selected frequency is added to input voltage, as depicted in Figure 3.9. Signals that have been generated in the SIMULINK program can be easily export to the workspace of MATLAB by using a sink block called "To Workspace".

From the workspace, one can simply use a MATLAB function called fft to apply the fast Fourier transform to any signal available in the workspace. As a result, the magnitude and phase of input-to-output transfer function $\dfrac{\hat{v}_{out}}{\hat{v}_g}$ at each selected frequency has been extracted by applying fast Fourier transform. Program codes for extracting the magnitude and phase angle using fft function are attached in Appendix C. The resulting magnitude and phase plots of the input-to-output transfer function with sawtooth carrier are plotted in Figure 3.10. The data points produced by the detailed switching model are considered as a reference for comparison. As shown in Figure 3.10, TIMF model match well with the detailed switching model up to 5 kHz, which is one half of the switching frequency. The phase plot as shown in Figure 3.10(b) begins at 180 degrees since the output voltage of the Cuk converter is inverted. The magnitude and phase plots of the input-to-output transfer function with triangular carrier are plotted in Figure 3.11. As shown in Figure 3.11, the TIMF model correctly predicts the detailed switching model. In cases of sawtooth carrier and triangular carrier, the magnitude plots are identical as shown in Figure 3.10(a) and Figure 3.11(a), and the phase plots are almost identical with only a difference of a few thousandth of a degree as shown in Figure 3.10(b) and 3.11(b).
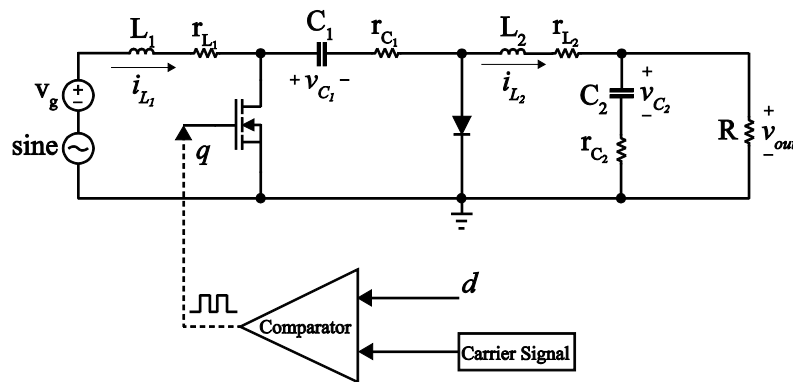

Figure 3.9 Small signal injection for extract input-to-output transfer function of Cuk converter
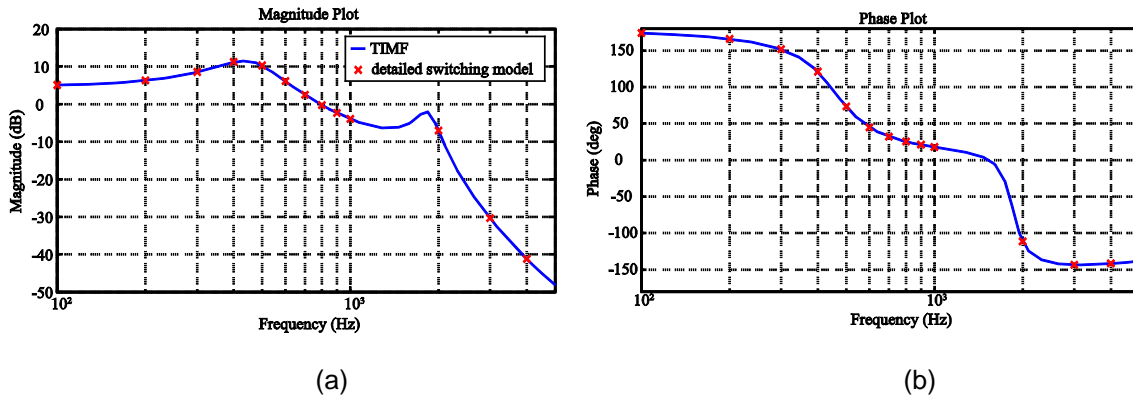
(a)   (b)

Figure 3.10 Input-to-output transfer function of Cuk converter with sawtooth carrier: (a)
magnitude plot (b) phase plot

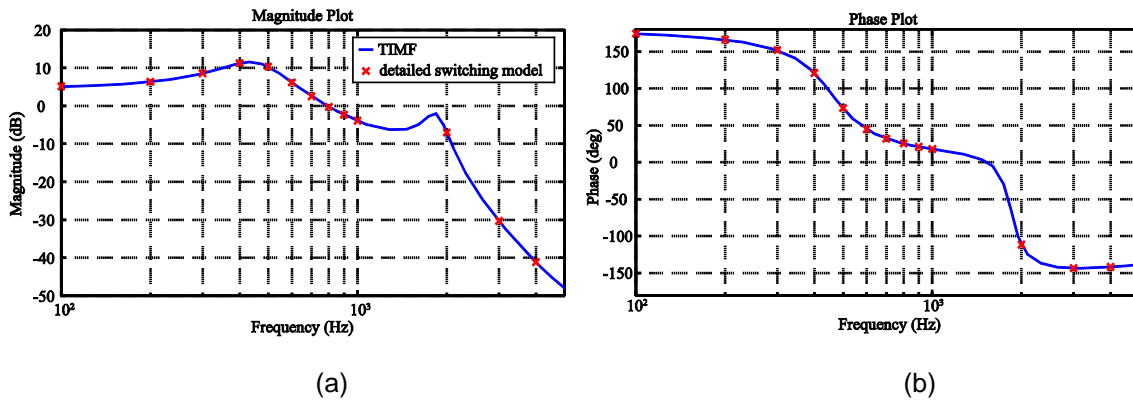(a)   (b)

Figure 3.11 Input-to-output transfer function of Cuk converter with triangular carrier: (a)
magnitude plot (b) phase plot

Similarly, to extract the control-to-output $\dfrac{\hat{v}_{out}}{\hat{d}}$, a small perturbation has been injected

to the duty ratio d, as shown in Figure 3.12. The sine wave has a constant magnitude of 0.1,

but its frequency changes every time a data point is collected. Different from the case of input-

to-output transfer function where the initial condition for every state variable has been set to

zero, the operation points for the input-to-output transfer function of each state variable has

been set to its steady state values as shown in Table 3.4 and Table 3.5. Due to the same

reason discussed before, the transfer functions for both sawtooth and triangular carrier signals

have been examined up to 5 kHz. The resulting control-to-output transfer function for sawtooth

carrier signal are plotted in Figure 3.13 and control-to-output transfer function for triangular

62

carrier are plotted in Figure 3.14. In the magnitude plots, there is no noticable mismatch between the detailed switching model and TIMF model. However, small discrepancy has been observed for the phase plots. One factor contributes to the discrepancy is due to neglect of the higher harmonic terms in the QFS representation of the switching function q, and the duty cycle command d.
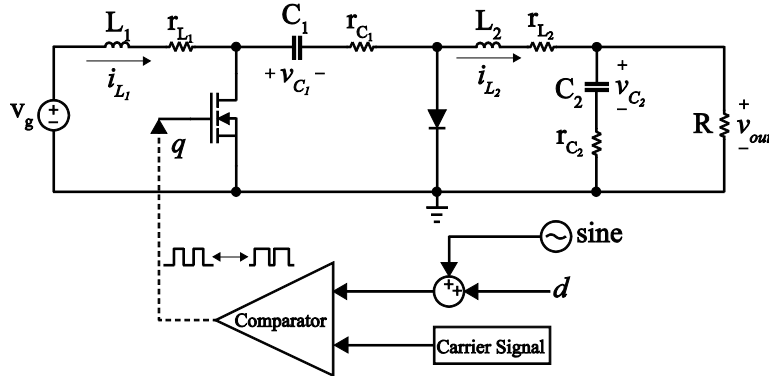

Figure 3.12 Small signal injection for extract control-to-output transfer function of Cuk converter

Table 3.4 Operating points for detailed switching model of control-to-output transfer function of Cuk Converter

Detailed Swiching Model	
i_{L_1}	1.8387 A
i_{L_2}	-0.9975 A
v_{C_1}	23.7943 V
v_{C_2}	-14.963 V

Table 3.5 Operating points for TIMF model of control-to-output transfer function of Cuk Converter

TIMF Model							
$i_{L_1\_0}$	1.8387 A	$i_{L_2\_0}$	-0.9975 A	$v_{C_1\_0}$	23.794 V	$v_{C_2\_0}$	-14.963 V
$i_{L_1\_\alpha_1}$	-0.5863 A	$i_{L_2\_\alpha_1}$	0.6897 A	$v_{C_1\_\alpha_1}$	2.3322 V	$v_{C_2\_\alpha_1}$	-0.0617 V
$i_{L_1\_\beta_1}$	-0.315 A	$i_{L_2\_\beta_1}$	0.1944 A	$v_{C_1\_\beta_1}$	1.6542 V	$v_{C_2\_\beta_1}$	0.2397 V
$i_{L_1\_\alpha_2}$	-0.1262 A	$i_{L_2\_\alpha_2}$	0.1138 A	$v_{C_1\_\alpha_2}$	0.2441 V	$v_{C_2\_\alpha_2}$	0.014 V
$i_{L_1\_\beta_2}$	0.0721 A	$i_{L_2\_\beta_2}$	-0.0797 A	$v_{C_1\_\beta_2}$	-0.5768 V	$v_{C_2\_\beta_2}$	0.0195 V

Magnitude Plot	Phase Plot
(a)	(b)
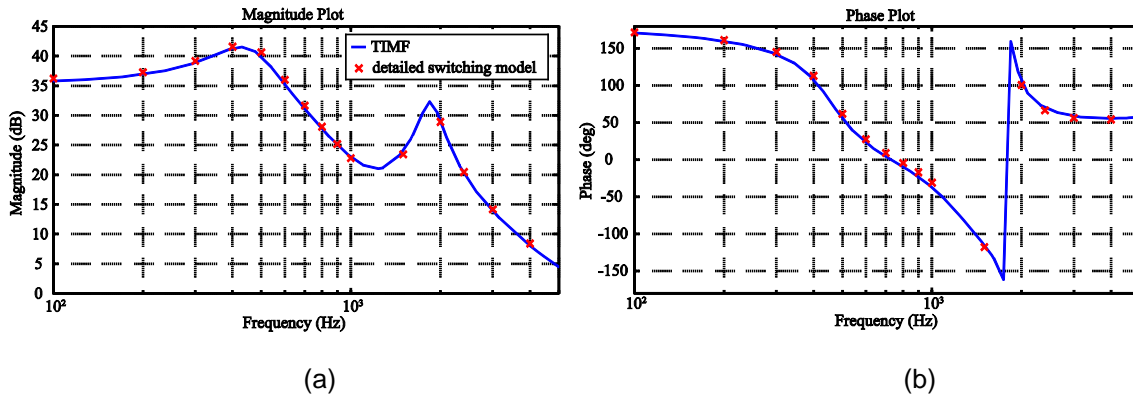
Figure 3.13 Control-to-output transfer function of Cuk converter with sawtooth carrier: (a) magnitude plot (b) phase plot

Magnitude Plot	Phase Plot
(a)	(b)
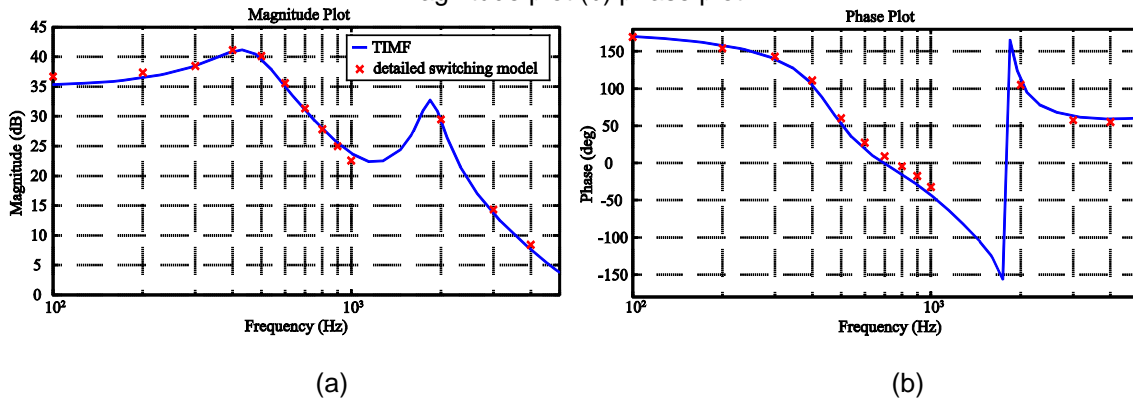
Figure 3.14 Control-to-output transfer function of Cuk converter with triangular carrier: (a) magnitude plot (b) phase plot

3.2.5 Experimental Verifications

A 20W prototype of the PWM DC-DC Cuk converter has been built, and measurement data have been collected for both closed-loop time domain and open-loop frequency domain analyses.

3.2.5.1 Time Domain Response of Cuk converter

3.2.5.1.1 Experimental Setup

For obtaining the closed-loop time-domain response, the Cuk converter labeled as (e) in Figure 3.15 has been constructed. The main objectives are to verify the time-domain responses of the state variables of the Cuk converter predicted by the TIMF model. The values

of each individual component have been displayed in Table 3.2. The step change in load has been achieved by switching from 15Ω load resistance to 10Ω with single pole single throw (SPST) relay. The manufacture number of this relay is T77V1D10-12, and its contact rating is 10A at 12 VDC. This relay has been controlled manually by turning on or off the voltage supply labeled as (a) in Figure 3.15. Two other voltage supplies have been used for the controller circuit and the input power. Microcontroller ATmega32 has been implemented for the controller circuit labeled as (d) in Figure 3.15.
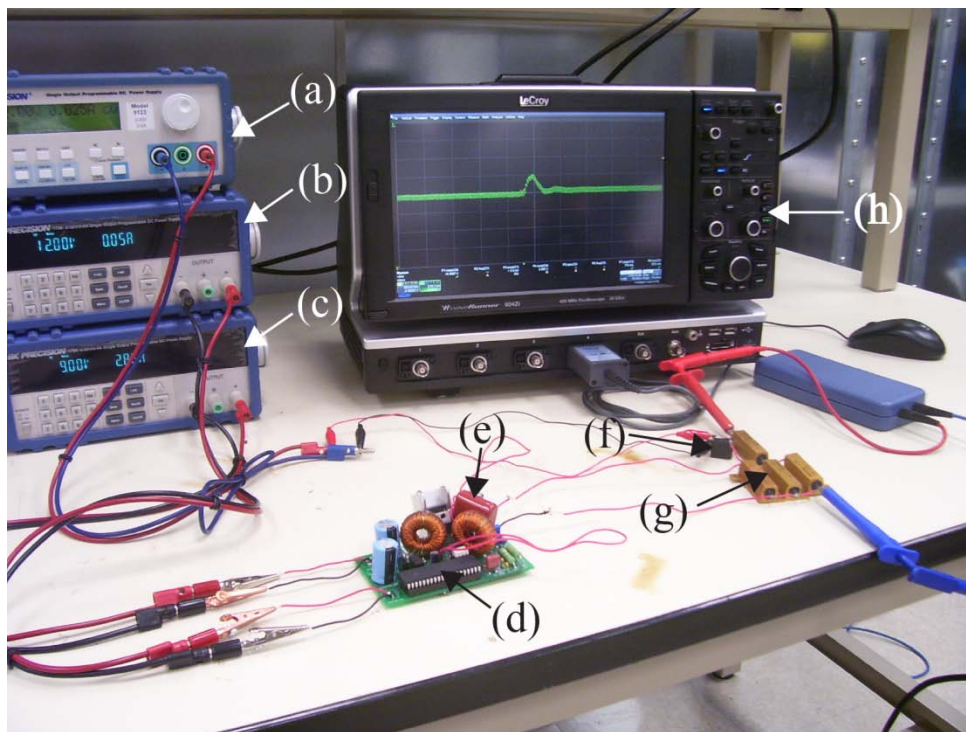
Figure 3.15 Experimental setup for closed-loop controlled Cuk Converter: (a) control voltage for relay, (b) voltage supply for microcontroller, (c) input voltage, (d) microcontroller, (e) microcontroller, (f) relay for changing load resistance, (g) resistive load, and (h) oscilloscope

3.2.5.1.2 Comparison with Simulation Results

The experimental results for the setup described in the previous section are shown in Figure 3.15. Figure 3.16 shows the transient response to a step change of load from 15Ω to 10Ω. Due to noises in the circuit, the experimental results have larger ripples and slightly

distorted waveforms than the simulated results as shown in Figure 3.16(b). Due to the switching loss, the measured inductor current i_{L1} is 0.3A higher than the simulated results. Under closed-loop control, the output power of the converter tends to maintain the same power as in the simulation, but since the switching loss has not been considered in the model, slightly higher current has been observed in the measurement of i_{L1}. Overall, the experimental results match well with the simulation results of TIMF model. The close-up view of time response in the steady state is shown in Figure 3.17.
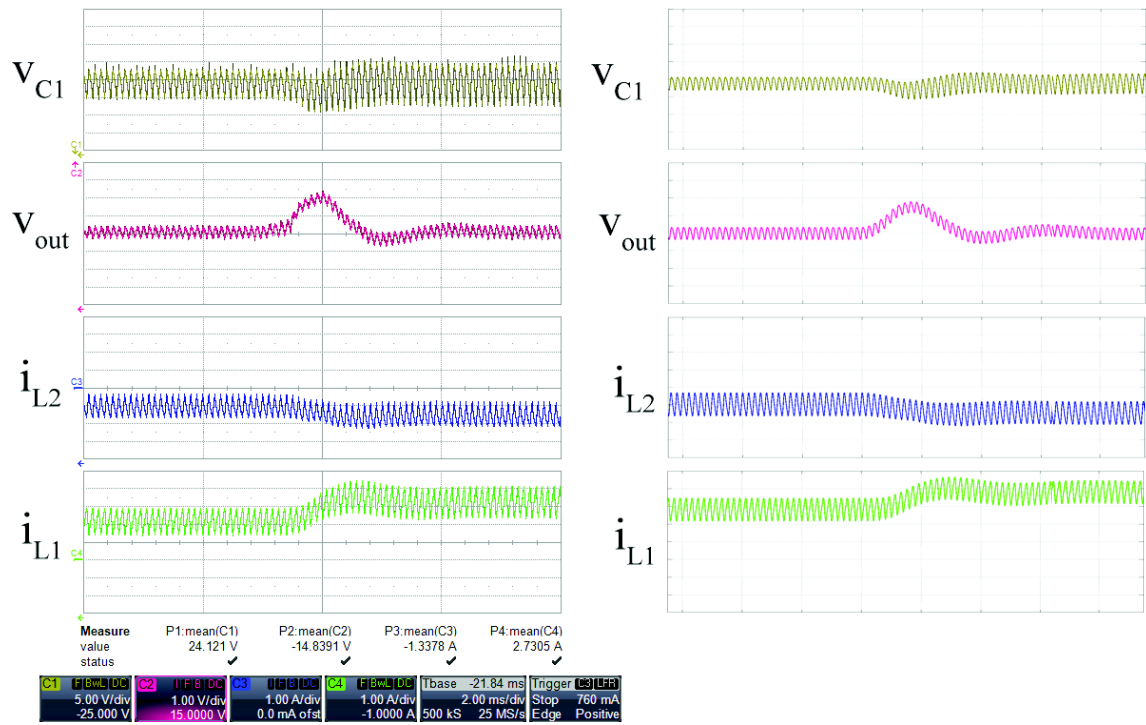
(a)   (b)

Figure 3.16 Comparison between experimental results and simulation results of TI multi-frequency model: (a) experimental results, (b) simulation results
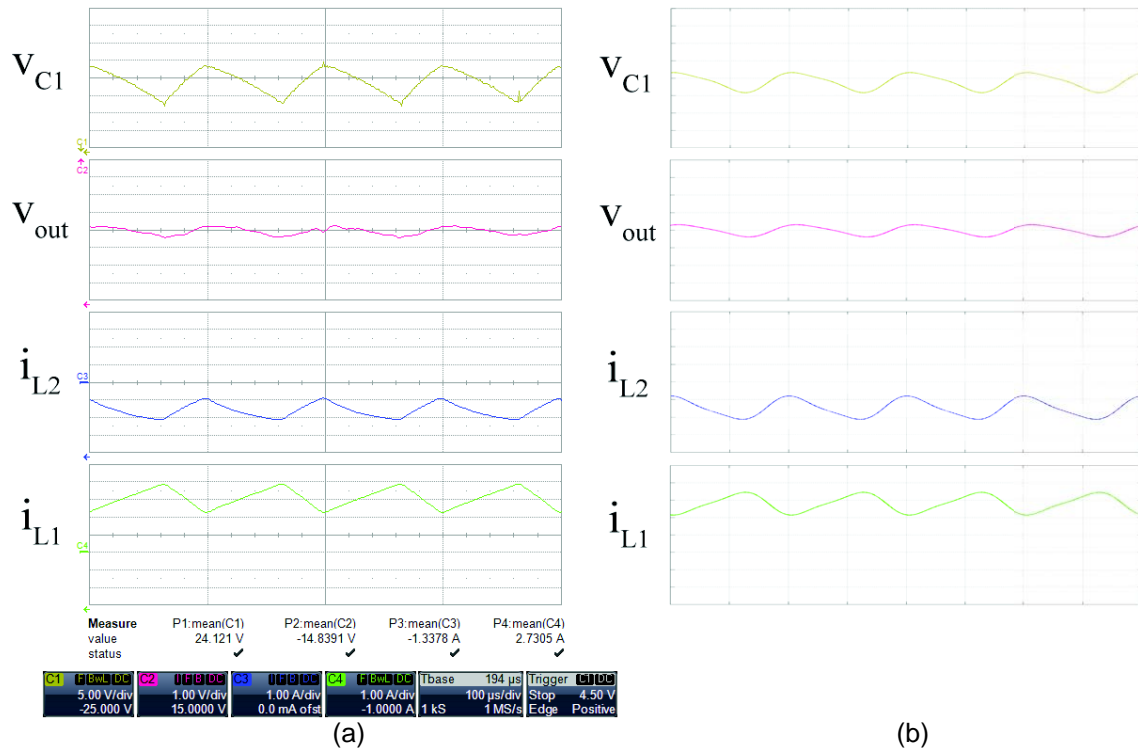
Measure	P1:mean(C1)	P2:mean(C2)	P3:mean(C3)	P4:mean(C4)
value	24.121 V	-14.8391 V	-1.3378 A	2.7305 A
status	✔	✔	✔	✔

C1	BwL DC	C2	BwL DC	C3	BwL DC	C4	BwL DC	Tbase	194 µs	Trigger	C1 DC
	5.00 V/div		1.00 V/div		1.00 A/div		1.00 A/div		100 µs/div	Stop	4.50 V
	-25.000 V		15.0000 V		0.0 mA ofst		-1.0000 A	1 kS	1 MS/s	Edge	Positive

(a)   (b)

Figure 3.17 Close-up view of steady state response: (a) experimental results, (b) simulation results

3.2.5.2 Frequency Response of Cuk converter

3.2.5.2.1 Experimental Setup

For verifying the frequency response of the open-loop Cuk converter modeled by TIMF technique, the Cuk converter has been set up as shown in Figure 3.18. The gating signal has been generated by the modulator, in which duty cycle command of 0.641 has been generated by comparing a sinusoidal wave of amplitude of 50mV at an offset of 1.312V with a sawtooth signal of amplitude 2.724V. A close-up view of the modulator is shown in Figure 3.19. The main component of modulation circuit is TL494, which is a PWM control integrated circuit (IC) from Texas Instruments. By applying the small signal injection and frequency sweep methods, the frequency response of the control-to-output transfer function $\frac{\hat{v}_{out}}{\hat{d}}$ of the Cuk converter has been obtained.
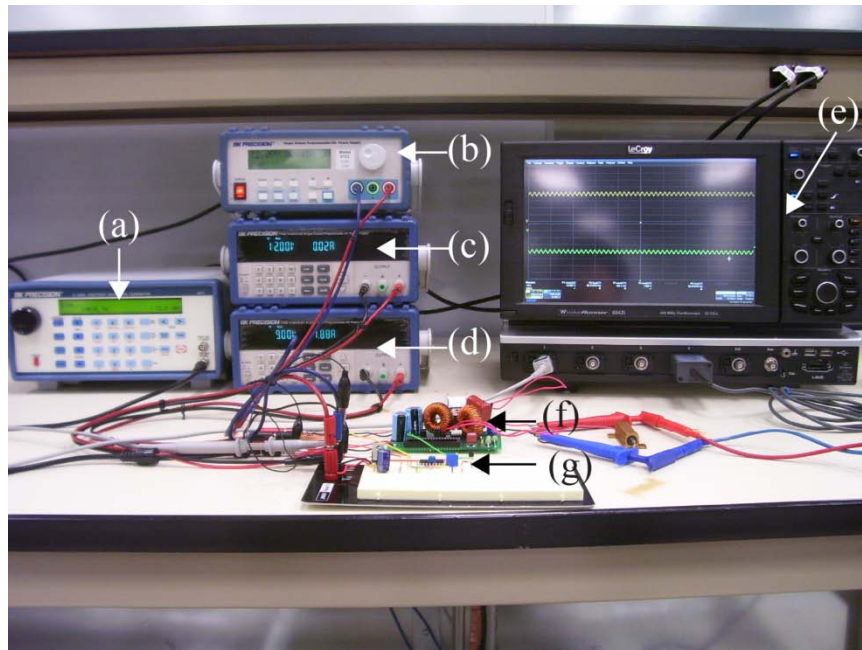
67

Figure 3.18 Experimental setup for obtaining the frequency response of Cuk converter: (a) signal generator for disturbance, (b) voltage supply for the modulator, (c) voltage supply for MOSFET driver, (d) input voltage, (e) oscilloscope, (f) open-loop Cuk converter, (g) modulator
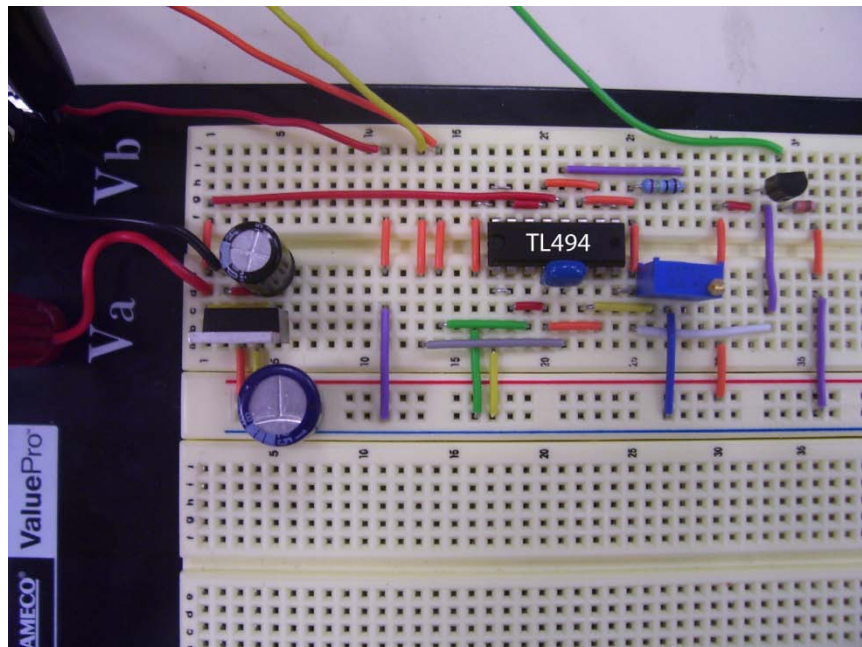

Figure 3.19 Close-up view of the modulation circuit

68

3.2.5.2.2 Comparison with Simulation Results

The experimental results obtained from the setup shown in Figure 3.18 has been depicted in Figure 3.20. As shown in Figure 3.20, the measurement data and TIMF model are approximately the same. This verification assures that the TIMF model is able to capture major dynamical behaviors of the Cuk converter.
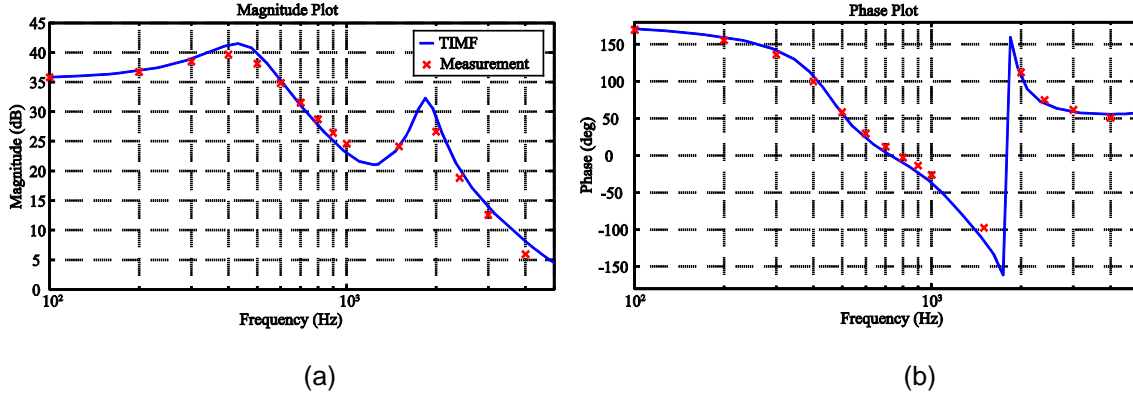

Figure 3.20 Control-to-output transfer function of the Cuk converter with sawtooth carrier: (a) magnitude plot (b) phase plot

3.2.6 Comparison with Existing Time Invariant Techniques

3.2.6.1 Generalized State Space Averaging Model Of Cuk Converter

From the state space model of Cuk converter given by Equations 3.91-3.94, GSSA model can be derived. Only the first order has been derived for the comparison, because the complexity considerable increases for higher order models of GSSA. Although GSSA model of Cuk converter has been presented in [85], the model has not included the parasitic elements, and only open-loop time domain analysis has been done.

In order to derive the GSSA model of Cuk converter, the original state space model (Equations 3.91-3.94) has to be rearranged by applying distributive property, the zero order terms after the rearrangement are

$$\frac{di_{L_1}^0}{dt} = \frac{1}{L_1}(v_g - \left(r_{L_1} + r_m\right)\left\langle qi_{L_1}\right\rangle_0 + r_m\left\langle qi_{L_2}\right\rangle_0 - v_{C_1}^0 - \left(r_{L_1} + r_{C_1} + r_d\right)i_{L_1}^0 - v_d + r_d i_{L_2}^0 +$$

$$\left\langle qv_{C_1}\right\rangle_0 + \left(r_{L_2} + r_{C_1} + r_d\right)\left\langle qi_{L_1}\right\rangle_0 + q_0 v_d - r_d\left\langle qi_{L_2}\right\rangle_0) \tag{3.170}$$

$$\frac{di_{L_2}^0}{dt} = \frac{1}{L_2}(-\left\langle qv_{C_1}\right\rangle_0 - \left(r_{C_1} + r_{L_2} + r_{C_2} + r_m - \frac{r_{C_2}^2}{r_{C_2} + R}\right)\left\langle qi_{L_2}\right\rangle_0 + \left(\frac{r_{C_2}}{r_{C_2} + R} - 1\right)\left\langle qv_{C_2}\right\rangle_0 +$$

$$r_m\left\langle qi_{L_1}\right\rangle_0 - i_{L_2}^0\left(r_{L_2} + r_{C_2} + r_d - \frac{r_{C_2}^2}{r_{C_2} + R}\right) + v_{C_2}^0\left(\frac{r_{C_2}}{r_{C_2} + R} - 1\right) + v_d + r_d i_{L_1}^0 +$$

$$\left\langle qi_{L_2}\right\rangle_0\left(r_{L_2} + r_{C_2} + r_d - \frac{r_{C_2}^2}{r_{C_2} + R}\right) - \left\langle qv_{C_2}\right\rangle_0\left(\frac{r_{C_2}}{r_{C_2} + R} - 1\right) - q_0 v_d - r_d\left\langle qi_{L_1}\right\rangle_0) \tag{3.171}$$

$$\frac{dv_{C_1}^0}{dt} = \frac{1}{C_1}(\left\langle qi_{L_2}\right\rangle_0 + i_{L_1}^0 - \left\langle qi_{L_1}\right\rangle_0) \tag{3.172}$$

$$\frac{dv_{C_2}^0}{dt} = \frac{1}{C_2}(\left(1 - \frac{r_{C_2}}{r_{C_2} + R}\right)i_{L_2}^0 - \frac{v_{C_2}^0}{v_{C_2}^0 + R}) \, . \tag{3.173}$$

The first order terms can be obtained from the zero order terms by dropping the constants from the expressions and adding an extra term $\omega_{sw}x^{1I}$ for the real part, and $-\omega_{sw}x^{1R}$ for imaginary part of each state variable to the end of the right hand side of the equations. The results for the real part of each state variable are

$$\frac{di_{L_1}^{1R}}{dt} = \frac{1}{L_1}(-\left(r_{L_1} + r_m\right)\left\langle qi_{L_1}\right\rangle_{1R} + r_m\left\langle qi_{L_2}\right\rangle_{1R} - v_{C_1}^{1R} - \left(r_{L_1} + r_{C_1} + r_d\right)i_{L_1}^{1R} - v_d + r_d i_{L_2}^{1R} +$$

$$\left\langle qv_{C_1}\right\rangle_{1R} + \left(r_{L_1} + r_{C_1} + r_d\right)\left\langle qi_{L_1}\right\rangle_{1R} + q_{1R} v_d - r_d\left\langle qi_{L_2}\right\rangle_{1R}) + \omega_{sw}i_{L_1}^{1I} \tag{3.174}$$

$$\frac{di_{L_2}^{1R}}{dt} = \frac{1}{L_2}(-\left\langle qv_{C_1}\right\rangle_{1R} - \left(r_{C_1} + r_{L_2} + r_{C_2} + r_m - \frac{r_{C_2}^2}{r_{C_2} + R}\right)\left\langle qi_{L_2}\right\rangle_{1R} +$$

$$+\left(\frac{r_{C_2}}{r_{C_2} + R} - 1\right)\left\langle qv_{C_2}\right\rangle_{1R} + r_m\left\langle qi_{L_1}\right\rangle_{1R} -$$

$$i_{L_2}^{1R}\left(r_{L_2} + r_{C_2} + r_d - \frac{r_{C_2}^2}{r_{C_2} + R}\right) + v_{C_2}^{1R}\left(\frac{r_{C_2}}{r_{C_2} + R} - 1\right) + r_d i_{L_1}^{1R} +$$

$$\left\langle qi_{L_2}\right\rangle_{1R}\left(r_{L_2} + r_{C_2} + r_d - \frac{r_{C_2}^2}{r_{C_2} + R}\right) - \left\langle qv_{C_2}\right\rangle_{1R}\left(\frac{r_{C_2}}{r_{C_2} + R} - 1\right) -$$

$$q_{1R}v_d - r_d\left\langle qi_{L_1}\right\rangle_{1R}) + \omega_{sw}i_{L_2}^{1I} \tag{3.175}$$

$$\frac{dv_{C_1}^{1R}}{dt} = \frac{1}{C_1}(\left\langle qi_{L_2}\right\rangle_{1R} + i_{L_1}^{1R} - \left\langle qi_{L_1}\right\rangle_{1R}) + \omega_{sw}v_{C_1}^{1I} \tag{3.176}$$

$$\frac{dv_{C_2}^{1R}}{dt} = \frac{1}{C_2}\left(\left(1 - \frac{r_{C_2}}{r_{C_2} + R}\right)i_{L2}^{1R} - \frac{v_{C2}^{1R}}{r_{C_2} + R}\right) + \omega_{sw}v_{C_2}^{1I}. \tag{3.177}$$

And the results for imaginary part of each state variable are

$$\frac{di_{L_1}^{1I}}{dt} = \frac{1}{L_1}(-\left(r_{L_1} + r_m\right)\left\langle qi_{L_1}\right\rangle_{1I} + r_m\left\langle qi_{L_2}\right\rangle_{1I} - v_{C_1}^{1I} - \left(r_{L_1} + r_{C_1} + r_d\right)i_{L_1}^{1I} - v_d + r_d i_{L_2}^{1I} +$$

$$\left\langle qv_{C_1}\right\rangle_{1I} + \left(r_{L_1} + r_{C_1} + r_d\right)\left\langle qi_{L_1}\right\rangle_{1I} + q_{1I}v_d - r_d\left\langle qi_{L_2}\right\rangle_{1I}) - \omega_{sw}i_{L_1}^{1R} \tag{3.178}$$

$$\frac{di_{L_2}^{1I}}{dt} = \frac{1}{L_2}(-\left\langle qv_{C_1}\right\rangle_{1I} - \left(r_{C_1} + r_{L_2} + r_{C_2} + r_m - \frac{r_{C_2}^2}{r_{C_2} + R}\right)\left\langle qi_{L_2}\right\rangle_{1I} +$$

$$\left(\frac{r_{C_2}}{r_{C_2} + R} - 1\right)\left\langle qv_{C_2}\right\rangle_{1I} + r_m\left\langle qi_{L_1}\right\rangle_{1I} - i_{L_2}^{1I}\left(r_{L_2} + r_{C_2} + r_d - \frac{r_{C_2}^2}{r_{C_2} + R}\right) +$$

$$v_{C_2}^{1I}\left(\frac{r_{C_2}}{r_{C_2} + R} - 1\right) + r_d i_{L_1}^{1I} + \left\langle qi_{L_2}\right\rangle_{1I}\left(r_{L_2} + r_{C_2} + r_d - \frac{r_{C_2}^2}{r_{C_2} + R}\right) -$$

$$\left\langle qv_{C_2}\right\rangle_{1I}\left(\frac{r_{C_2}}{r_{C_2} + R} - 1\right) - q_{1I}v_d - r_d\left\langle qi_{L_1}\right\rangle_{1I}) - \omega_{sw}i_{L_2}^{iR} \tag{3.179}$$

$$\frac{dv_{C_1}^{1I}}{dt} = \frac{1}{C_1}(\left\langle qi_{L_2}\right\rangle_{1I} + i_{L_1}^{1I} - \left\langle qi_{L_1}\right\rangle_{1I}) - \omega_{sw}v_{C_1}^{1R} \tag{3.180}$$

71

$$\frac{dv_{C_2}^{1l}}{dt} = \frac{1}{C_2}\left(\left(1 - \frac{r_{C_2}}{r_{C_2} + R}\right)i_{L_2}^{1l} - \frac{v_{C_2}^{1l}}{r_{C_2} + R}\right) - \omega_{sw}v_{C_2}^{1R}.$$

(3.181)

3.2.6.2 Krylov-Bogoliubov-Mitropolsky Model of Cuk Converter

A typical Cuk converter is shown in Figure 3.4. When the circuit operates in CCM, there are two different circuit topologies for when the switching is on and when the switching is off as depicted in Figure 3.5. The state space equation has the form of

$$\frac{d}{dt}\begin{bmatrix} i_{L_1} \\ i_{L_2} \\ v_{C_1} \\ v_{C_1} \end{bmatrix} = \{\mathbf{A_1} + h(t,T)\mathbf{A_2}\}\begin{bmatrix} i_{L_1} \\ i_{L_2} \\ v_{C_1} \\ v_{C_1} \end{bmatrix} + \{\mathbf{b_1} + h(t,T)\mathbf{b_2}\},$$

(3.182)

where

$$h(t,T) = u[D - tri(t,T)],$$

(3.183)

$$tri(t,T) = \frac{t \bmod T}{T},$$

(3.184)

$$\mathbf{A_1} = \begin{bmatrix} \dfrac{-(r_{L_1} + r_{C_1} + r_d)}{L_1} & \dfrac{r_d}{L_1} & \dfrac{-1}{L_1} & 0 \\[2em] \dfrac{r_d}{L_2} & \dfrac{-\left(r_{L_2} + r_{C_2} - \dfrac{r_{C_2}^2}{r_{C_2} + R} - r_d\right)}{L_2} & 0 & \dfrac{-1 + \dfrac{r_{C_2}}{r_{C_2} + R}}{L_2} \\[2em] \dfrac{1}{C_1} & 0 & 0 & 0 \\[2em] 0 & \dfrac{1 - \dfrac{r_{C_2}}{r_{C_2} + R}}{C_2} & 0 & \dfrac{\dfrac{-1}{r_{C_2} + R}}{C_2} \end{bmatrix},$$

(3.185)

72

$$\mathbf{A_2} = \begin{bmatrix} \dfrac{r_{C_1} + r_d - r_m}{L_1} & \dfrac{r_m - r_d}{L_1} & \dfrac{1}{L_1} & 0 \\[2mm] \dfrac{r_m - r_d}{L_2} & \dfrac{r_m - r_d - r_{C_1}}{L_2} & \dfrac{-1}{L_2} & 0 \\[2mm] \dfrac{-1}{C_1} & \dfrac{1}{C_1} & 0 & 0 \\[2mm] 0 & 0 & 0 & 0 \end{bmatrix},$$

(3.186)

$$\mathbf{b_1} = \begin{bmatrix} \dfrac{v_g - v_d}{L_1} \\[2mm] \dfrac{v_d}{L_2} \\[2mm] 0 \\[2mm] 0 \end{bmatrix},$$

(3.187)

and

$$\mathbf{b_2} = \begin{bmatrix} \dfrac{v_d}{L_1} \\[2mm] \dfrac{-v_d}{L_2} \\[2mm] 0 \\[2mm] 0 \end{bmatrix},$$

(3.188)

notice that $u[x]$ is defined as a step function. Following the procedure described in [49], the next step in developing the KBM model is to explicitly define ε,

$$\varepsilon = \alpha T ,$$

(3.189)

where α is the largest coefficient in matrices $\mathbf{A_1}$, $\mathbf{A_2}$, $\mathbf{b_1}$, and $\mathbf{b_2}$. Introduce a new variable τ

$$\tau = \frac{t}{T} ,$$

(3.190)

Equation 3.182 becomes

$$\frac{d}{dt} \begin{bmatrix} i_{L_1} \\ i_{L_2} \\ v_{C_1} \\ v_{C_2} \end{bmatrix} = \varepsilon \left\{ \frac{1}{\alpha} \mathbf{A_1} + \frac{1}{\alpha} h(\tau)\mathbf{A_2} \right\} \begin{bmatrix} i_{L_1} \\ i_{L_2} \\ v_{C_1} \\ v_{C_2} \end{bmatrix} + \varepsilon \left\{ \frac{1}{\alpha}\mathbf{b_1} + \frac{1}{\alpha} h(\tau)\mathbf{b_2} \right\},$$

(3.191)

and

$$h(\tau) = u[D - tri(\tau,1)]$$ (3.192)

Applying averaging to the right hand side of Equation 3.191 yields

$$G(y) = \left[\frac{1}{\alpha}\mathbf{A_1} + \frac{D}{\alpha}\mathbf{A_2}\right]y + \frac{1}{\alpha}[\mathbf{b_1} + D\mathbf{b_2}].$$ (3.193)

Use Equation 3.193 to rewrite $\dot{y}$ in the original time-scale

$$\dot{y} = [\mathbf{A_1} + D\mathbf{A_2}]y + \mathbf{b_1} + D\mathbf{b_2}.$$ (3.194)

The next step is to differentiate Equation 2.42 with respect to time,

$$\dot{x} = \dot{y} + \varepsilon\frac{d\Psi_1}{dt} + \varepsilon^2\frac{d\Psi_2}{dt} + \cdots$$ (3.195)

Substitute in Equation 3.191 for $\dot{x}$, Equation 2.42 for x, Equation 2.43 for $\dot{y}$, and

$$\dot{\Psi}_i(\tau,y) = \frac{\partial\Psi_i}{\partial\tau} + \frac{\partial\Psi_i}{\partial y}\dot{y}$$ (3.196)

yields

$$\varepsilon\left\{\frac{1}{\alpha}\mathbf{A_1} + \frac{1}{\alpha}h(\tau)\mathbf{A_2}\right\}\left[y + \varepsilon\Psi_1 + \varepsilon^2\Psi_2 + \cdots\right] + \varepsilon\left\{\frac{1}{\alpha}\mathbf{b_1} + \frac{1}{\alpha}h(\tau)\mathbf{b_2}\right\} =$$

$$\left(\varepsilon G_1 + \varepsilon^2 G_2 + \cdots\right) + \varepsilon\left[\frac{\partial\Psi_1}{\partial\tau} + \frac{\partial\Psi_1}{\partial y}\left(\varepsilon G_1 + \varepsilon^2 G_2 + \cdots\right)\right] +$$

$$\varepsilon^2\left[\frac{\partial\Psi_2}{\partial\tau} + \frac{\partial\Psi_2}{\partial y}\left(\varepsilon G_1 + \varepsilon^2 G_2 + \cdots\right)\right] + \cdots.$$ (3.197)

After equating the coefficients in Equation 3.197, the results are

$$\varepsilon^1 : \left[\frac{1}{\alpha}\mathbf{A_1} + \frac{h(\tau)}{\alpha}\mathbf{A_2}\right]y + \frac{1}{\alpha}\mathbf{b_1} + \frac{h(\tau)}{\alpha}\mathbf{b_2} = G_1 + \frac{\partial\Psi_1}{\partial\tau}$$ (3.198)

$$\varepsilon^2 : \left[\frac{1}{\alpha}\mathbf{A_1} + \frac{h(\tau)}{\alpha}\mathbf{A_2}\right]\Psi_1 = G_2 + \frac{\partial\Psi_1}{\partial y}G_1 + \frac{\partial\Psi_2}{\partial\tau}.$$ (3.199)

$$\vdots$$

Use Equation 3.193 to substitute for G_1 in Equation 3.198, and solve of Ψ_1,

$$\Psi_1 = \frac{1}{\alpha}(\mathbf{A}_2 y - \mathbf{b}_2)\left\{[h(\tau) - D]tri(\tau,1) + [1 - h(\tau)]D + \frac{1}{2}(D^2 - D)\right\}. \tag{3.200}$$

The only unknown in Equation 3.200 is y, however, y can be found from Equation 3.194.

Knowing Ψ_1 and y, state variable x can be approximated by its first order model as

$$x(t) \approx y(t) + \varepsilon\Psi_1(t, y). \tag{3.201}$$

3.2.6.3 Comparison of Open-Loop Frequency Response Simulations

Different modeling techniques discussed in Chapter 2 have been applied to open-loop Cuk converter, and compared with the detailed switching model as shown in Figure 3.21. The harmonics approximation with each modeling techniques has been limited to only first order for comparison purpose. The open-loop Cuk converter parameters are listed in Table 3.3. In detailed switching model, the nonlinearity behavior of the switch is simulated by comparing the duty cycle command d with the sawtooth carrier signal. When the duty cycle command is greater than the carrier signal, the switch is on, and otherwise the switch is off. Due to this close resemblance between the detailed switching model and the real world converter, the detailed switching model has been used here as a reference for checking the accuracy of other modeling techniques. Observing the inductor current waveforms as shown in Figure 3.21(a) and (b), due to the non-linear modeling of the switch, KBM offers the best estimation for the inductor currents. TIMF offers the second best approximation. Floquet theory has the worst approximation because it does not reveal any information about the phase. One explanation to this problem is the fact that in Floquet theory the beginning value and the end value of a state variable during a given switching period is assumed to be the same. Because of this assumption, Floquet theory can only be used to approximate the steady state values of the state variables. The zero order terms from both TIMF and GSSA are almost identical for the inductor currents. For the capacitor voltage v_{C_1} as shown in Figure 3.21(c), the same observation as in the inductor currents has been made. However, in capacitor voltage v_{C2} as shown in Figure 3.21(d), a catastrophe has happened in the KBM model. KBM has only

75

estimated the average value for capacitor voltage v_{C_2}.
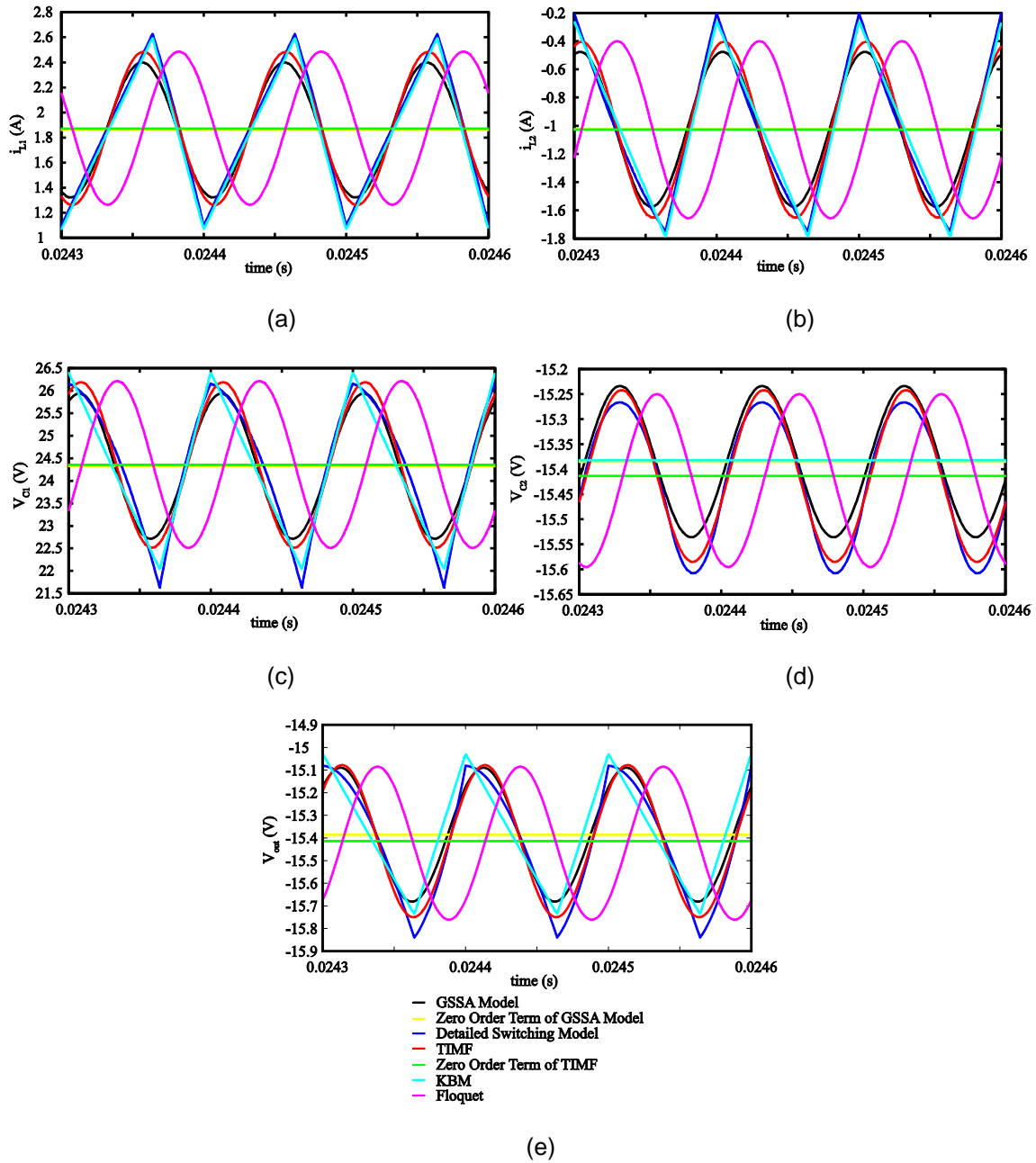

(a)

(b)

(c)

(d)

(e)

Figure 3.21 Comparison of state variables of open-loop Cuk converter: (a) inductor current i_{L1}, (b) inductor current i_{L2}, (c) capacitor voltage v_{C1}, (d) capacitor voltage v_{C2}, and (e) output voltage v_{out}

As a result, it offers the worse approximation among all other modeling technique. One explanation for this catastrophe is that the ripple estimation in KBM depends on the nonlinearity modeling of the switch, and if a state variable does not include the switching function in its state space equation, KBM will only estimate the average value for that state variable. Among other techniques in Figure 3.21(d), TIMF offers the best estimation. Also, the zero order term of GSSA shows an offset when comparing with the actual average value of the detailed switching model. Consequently, in the output voltage as presented in Figure 3.21(e), TIMF shows the best match with the detailed switching model. The zero order term of TIMF presents the best estimation for the average value of the detailed switching model.

The input-to-output transfer functions obtained from different modeling techniques has been plotted in Figure 3.22. Floquet theory has been excluded from this comparison due lack of phase estimation. In Figure 3.22, both TIMF and GSSA show great resemblance with the detailed switching model. The control-to-output transfer functions obtained from different modeling techniques has been presented in Figure 3.23. The same observation has been made in Figure 3.22 can be applied to the bode plots for control-to-output transfer functions. TIMF and GSSA still show better match for the detailed switching model than KBM.

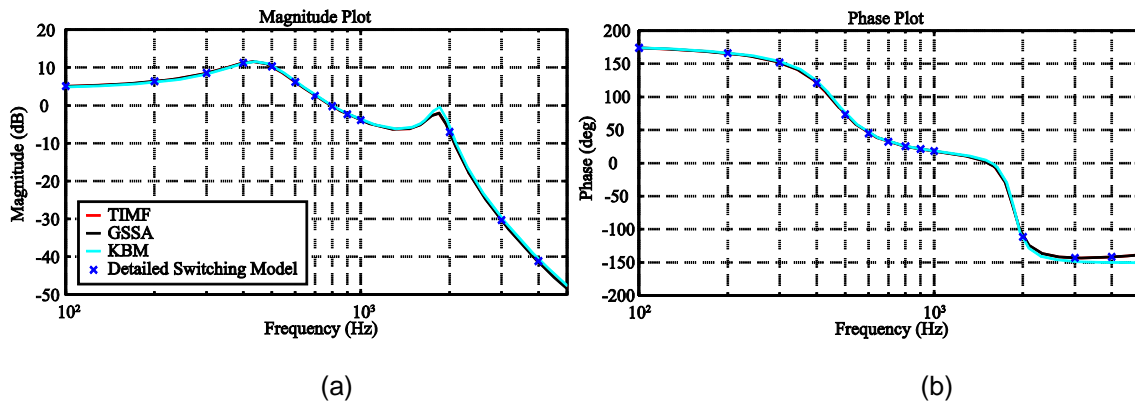(a)   (b)

Figure 3.22 Bode plots for input-to-output transfer function of open-loop Cuk converter: (a) magnitude plot and (b) phase plot
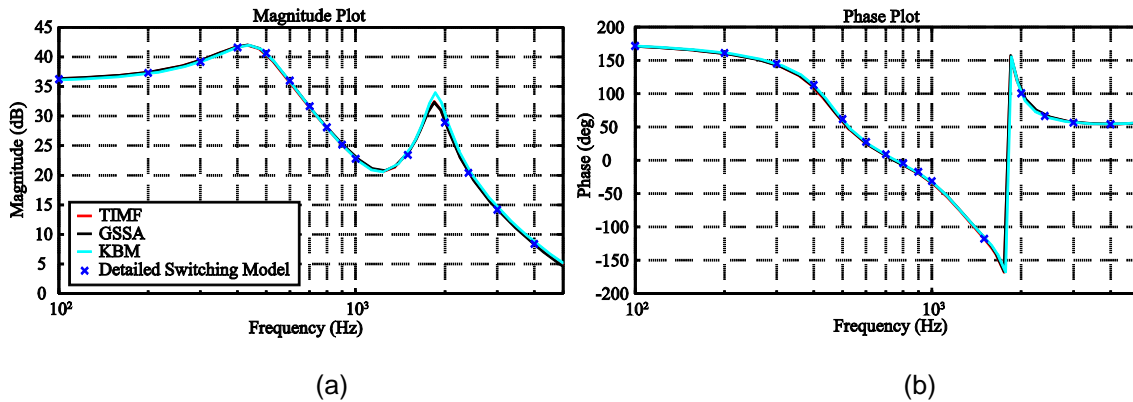
Figure 3.23 Bode plots for control-to-output transfer function of open-loop Cuk converter: (a) magnitude plot and (b) phase plot

After comparing both open-loop time domain response and frequency domain response, one can make the conclusion that TIMF shows the best match for the detailed switching model among all other model techniques that have been discussed in this work. Table 3.6 summarizes the distinct features of different modeling techniques.

Table 3.6 Comparison of Different Modeling Techniques

	SSA/CA	KBM	GSSA	Floquet	TIMF
Ripple Estimation	No	Yes	Yes	Yes	Yes
Discrepancy at Low Frequency	Yes	No	No	No	No
Carrier Signal Dependent Modeling	No	No	No	No	Yes
Model Construnction	Easy	Difficult	Moderate	Difficult	Easy
Closed-Loop Control	Yes	Yes	Yes	No	Yes
Higher Order Model	N/A	Difficult	Moderate	Difficult	Moderate
DCM/CCM	Both	CCM	CCM	Both	CCM

<u>3.3 Case Study for Zeta Converter</u>

3.3.1 Model Construction

   The schematic diagram of the Zeta converter including parasitic components is shown in Figure 3.24. Due to the floated switch of Zeta converter, a separate voltage supply of isolated ground is required for the MOSFET driver. If isolated ground is not possible, p-channel MOSFET often has been used for the switch, and an additional gate driving circuit is needed to drive the switch. The two switching states of the Zeta converter have been shown in Figure 3.25.
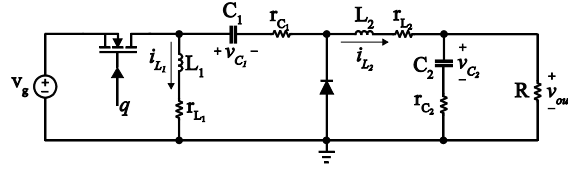

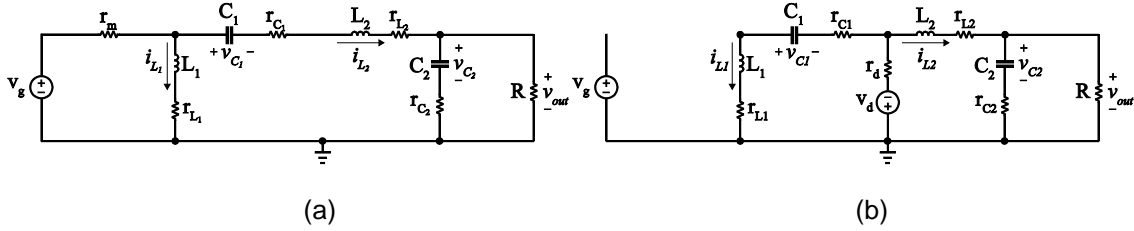Figure 3.24 Zeta converter including parasitic components

| (a) | (b) |

Figure 3.25 Zeta converter in CCM: (a) when q is on and (b) when q is off

The resulting state space model is

$$L_1 \frac{di_{L_1}}{dt} = q\left(v_g - \left(r_m + r_{L_1}\right)i_{L_1} - r_m i_{L_2}\right) +$$

$$(1-q)\left[-\left(r_{L_1} + r_{C_1} + r_d\right)i_{L_1} - r_d i_{L_2} + v_{C_1} - v_d\right] \tag{3.202}$$

$$L_2 \frac{di_{L_2}}{dt} =$$

$$q\left[v_g - r_m i_{L_1} - \left(r_m + r_{C_1} + r_{L_2} + \frac{r_{C_2}R}{r_{C_2} + R}\right)i_{L_2} - v_{C_1} - \frac{R}{R + r_{C_2}}v_{C_2}\right] +$$

$$(1 - q)\left[-r_d i_{L_1} - \left(r_d + r_{L_2} + \frac{r_{C_2} R}{r_{C_2} + R} \right) i_{L_2} - \frac{R}{R + r_{C_2}} v_{C_2} - v_d \right] \tag{3.203}$$

$$C_1 \frac{dv_{C_1}}{dt} = q i_{L_2} + (1 - q)\left(-i_{L_1} \right) \tag{3.204}$$

$$C_2 \frac{dv_{C_2}}{dt} = \frac{R}{R + r_{C_2}} i_{L_2} - \frac{1}{R + r_{C_2}} v_{C_2} . \tag{3.205}$$

Also the output voltage is

$$v_{out} = \frac{r_{C_2} R}{R + r_{C_2}} i_{L_2} + \frac{R}{R + r_{C_2}} v_{C_2} . \tag{3.206}$$

By applying rules discussed in Table 3.1, TIMF model can be easily developed from the state space model, as presented in Equation 3.207-3.210

$$L_1\left(-\mathbf{\Omega i_{L_1}} + \frac{d\mathbf{i_{L_1}}}{dt} \right) = \mathbf{Q}\left(v_g - \left(r_m + r_{L_1} \right)\mathbf{i_{L_1}} - r_m \mathbf{i_{L_2}} \right) + \tag{3.207}$$

$$(\mathbf{I_5} - \mathbf{Q})\left[-\left(r_{L_1} + r_{C_1} + r_d \right)\mathbf{i_{L_1}} - r_d \mathbf{i_{L_2}} + \mathbf{v_{C_1}} - \mathbf{v_d} \right]$$

$$L_2\left(-\mathbf{\Omega i_{L_2}} + \frac{d\mathbf{i_{L_2}}}{dt} \right) = \tag{3.208}$$

$$\mathbf{Q}\left[\mathbf{v_g} - r_m \mathbf{i_{L_1}} - \left(r_m + r_{C_1} + r_{L_2} + \frac{r_{C_2} R}{r_{C_2} + R} \right)\mathbf{i_{L_2}} - \mathbf{v_{C_1}} - \frac{R}{R + r_{C2}} \mathbf{v_{C_2}} \right] +$$

$$(\mathbf{I_5} - \mathbf{Q})\left[-r_d \mathbf{i_{L_1}} - \left(r_d + r_{L_2} + \frac{r_{C_2} R}{r_{C_2} + R} \right)\mathbf{i_{L_2}} - \frac{R}{R + r_{C_2}} \mathbf{v_{C_2}} - \mathbf{v_d} \right]$$

$$C_1\left(-\mathbf{\Omega v_{C_1}} + \frac{d\mathbf{v_{C_1}}}{dt} \right) = \mathbf{Q i_{L_2}} + (\mathbf{I_5} - \mathbf{Q})\left(-\mathbf{i_{L_1}} \right) \tag{3.209}$$

$$C_2\left(-\mathbf{\Omega v_{C_2}} + \frac{d\mathbf{v_{C_2}}}{dt} \right) = \frac{R}{R + r_{C_2}} \mathbf{i_{L_2}} - \frac{1}{R + r_{C_2}} \mathbf{v_{C_2}} , \tag{3.210}$$

where for $N > 2$, $\mathbf{\Omega}$, $\mathbf{i_{L_1}}$, $\mathbf{i_{L_2}}$, $\mathbf{v_{C_1}}$ and $\mathbf{v_{C_2}}$ are defined in Equations 3.103-3.104 and

$$\mathbf{v_d}^T = \begin{bmatrix} v_d & 0 & 0 & 0 & 0 \end{bmatrix} \tag{3.211}$$

$$\mathbf{v_g}^T = \begin{bmatrix} v_g & 0 & 0 & 0 & 0 \end{bmatrix}. \tag{3.212}$$

3.3.2 Closed-Loop Time Domain Analysis

The same procedure performed for the time domain analysis of the Cuk converter has been performed to the Zeta converter. The component values have been carefully chosen so that the converter operates in the CCM. The schematic diagram of closed-loop controlled Zeta converter is presented in Figure 3.26. Both detailed switching model and TIMF model have been simulated in SIMULINK. The component values used for the simulations have been presented in Table 3.7. The solver used for the simulations is ode45 (Dormand-Prince), with max step size of 10^{-5} and relative tolerance of 10^{-3}. Both sawtooth and triangular carriers have been used for time domain analysis. For observing the transient response of the Zeta converter, the load decreases from 10Ω to 5Ω at time $t = 0.5$ in seconds. With state variables modeled by the second order ($N = 2$) and duty cycle command modeled by first order ($N = 1$), the transient response of the Zeta converter has been shown in Figure 3.27(a). A close-up view of the transient response has been shown in Figure 3.27(b). Overall, the TIMF model shows matched well with detailed switching model. However, the ripples of the state variables have been found to be slightly larger than the detailed switching model in the steady state as shown in Figure 3.27(c). This slight discrepancy is due to the neglect of high order terms in the QFS representation of state variables and the duty cycle command. In order to illustrate the point, the order of the duty cycle command model has been increased by one using Equation 3.131. The resulting plots have been shown in Figure 3.28. Comparing the transient response in Figure 3.27(b) and Figure 3.28(b), one can conclude that the waveforms have been slightly improved as the order of duty cycle command increases. The ripples in the TIMF model has been greatly reduced as can be observed by comparing Figure 3.27(c) and Figure 3.28(c). The results can

81

be greatly improved when the order of both state variables and duty cycle command are increased to sixth order, as shown in Figure 3.29. In the case of triangular carrier signal, as shown in Figure 3.30, slightly better results have also been obtained when comparing with the sawtooth case as shown in Figure 3.27. When using the triangular carrier, the waveform of v_{C2} of TIMF model has less clipping or sharp edges than using the sawtooth carrier, as shown in Figure 3.30(b). Less clipping avoids the high frequency terms that are needed for good approximation with TIMF model. Therefore, the error is less when triangular carrier is implemented. However, this error is usually relatively small compared to the magnitude of the ripples in the state variables.

Table 3.7 Parameter values of Zeta converter used in time-domain analysis

Parameter	v_g	L_1	L_2	C_1	C_2	f_{sw}	v_d	r_d
Value	15 V	100 µH	200 µH	100 µF	55 µF	100kHz	0.4 V	14 mΩ

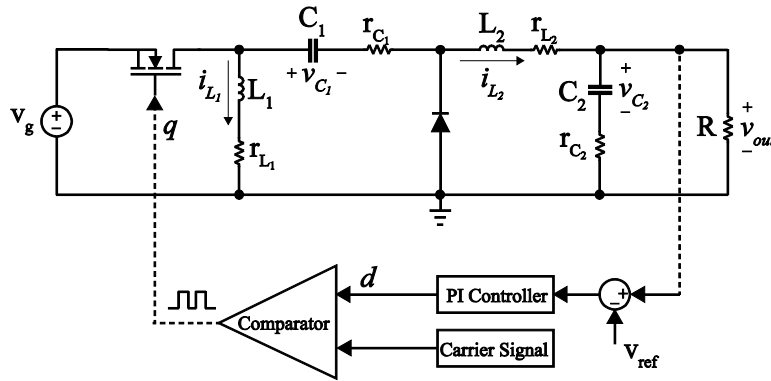| Parameter	r_m	r_{L_1}	r_{L_2}	r_{C_1}	r_{C_2}	v_{ref}	k_p	k_i
Value	0.07 Ω	1 mΩ	0.55 mΩ	0.19 Ω	95 mΩ	5 V	0.005	4

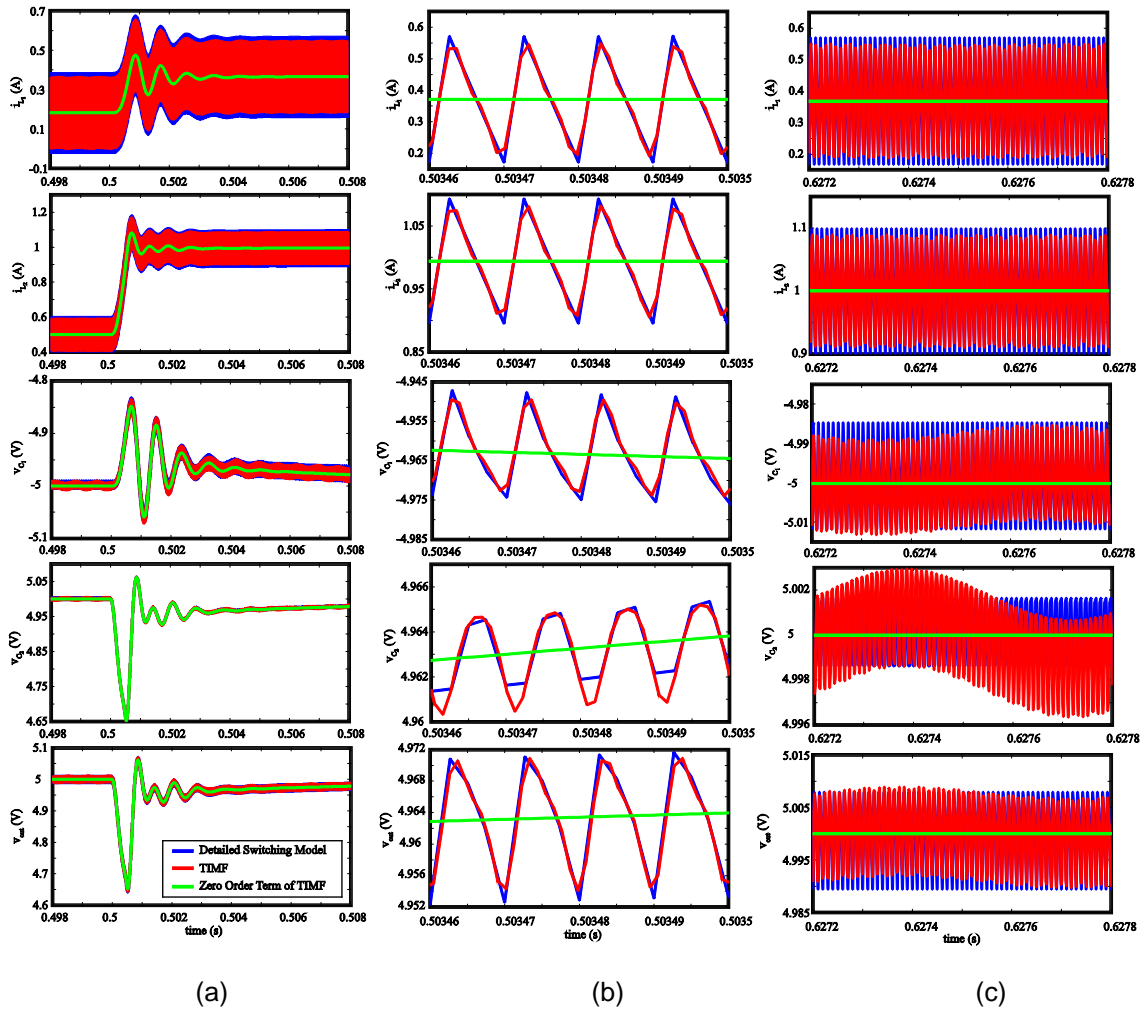Figure 3.26 The schematic diagram of PI controlled Zeta converter

Figure 3.27 Comparison between detailed switching model of Zeta Converter and the second order TIMF model of Zeta converter with first order model of PI controller in the case of sawtooth carrier: (a) Zoom-out view of the transient response, (b) Close-up view of the transient response, and (c) Steady state response
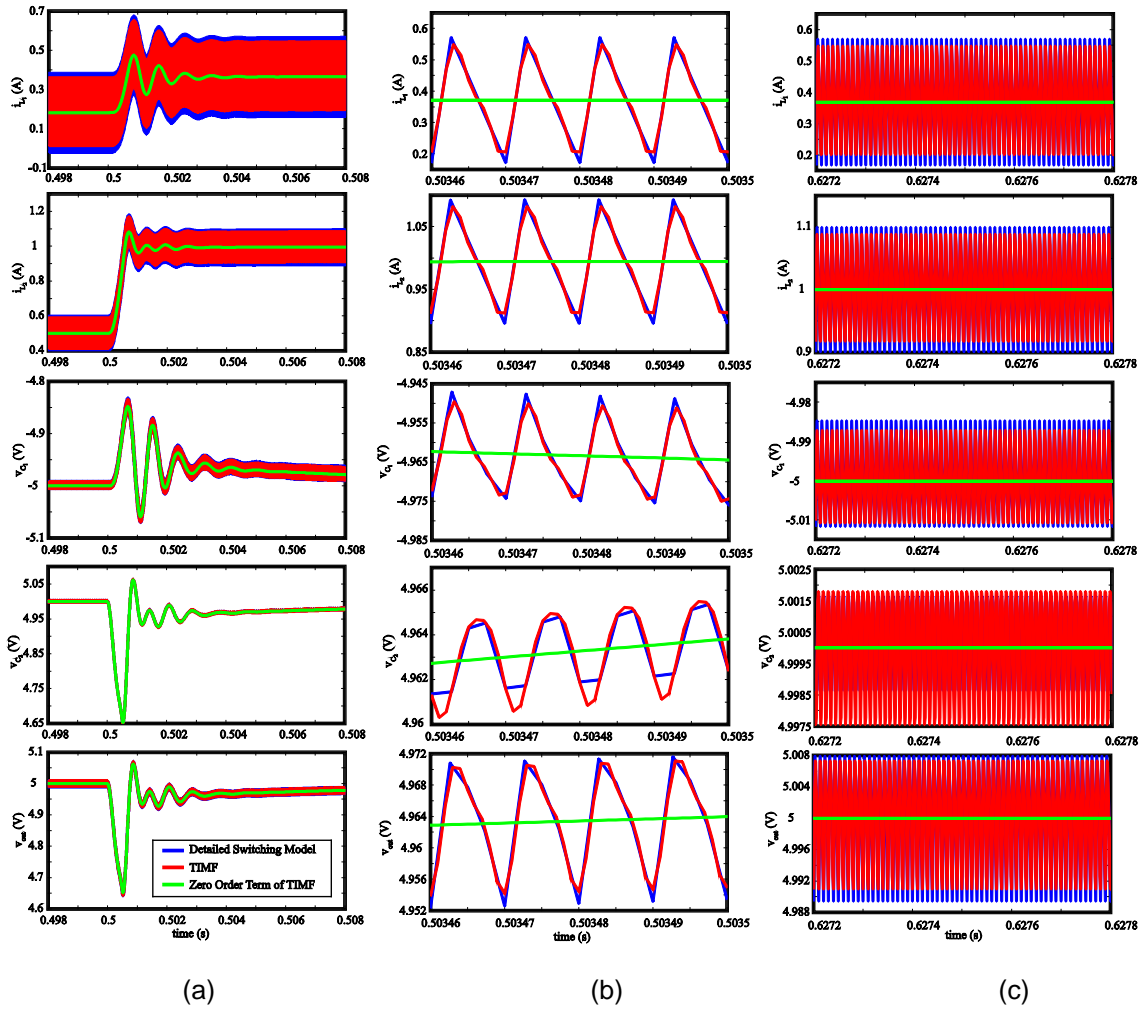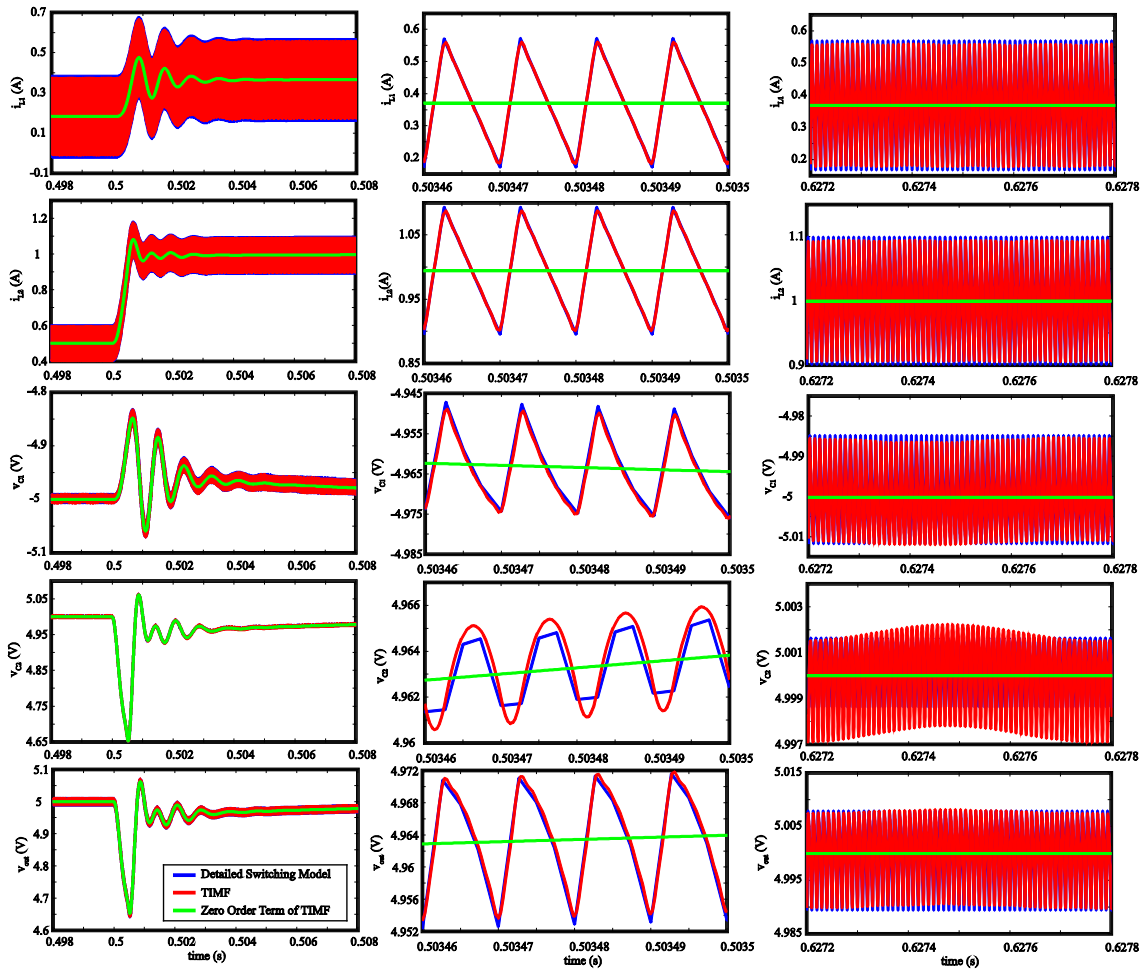
83

Figure 3.28 Comparison between detailed switching model of Zeta Converter and the second order TIMF model of Zeta converter with second order model of PI controller in the case of sawtooth carrier: (a) Zoom-out view of the transient response, (b) Close-up view of the transient response, and (c) Steady state response

Figure 3.29 Comparison between detailed switching model of Zeta Converter and the sixth order TIMF model of Zeta converter with sixth order model of PI controller in the case of sawtooth carrier: (a) Zoom-out view of the transient response, (b) Close-up view of the transient response, and (c) Steady state response
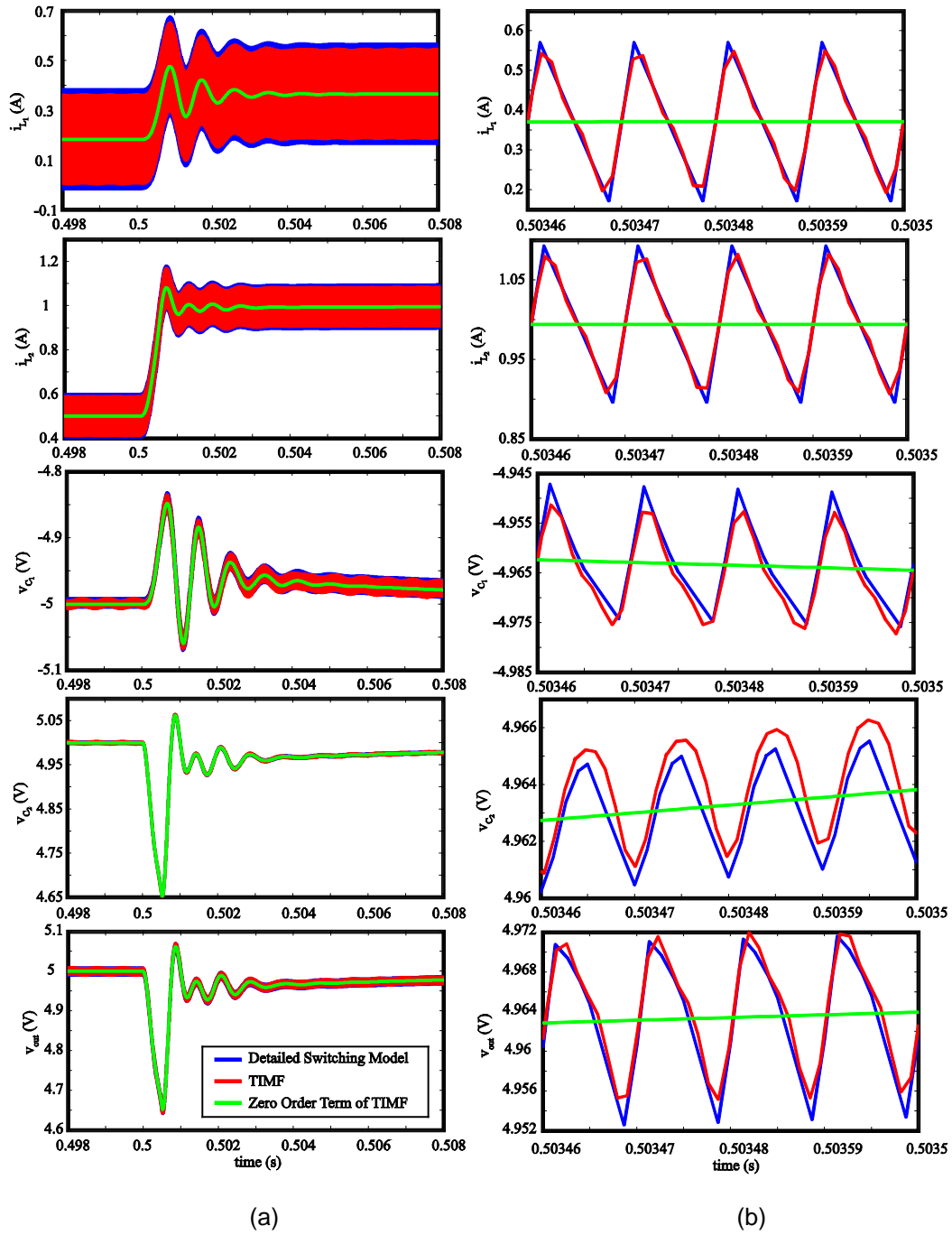
85

Figure 3.30 Comparison between detailed switching model of Zeta Converter and the second order TIMF model of Zeta converter with first order model of PI controller in the case of triangular carrier: (a) Zoom-out view of the transient response and (b) Close-up view of the transient response

86

3.3.3 Frequency Domain

In this section, the small-signal input-to-output transfer function $\frac{\hat{v}_{out}}{\hat{v}_g}$ and small-signal control-to-output transfer function $\frac{\hat{v}_{out}}{\hat{d}}$ of the open-loop Zeta converter have been extracted and compared with the detailed switching model. To extract the transfer functions from the TIMF model, linmod command from MATLAB has been used. To obtain the bode plots from the detailed switching model, small signal injection and frequency sweep method has been exploited, as previously discussed in the Cuk converter. Zeta converter as presented in Figure 3.23 has been simulated in SIMULINK, and the output of each state variable has been exported to the workspace in MATLAB. The second order model of state variables and first order model of the duty command cycle have been implemented in this section. The parameter values used for simulating the Zeta converter has been presented in Table 3.8. For extracting the input-to-output transfer function $\frac{\hat{v}_{out}}{\hat{v}_g}$ and the control-to-output transfer function $\frac{\hat{v}_{out}}{\hat{d}}$ in the detailed switching model, the circuit topologies shown in Figure 3.31 and Figure 3.32 have been implemented, respectively. The frequency responses obtained from both models have been examined up to 50 kHz.

Table 3.8 Parameter values of Zeta converter used in frequency-domain analysis

Parameter	v_g	L_1	L_2	C_1	C_2	f_{sw}	v_d	r_d
Value	15 V	100 µH	200 µH	100 µF	55 µF	100kHz	0.4 V	14 mΩ

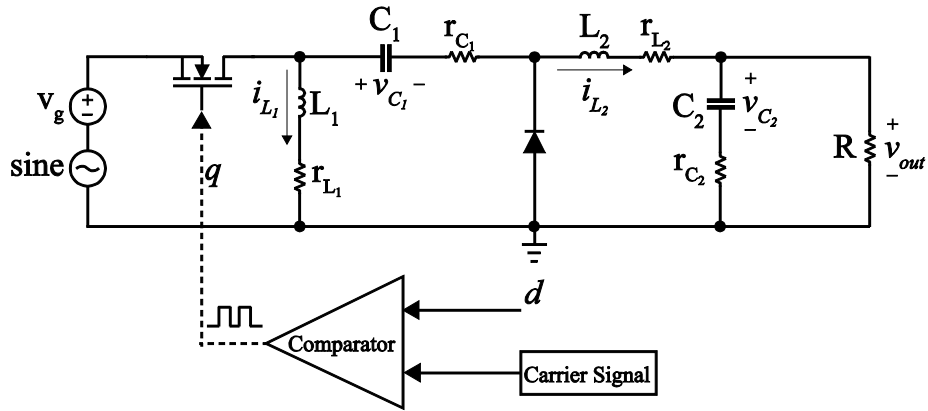| Parameter	r_m	r_{L_1}	r_{L_2}	r_{C_1}	r_{C_2}	R	D	
Value	0.07 Ω	1 mΩ	0.55 mΩ	0.19 Ω	95 mΩ	5 Ω	0.27	

Figure 3.31 Small signal injection for extract input-to-output transfer function of Zeta converter
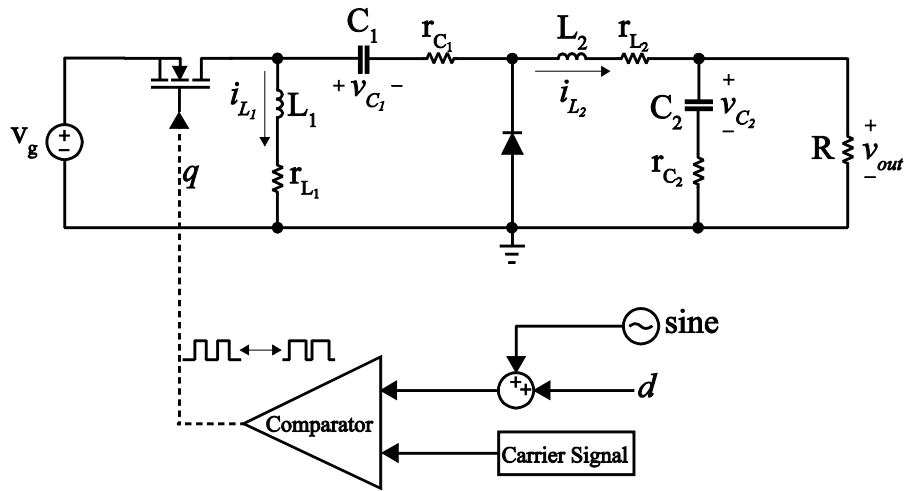

Figure 3.32 Small signal injection for extract control-to-output transfer function of Zeta converter

Using method discussed before, the bode plot of input-to-output transfer function $\dfrac{\hat{v}_{out}}{\hat{v}_g}$

have been obtained. By implementing sawtooth carrier, the magnitude and phase plots are

shown in Figure 3.33. The plots for triangular carrier are shown in Figure 3.34. In both cases,

the TIMF model is almost identical to the detailed switching model. The same conclusion can be

made to explain the bode plots for control-to-output transfer function $\dfrac{\hat{v}_{out}}{\hat{d}}$, as shown in Figure

3.35 and 3.36. Unlike the input-to-output transfer function case where the initial conditions for all

states are zero, the operating points for the control-to-output transfer function in its steady state as listed in Table 3.9 and Table 3.10.
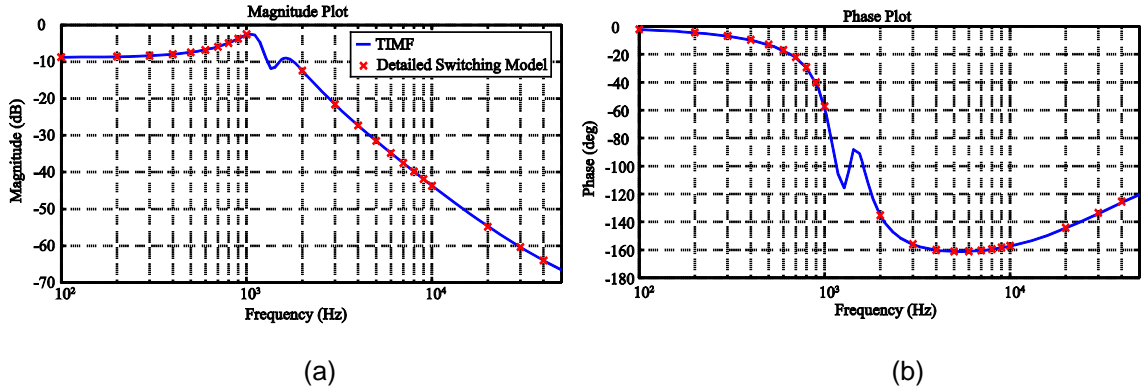

(a)   (b)

Figure 3.33 Input-to-output transfer function of Zeta converter with sawtooth carrier: (a) magnitude plot (b) phase plot

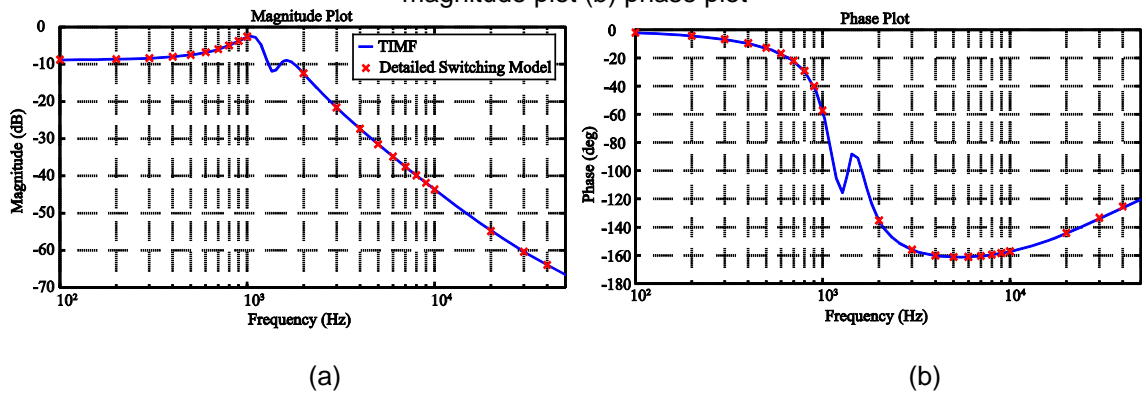(a)   (b)

Figure 3.34 Input-to-output transfer function of Zeta converter with triangular carrier: (a) magnitude plot (b) phase plot
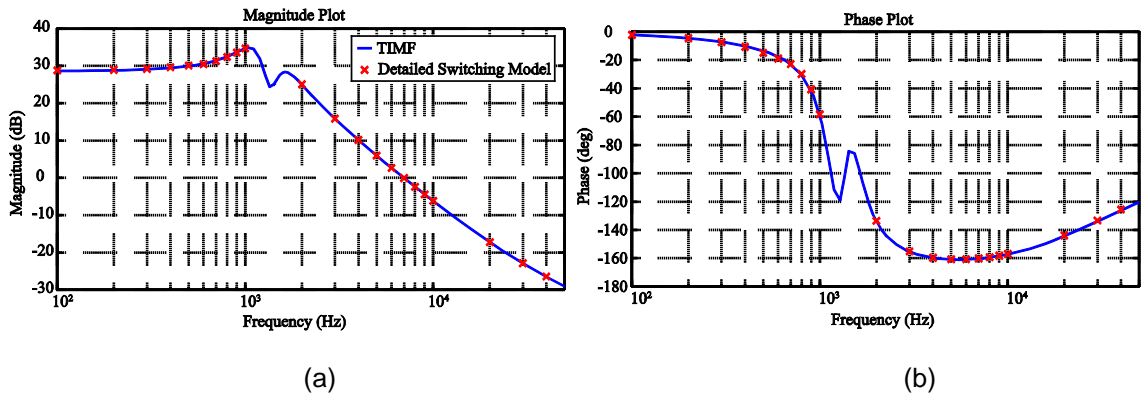

(a)   (b)

Figure 3.35 Control-to-output transfer function of Zeta converter with sawtooth carrier: (a) magnitude plot (b) phase plot
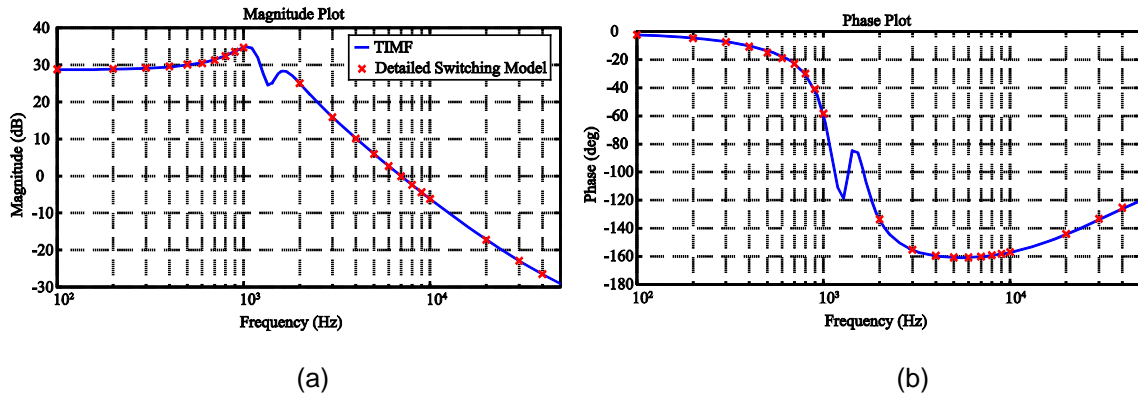
89

(a)   (b)

Figure 3.36 Control-to-output transfer function of Zeta converter with triangular carrier: (a) magnitude plot (b) phase plot

Table 3.9 Operating points for detailed switching model of control-to-output transfer function of Zeta converter

Detailed Switching Model	
i_{L_1}	0.3716 A
i_{L_2}	1.0042 A
v_{C_1}	-5.0214 V
v_{C_2}	5.0212 V

Table 3.10 Operating points for TIMF model of control-to-output transfer function of Zeta converter

TIMF Model							
$i_{L_1\_0}$	0.3716 A	$i_{L_2\_0}$	0.3716 A	$v_{C_1\_0}$	-5.0214 V	$v_{C_2\_0}$	5.0212 V
$i_{L_1\_\alpha_1}$	-0.1162 A	$i_{L_2\_\alpha_1}$	-0.1162 A	$v_{C_1\_\alpha_1}$	-6.68 mV	$v_{C_2\_\alpha_1}$	-0.0145 V
$i_{L_1\_\beta_1}$	0.1029 A	$i_{L_2\_\beta_1}$	0.1029 A	$v_{C_1\_\beta_1}$	8.24 mV	$v_{C_2\_\beta_1}$	-1.62 mV
$i_{L_1\_\alpha_2}$	-0.0509 A	$i_{L_2\_\alpha_2}$	-0.0509 A	$v_{C_1\_\alpha_2}$	3.407 mV	$v_{C_2\_\alpha_2}$	43.16 µV
$i_{L_1\_\beta_2}$	-6.39 mA	$i_{L_2\_\beta_2}$	-6.39 mA	$v_{C_1\_\beta_2}$	-6.29 mV	$v_{C_2\_\beta_2}$	-0.356 mV

3.4 Case Study for SEPIC

3.4.1 Model Construction

In this section, the state space model including parasitic components has been developed for the single-ended primary-inductor converter (SEPIC) which is shown in Figure

3.37. Figure 3.38 illustrates the different switching states for SEPIC in CCM. As a result, the state space model is

$$L_1 \frac{di_{L_1}}{dt} = q\left[v_g - \left(r_{L_1} + r_m\right)i_{L_1} + r_m i_{L_2}\right] + (1-q)*$$

$$\left[v_g - \left(r_{L_1} + r_{C_1} + r_d + \frac{r_{C_2}R}{r_{C_2}+R}\right)i_{L_1} + \left(r_d + \frac{r_{C_2}R}{r_{C_2}+R}\right)i_{L_2} - v_{C_1} - \frac{R}{r_{C_2}+R}v_{C_2} - v_d\right] \quad (3.213)$$

$$L_2 \frac{di_{L_2}}{dt} = q\left[r_m i_{L_1} - \left(r_m + r_{C_1} + r_{L_2}\right)i_{L_2} - v_{C_1}\right] + (1-q)*$$

$$\left[\left(\frac{r_{C_2}R}{r_{C_2}+R} + r_d\right)i_{L_1} - \left(r_d + r_{L_2} + \frac{r_{C_2}R}{r_{C_2}+R}\right)i_{L_2} + \frac{R}{r_{C_2}+R}v_{C_2} + v_d\right] \quad (3.214)$$

$$C_1 \frac{dv_{C_1}}{dt} = qi_{L_2} + (1-q)i_{L_1} \quad (3.215)$$

$$C_2 \frac{dv_{C_2}}{dt} = q\left(\frac{-1}{r_{C_2}+R}v_{C_2}\right) +$$

$$(1-q)\left[\frac{R}{r_{C_2}+R}i_{L1} - \frac{R}{r_{C_2}+R}i_{L2} + \frac{R}{r_{C_2}+R}v_{C_2} + v_d\right]. \quad (3.216)$$

Using Table 3.1, second order TIMF model has been developed from the state space model

$$L_1\left(-\mathbf{\Omega i_{L_1}} + \frac{d\mathbf{i_{L_1}}}{dt}\right) = \mathbf{Q}\left[\mathbf{v_g} - \left(r_{L_1} + r_m\right)\mathbf{i_{L_1}} + r_m\mathbf{i_{L_2}}\right] + \left(\mathbf{I_5} - \mathbf{Q}\right)*$$

$$\left[\mathbf{v_g} - \left(r_{L_1} + r_{C_1} + r_d + \frac{r_{C_2}R}{r_{C_2}+R}\right)\mathbf{i_{L_1}} + \left(r_d + \frac{r_{C_2}R}{r_{C_2}+R}\right)\mathbf{i_{L_2}} - \mathbf{v_{C_1}} - \frac{R}{r_{C_2}+R}\mathbf{v_{C_2}} - \mathbf{v_d}\right] \quad (3.217)$$

$$L_2\left(-\mathbf{\Omega i_{L_2}} + \frac{d\mathbf{i_{L_2}}}{dt}\right) = \mathbf{Q}\left[r_m\mathbf{i_{L_1}} - \left(r_m + r_{C_1} + r_{L_2}\right)\mathbf{i_{L_2}} - \mathbf{v_{C_1}}\right] + \left(\mathbf{I_5} - \mathbf{Q}\right)*$$

$$\left[\left(\frac{r_{C_2}R}{r_{C_2}+R} + r_d\right)\mathbf{i_{L_1}} - \left(r_d + r_{L_2} + \frac{r_{C_2}R}{r_{C_2}+R}\right)\mathbf{i_{L_2}} + \frac{R}{r_{C_2}+R}\mathbf{v_{C_2}} + \mathbf{v_d}\right] \quad (3.218)$$

91

$$C_1\left(-\boldsymbol{\Omega}\mathbf{v_{C1}} + \frac{d\mathbf{v_{C1}}}{dt}\right) = \mathbf{Q}\mathbf{i_{L2}} + \left(\mathbf{I_5} - \mathbf{Q}\right)\mathbf{i_{L1}} \tag{3.219}$$

$$C_2\left(-\boldsymbol{\Omega}\mathbf{v_{C_2}} + \frac{d\mathbf{v_{C_2}}}{dt}\right) = \mathbf{Q}\left(\frac{-1}{r_{C_2} + R}\mathbf{v_{C_2}}\right) +$$

$$\left(\mathbf{I_5} - \mathbf{Q}\right)\left[\frac{R}{r_{C_2} + R}\mathbf{i_{L_1}} - \frac{R}{r_{C_2} + R}\mathbf{i_{L_2}} + \frac{R}{r_{C_2} + R}\mathbf{v_{C_2}} + \mathbf{v_d}\right]. \tag{3.220}$$

where the vectors $\boldsymbol{\Omega}$, $\mathbf{i}_{L_1}$, $\mathbf{i}_{L_2}$, $\mathbf{v}_{C_1}$, $\mathbf{v}_{C_2}$, $\mathbf{v_d}$ and $\mathbf{v_g}$ are defined in Equations 3.103-3.107, and
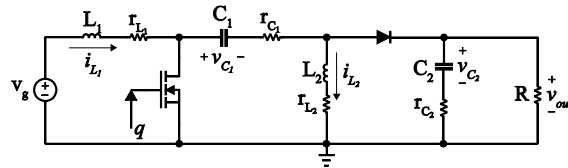
3.211-3.212.

Figure 3.37 SEPIC with parasitic components

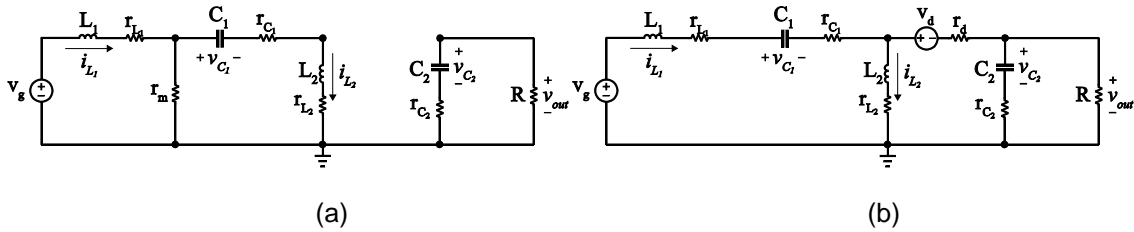(a)   (b)

Figure 3.38 Circuit diagram of SEPIC in CCM: (a) when q is on and (b) when q is off
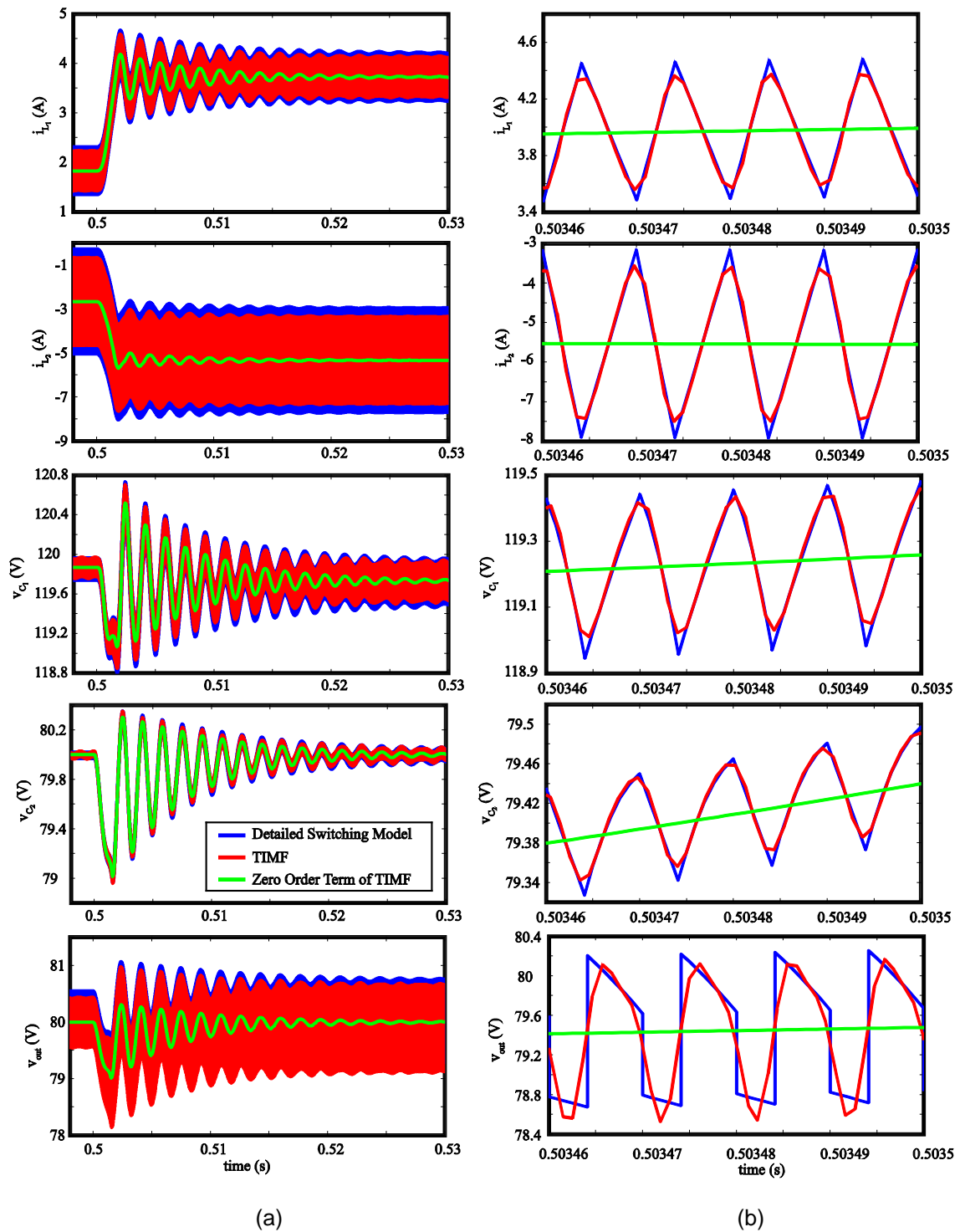
Figure 3.39 Transient response of detailed switching model and TIMF of SEPIC with sawtooth carrier: (a) zoom-out view and (b) close-up view
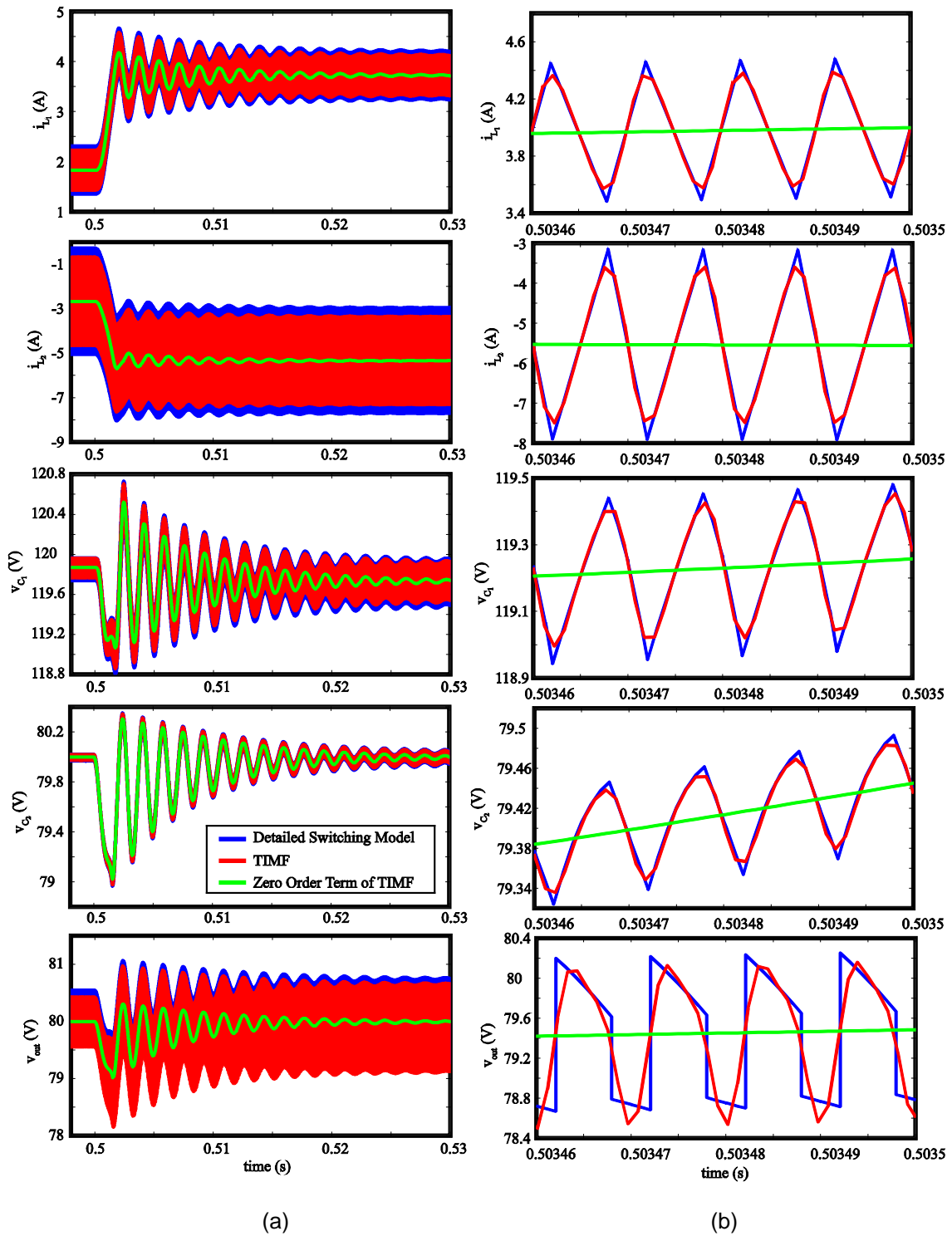
Figure 3.40 Transient response of detailed switching model and TIMF of SEPIC with triangular carrier: (a) zoom-out view and (b) close-up view

Table 3.11 Parameter values of SEPIC used in time-domain analysis

Parameter	v_g	L_1	L_2	C_1	C_2	f_{sw}	v_d	r_d
Value	120 V	500 µH	100 µH	47 µF	200 µF	100kHz	0.4 V	1 mΩ

Parameter	r_m	r_{L_1}	r_{L_2}	r_{C_1}	r_{C_2}	v_{ref}	k_p	k_i
Value	7 mΩ	10 mΩ	20 mΩ	0.53 Ω	125 mΩ	80 V	0.007	2

Table 3.12 Parameter values of SEPIC used in frequency-domain analysis

Parameter	v_g	L_1	L_2	C_1	C_2	f_{sw}	v_d	r_d
Value	120 V	500 µH	100 µH	47 µF	200 µF	100kHz	0.4 V	1 mΩ

Parameter	r_m	r_{L_1}	r_{L_2}	r_{C_1}	r_{C_2}	R	D	
Value	7 mΩ	10 mΩ	20 mΩ	0.53 Ω	125 mΩ	15 Ω	0.4	

3.4.2 Closed-Loop Time Domain Analysis

In this section, the second order TIMF model given by Equations 3.217-3.220 of SEPIC has been simulated in SIMULINK and compared with the detailed switching model. The configuration parameters for the SIMULINK is the same as in the case of Zeta converter, maximum step size of 10^{-5}, relative tolerance of 10^{-3}, and ode45 (Dormand-Prince) as the solver. Parameter values of SEPIC used in time-domain analysis has bee shown in Table 3.11. As the load resistance decreases from 30Ω to 15Ω at $t = 0.5$, the transient responses are captured for second order TIMF model in the case of sawtooth carrier and triangular carrier, as shown in Figure 3.39 and 3.40. The plots show that TIMF model match well with the detailed switching model.

3.4.3 Open-Loop Frequency Domain Analysis

In this section, the bode plots of the small-signal input-to-output transfer function $\frac{\hat{v}_{out}}{\hat{v}_g}$

and small-signal control-to-output transfer function $\frac{\hat{v}_{out}}{\hat{d}}$ of TIMF model of the open-loop SEPIC

have been obtained and compared with the data obtained from the detailed switching model. Parameter values of SEPIC used in frequency-domain analysis has been shown in Table 3.12. In order to obtain the data points of the input-to-output transfer function for the detailed switching model, Figure 3.41 has been implemented in SIMULINK. In the case of sawtooth carrier, the bode plots are shown in Figure 3.43. In the case of triangular carrier, the bode plots are shown in Figure 3.44. For control-to-output transfer function $\frac{\hat{v}_{out}}{\hat{d}}$, the operating point is set according to Table 3.13 and Table 3.14. By implementing the schematic shown in Figure 3.42, one can easily obtain the magnitude and phase at different frequency for the detailed switching model. The bode plots for sawtooth and triangular carriers are shown in Figure 3.45 and 3.46. Small discrepancy has been observed in the phase plots at the higher frequencies, this is due to the neglect of high frequency terms in the TIMF model. Overall the results of TIMF match well with the detailed switching model.
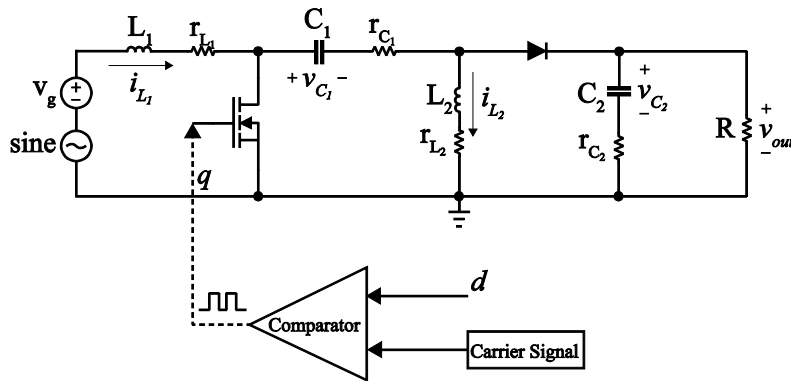

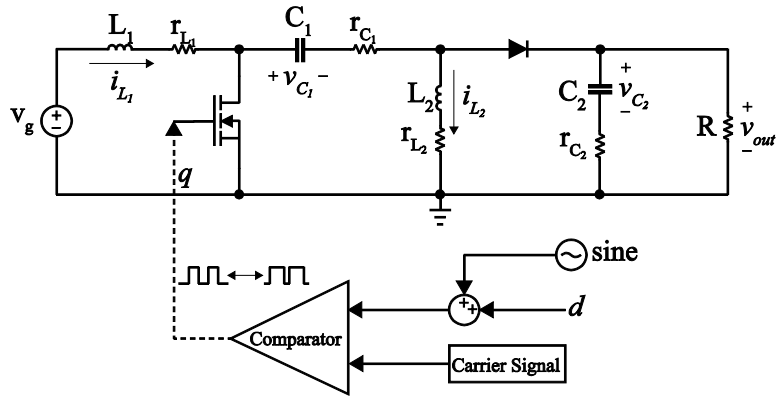Figure 3.41 Small signal injection for extract input-to-output transfer function of SEPIC

Figure 3.42 Small signal injection for extract control-to-output transfer function of SEPIC

Table 3.13 Operating points for detailed switching model of control-to-output transfer function of SEPIC

Detailed Switching Model	
i_{L_1}	3.4092 A
i_{L_2}	-5.1042 A
v_{C_1}	119.761 V
v_{C_2}	76.5629 V

Table 3.14 Operating points for TIMF model of control-to-output transfer function of SEPIC

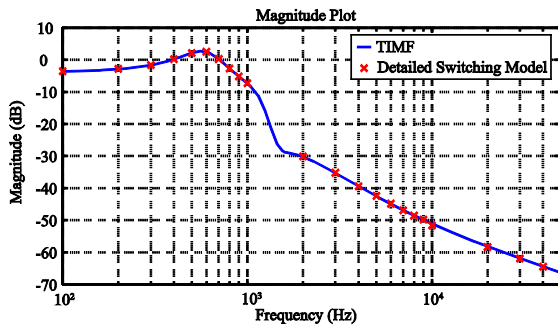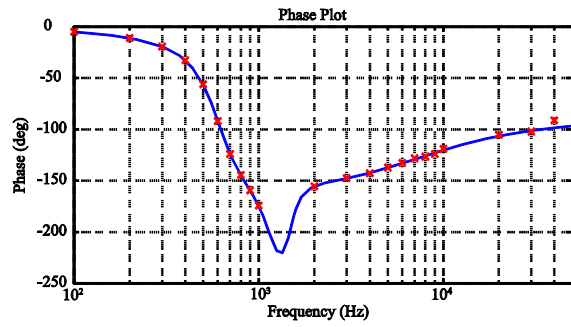| TIMF Model					
$i_{L_1\_0}$	3.4092 A	$i_{L_2\_0}$	-5.1042 A	$v_{C_1\_0}$	119.761 V	$v_{C_2\_0}$	76.5629 V
$i_{L_1\_\alpha_1}$	-0.3635 A	$i_{L_2\_\alpha_1}$	1.7742 A	$v_{C_1\_\alpha_1}$	0.1705 V	$v_{C_2\_\alpha_1}$	0.0351 V
$i_{L_1\_\beta_1}$	0.119 A	$i_{L_2\_\beta_1}$	-0.5877 A	$v_{C_1\_\beta_1}$	-0.0407 V	$v_{C_2\_\beta_1}$	-0.0235 V
$i_{L_1\_\alpha_2}$	-0.0347 A	$i_{L_2\_\alpha_2}$	0.1725 A	$v_{C_1\_\alpha_2}$	5.4681 V	$v_{C_2\_\alpha_2}$	2.1898 V
$i_{L_1\_\beta_2}$	3.4092 A	$i_{L_2\_\beta_2}$	-5.1042 A	$v_{C_1\_\beta_2}$	119.761 V	$v_{C_2\_\beta_2}$	76.5629 V
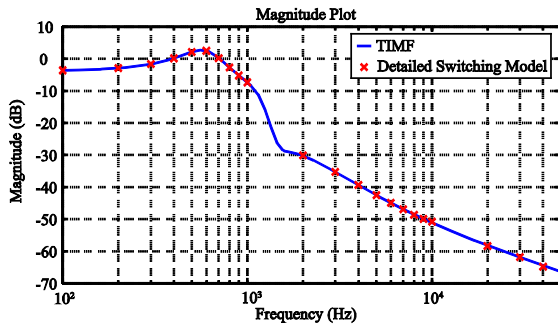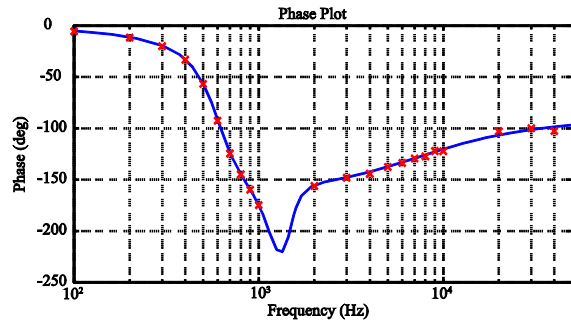
Figure 3.43 Input-to-output transfer function of SEPIC with sawtooth carrier: (a) magnitude plot (b) phase plot
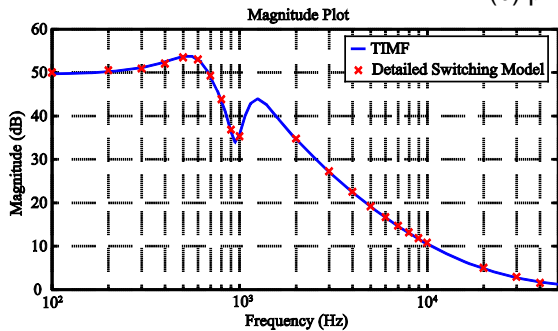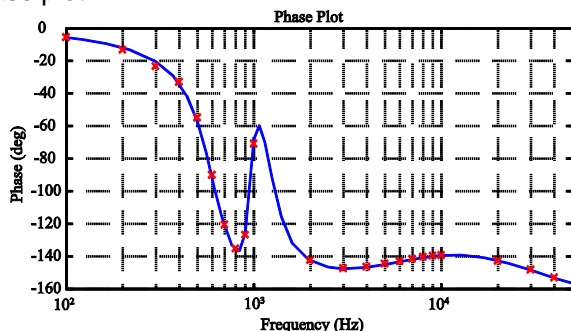

Figure 3.44 Input-to-output transfer function of SEPIC with triangular carrier: (a) magnitude plot (b) phase plot

Figure 3.45 Control-to-output transfer function of SEPIC with sawtooth carrier: (a) magnitude plot (b) phase plot
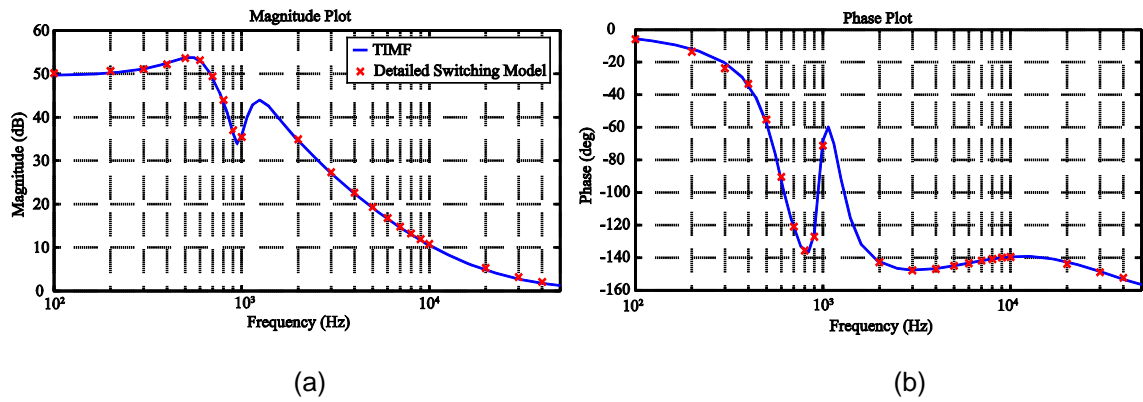
Figure 3.46 Control-to-output transfer function of SEPIC with triangular carrier: (a) magnitude plot (b) phase plot

CHAPTER 4

CONCLUSION

4.1 Contribution

In this thesis, the state space models with parasitic elements for higher order converters such as Cuk converter, SEPIC and zeta converter, have been developed. TIMF model has been applied to these higher order converters and compared with the detailed switching model for both time domain response and frequency domain response. In this thesis, the process of converting from state space model to TIMF model has been simplified by defining a set of rules. With these rules, the TIMF model with higher order harmonics can be obtained. Experimental verification for TIMF has been done using Cuk converter. Experimental results show great match between TIMF and the measurement data in both time domain and frequency domain. Lastly, the existing models have been simulated and compared with TIMF model of open-loop Cuk converter in both time domain and frequency domain. TIMF presents itself as the best candidate for modeling higher order converters.

4.2 Future work

TIMF provides a convenient way to achieve high accuracy for estimating the inductor current and capacitor voltage waveforms. TIMF model can be further improved by including the switching losses in the model. It would be of great interest to extend TIMF to other classes of converters such as soft switching converters, resonant converters, and inverters. In this paper, the controllers have been developed based on voltage mode control (VMC). For future work, current mode control and nonlinear control methods can also be added to the list. In [48], TIMF has been utilized to model multiple-input buck-boost converter. For future research, TIMF can be applied to model multiple-input multiple output (MIMO) converters.

APPENDIX A

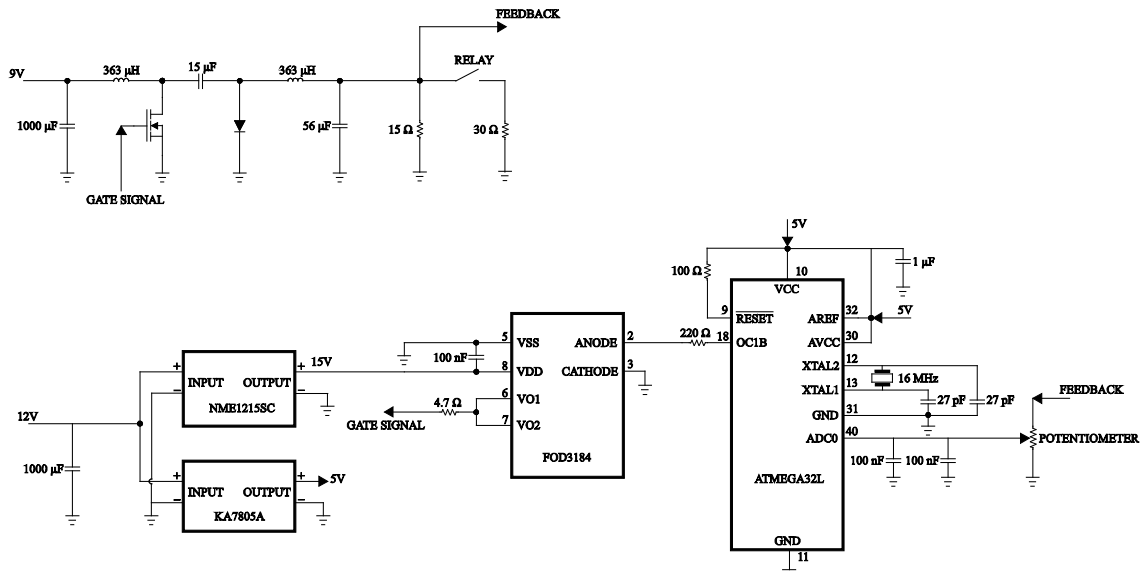SCHEMATIC DIAGRAMS FOR CUK CONVERTER

Figure A.1 Schematic diagrams for Cuk Converter used in time domain analysis of the experimental section
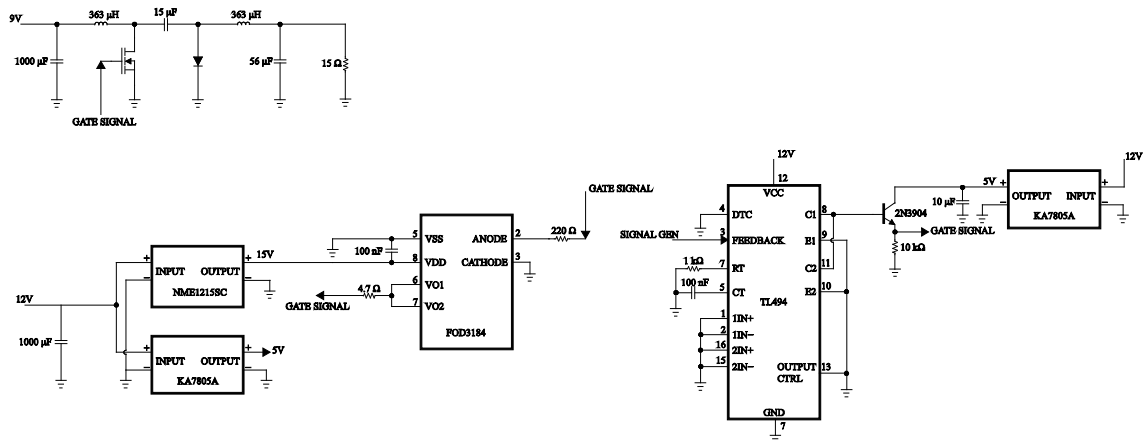

Figure A.2 Schematic diagrams for Cuk Converter used in frequency domain analysis of the experimental section

REFERENCES

[1] W. A. Y. Salah and S. Taib, "Improvement of transformerless 200W SMPS using CUK DC-DC converter," in *Power and Energy 2006 IEEE Int. Conf.*, pp. 497-500.

[2] M. Veerachary and M. Suresh, "Digital voltage-mode control of higher order boost converter," in *Power Syst. Technol. and IEEE Power India Conf.*, 2008, pp. 1-6.

[3] L. Maharjan, T. Yamagishi, H. Akagi, and J. Asakura, "Fault-tolerant operation of a battery-energy-storage system based on a multilevel cascade PWM converter with star configuration," *IEEE Trans. Power Electron.*, vol. 25, no. 9, pp. 2386-2396, Apr. 2010.

[4] L. Xu and V.G. Agelidis, "Flying capacitor multilevel PWM converter based UPFC," *Proc. IEE* vol. 149, no. 4, pp. 304-310, Nov. 2002.

[5] J. G. Lee, S. Y. Choe, J. W. Ahn, and S. H. Baek, "Modeling and simulation of a polymer electrolyte membrane fuel cell system with a PWM DC/DC converter for stationary applications," *IET Power Electron.*, vol. 1, no. 3, pp. 305-317, Aug. 2008.

[6] H. S. H. Chung, K. K. Tse, S. Y. R. Hui, C. M. Mok, and M. T. Ho, "A novel maximum power point tracking technique for solar panels using a SEPIC or Cuk converter," *IEEE Trans. Power Electron.*, vol. 18, no. 3, pp. 717-724, May 2003.

[7] K. B. Park, G. W. Moon, and M. J. Youn, "Nonisolated high step-up boost converter integrated with sepic converter," *IEEE Trans. Power Electron.*, vol. 25, no. 9, pp. 2266-2275, Sept. 2010.

[8] H. F. Lopez, C. Zollmann, and R. Vieri e Fernando S dos Reis, "Photovoltaic panels grid-tied by a zeta converter," *Power Electron. Conf.*, Brazil, 2009, pp. 181-188.

[9] J. Hu, A. D. Sagneri, J. M. Rivas, Y. Han, S. M. Davis, and D. J. Perreault, "High-frequency resonant SEPIC converter with wide input and output voltage ranges," *IEEE Trans. Power Electron.*, vol. 27, no. 1, pp. 189-200, Jan. 2012.

[10] S. B. Kjaer, J. K. Pdersen, and F. Blaabjerg, "Modeling and control of PV charger system with SEPIC converter," *IEEE Trans. Ind. Electron.*, vol. 56, no. 11, pp. 4344-4353, Nov. 2009.

[11] A. Safari, and S. Mekhilef, "Simulation and hardware implementation of incremental conductance MPPT with direct control method using Cuk converter," *IEEE Trans. Ind. Electron.*, vol. 58, no. 4, pp. 1154-1161, Apr. 2011.

[12] D. Murthy-Bellur, and M. K. Kazimierczuk, "Isolated two-transistor zeta converter with reduced transistor voltage stress," *IEEE Trans. Circuits Syst. II, Exp. Briefs*, vol. 58, no. 1, pp. 41-45, Jan. 2011.

[13] S. Yu, R. Zhao, and A. Kwasinski, "Design considerations of a multiple-input isolated single ended primary inductor converter (SEPIC) for distributed generation sources," in *IEEE Energy Convers. Congr. and Exposition*, 2001, pp. 3960-3967.

[14] R. Zhao and A. Kwasinski, "Multiple-input single ended primary inductor converter (SEPIC) converter distributed generation applications," *in IEEE Energy Convers. Congr. and Exposition*, 2009, pp. 1847-1854.

[15] S. C. Tan and Y. M. Lai, "Constant-frequency reduced-state sliding mode current controller for Cuk converters," *IET Power Electron.*, vol.1 no. 4, pp. 466-477, Dec. 2008.

[16] J. Knight, S. Shirsavar, and W. Holderbaum, "An improved reliability Cuk based solar inverter with sliding mode control," *IEEE Trans. Power. Electron.*, vol. 21, no. 4, pp. 1107-1115, Jul. 2006.

[17] D. B. Costa and C.M.C. Duarte, "The ZVS-PWM active-clamping Cuk converter," *IEEE Trans. Ind. Electron.*, vol. 51, no. 1, pp. 54-60, Feb. 2004.

[18] B. R. McGee and R. M. Nelms, "Using a Cuk converter to interface a pulsed load to a fuel cell," in *Energy Convers. Eng. Conf.*, 2002, pp. 313-318.

[19] J. Jung and A. Kwasinski, "A multiple-input SEPIC with a bi-directional input for modular distributed generation and energy storage integration," in *IEEE Applied Power Electron. Conf. and Exposition '11*, pp. 28-34.

[20] H. Ma, J. Lai, Q. Feng, W. Yu, C. Zheng and Z. Zhao, "A novel valley-fill SEPIC-derived power supply without electrolytic capacitor for led lighting application," *IEEE Trans. Power Electron.*, to be published.

[21] B. R. Lin and C. L. Huang, "Analysis and implementation of an integrated sepic-forward converter for photovoltaic based light emitting diode lighting," IET Power Electron., vol 2, no. 6, pp. 635-645, Nov. 2009.

[22] D. C. Martins and G. N. de Abreu, "Application of the zeta converter in switch-mode power supplies," in *IEEE Applied Power Electron. Conf. and Exposition '93*, pp. 28-34.

[23] D. C. Martins and M. M. Casaro, "Isolated three-phase rectifier with high power factor using the zeta converter in continuous conduction mode," *IEEE Trans. Circuits Syst. I, Fundam. Theory Appl.*, vol. 48, no. 1, pp. 74-80, Jan. 2001.

[24] E. Vuthchhay, C. Bunlaksananusorn and H. Hirata, "Dynamic modeling and control of a zeta converter," in *Commun. and Inform. Technol. Int. Symp.*, 2008, pp. 498-503.

[25] B. Lin and Y. Huang, "ZVS double-ended Cuk converter," *IEEE Trans. Circuits. Syst. II, Exp. Briefs*, vol. 57, no. 11, pp. 908-912, Nov. 2010.

[26] C. Liu and J. Lai, "Low Frequency current ripple reduction technique with active control in a fuel cell power system with inverter load," *IEEE Trans. Power Electron.*, vol. 22, no. 4, pp. 1429-1436.

[27] P. T. Krein and R. S. Balog, "Cost-effective hundred-year life for single-phase inverters and rectifiers in solar and LED lighting applications based on minimum capacitance

requirements and a ripple power port," in *IEEE Applied Power Electron. Conf. and Exposition '09*, pp. 620-625.

[28] J. A. Veitch and S. L. McColl, "Modulation of fluorescent light: flicker rate and light source effects on visual performance and visual comfort," *Lighting Research and Technol.*, vol. 27, no. 4, pp. 243-256, 1995.

[29] S. Wang, Y. Zhou, J. Chen, and X. Jiang, "An integrative modeling method and stability analysis of higher order switching converters," in *Electrical Machines and Syst. Int. Conf.*, 2008, pp. 4068-4071.

[30] M. di Bernardo and F. Vasca, "Discrete-time maps for the analysis of bifurcations and chaos in DC/DC converters," *IEEE Trans. Circuits. Syst. I: Fundam. Theory Appl.*, vol 47, no 2, pp. 130-143, Feb. 2000.

[31] Y. Fuad, W. L. de Koning, and J. W. van der Woude, "On the stability of the pulsewidth-modulated Cuk converter," *IEEE Trans. Circuits Syst. II, Exp. Brief*, vol. 51, no. 8, pp. 412-420, Aug. 2004.

[32] A. Cantillo, A. De Nardo, N. Femia, and W. Zamboni, "Stability issues in peak-current-controlled SEPIC," *IEEE Trans. Power Electron.*, to be published.

[33] A. Balestrino, A. Landi, and L. Sani, "Cuk converter global control via fuzzy logic and scaling factors," *IEEE Trans. Ind. Appl.*, vol. 38, no. 2, pp. 406-413, Apr. 2002.

[34] R. W. Erickson and D. Maksimovic, *Fundamentals of Power Electronics*, 2nd ed. New York: Springer, 2001.

[35] V. P. Galigekere and M. K. Kazimierczuk, "Small-signal modeling of PWM Z-source converter by circuit-averaging technique," in *Circuits Syst. Int. Symp.*, 2011, pp. 1600-1603.

[36] E. Van Dijk, J. N. Spruijt, D. M. O'Sullivan, and J. B. Klaassens, "PWM-switch modeling of DC-DC converters," *IEEE Trans. Power Electron.*, vol. 10, no. 6, pp. 659-665, Nov. 1995.

[37] D. Czarkowski and M. K. Kazimierczuk, "Energy-conservation approach to modeling PWM DC-DC converters," *IEEE Trans. Aerosp. Electron. Syst.*, vol. 29, no. 3, pp. 1059-1063, Jul. 1993.

[38] V. Vorperian, R. Tymerski, and F. C. Y. Lee, "Equivalent circuit models for resonant and PWM switches," *IEEE Trans. Power Electron.*, vol. 4, no. 2, pp. 205-214, Apr. 1989.

[39] G. W. Wester and R. D. MiddleBrook, "Low-frequency characterization of switched dc-dc converters," *IEEE Trans. Aerosp. Electron. Syst.*, vol. AES-9, no. 3, pp. 376-385, May 1973.

[40] V. Vorperian, "Simplified analysis of PWM converters using model of PWM switch part I: continuous conduction mode," *IEEE Trans. Aerosp. Electron. Syst.*, vol. 26, no. 3, pp. 490-496, May 1990.

[41] V. Vorperian, "Simplified analysis of PWM converters using model of PWM switch part II: discontinuous conduction mode," *IEEE Trans. Aerosp. Electron. Syst.*, vol. 26, no. 3, pp. 497-505, May 1990.

[42] S. Cuk, "Modeling, analysis, and design of switching converters," Ph.D. dissertation, Elect. Eng. Dept., California Insti. of Technol., 1977.

[43] H. R. Visser and P. P. J. van den Bosch, "Modelling of periodically switching networks," in *IEEE Power Electron. Specialists Conf.*, 1991, pp. 67-73.

[44] R. D. Middlebrook and S. Cuk, "A general unified approach to modeling switching-converter power stages," in *IEEE Power Electron. Specialists Conf.*, 1976, pp. 18-34.

[45] S. R. Sanders and G. C. Verghese, "Synthesis of averaged circuit models for switched power converters," *IEEE Trans. Circuits Syst.*, vol 38, no. 8, pp. 905-915, Aug. 1991.

[46] V. A. Caliskan, O. C. Verghese, and A. M. Stankovic, "Multifrequency averaging of DC/DC converters," *IEEE Trans. Power Electron.*, vol 14, no. 1, pp. 124-133, Jan. 1999.

[47] S. R. Sanders, J. M. Noworolski, X. Z. Liu, and G. C. Verghese, "Generalized averaging method for power conversion circuits," *IEEE Trans. Power Electron.*, vol. 6, no. 2, pp. 251-259, Apr. 1991.

[48] J. M. Noworolski and S. R. Sanders, "Generalized in-plane circuit averaging," in *IEEE Applied Power Electron. Conf. and Exposition '91*, pp. 445-451.

[49] P. T. Krein, J. Bentsman, R. M. Bass, and B. L. Lesieutre, "On the use of averaging for the analysis of power electronic systems," IEEE Trans. Power Electron. , vol. 5, no. 2, pp. 182-190, Apr. 1990.

[50] A. Davoudi and J. Jatskevich, "Parasitics realization in state-space average-value modeling of PWM DC–DC converters using an equal area method," *IEEE Trans. Circuits Syst. I, Reg. Papers*, vol. 54, no. 9, pp. 1960-1967, Sept. 2007.

[51] A. Davoudi, J. Jatskevich, and P. L. Chapman, "Computer-aided dynamic characterization of fourth-order PWM DC–DC converters," *IEEE Trans. Circuits Syst. II, Exp. Briefs.*, vol. 55, no. 10, pp. 1021-1025, Oct. 2008.

[52] A. Davoudi, J. Jatskevich, and T. De Rybel, "Numerical state-space average-value modeling of PWM DC-DC converters operating in DCM and CCM," *IEEE Trans. Power Electron.*, vol. 21, no. 4, Jul. 2006.

[53] A. Davoudi, J. Jatskevich, P. L. Chapman, and A. Khaligh, "Averaged-switch modeling of fourth-order PWM DC–DC converters considering conduction losses in discontinuous mode," *IEEE Trans. Power Electron.*, vol. 22, no. 6, pp. 2410-2415, Nov. 2007.

[54] M. A. Uddin, M. A. M. Talukder, M. Hasanuzzaman, and MST. Mumtahinah, " A unified KBM method for obtaining the second approximate solution of a third order weakly non-linear differential system with strong damping and slowly varying coefficients," *Journal of Bangladesh Academy of Sci.*, vol. 35, no. 1, pp. 77-89, 2011.

[55] S. Jian and R. M. Bass, "Automated ripple analysis using KBM method [switching power convertor harmonics]," in *Ind. Electron. Control Instrum. Int. Conf.*, 1997, vol. 2, pp. 621-626.

[56] M. S. Alam, M. A. Akbar, M. Z. Islam, "A general form of Krylov–Bogoliubov–Mitropolskii method for solving nonlinear partial differential equations," *Journal of Sound and Vibration*, vol 285, no. 1-2, pp. 173-185, Jul. 2005.

[57] M. A. Sattar, "An asymptotic method for second-order critically damped nonlinear equations," *Journal of Franklin Inst.*, vol. 321, no. 2, pp. 109-113, Feb. 1986.

[58] C. E. C. Ortiz, "Circuit oriented average modeling of switching power converters," in *Power Electron. Appl. European Conf.*, 2005, pp. 1-10.

[59] J. Cai, X. Wu and Y. Li, "Comparison of multiple scales and KBM methods for strongly nonlinear oscillators with slowly varying parameters," *Mech. Research Commun.*, vol. 31, no. 5, pp. 519-524, Sept. 2004.

[60] K. L. Lian, "Derivation of a small-signal Harmonic Model for closed-loop power converters based on the state-variable sensitivity method," *IEEE Trans. Circuits Syst. I, Reg. Papers*, to be published.

[61] R. M. Bass and J. Sun, "Large-signal averaging methods under large ripple conditions [for power convertors]," in *Power Electron. Specialists Conf.*, 1998, pp. 630-632.

[62] J. Sun, W. Wu, and R. M. Bass, "Large-signal characterization of single-phase pfc circuits with different types of current control," in in *IEEE Applied Power Electron. Conf. and Exposition, '98,* pp. 655-661.

[63] B. Lin and S. Qiu, "New perturbation technique for transient analysis and its applications in DC-DC PWM switching power converters," *Journal of Electron., China*, vol. 14, no. 4, pp. 357-366, Oct. 1997.

[64] Z. Mihajlovic, B. Lehman, and C. Sun, "Output ripple analysis of switching dc-dc converters," IEEE Trans. Circuits Syst. I, Reg. Papers, vol. 51, no. 8, pp. 1596-1611, Aug. 2004.

[65] R. M. Bass and J. Sun, "Using symbolic computation for power electronics," in *Computers in Power Electron. Workshop*, 1998, pp. 1-4.

[66] N. N. Bogoliubov and Y. A. Mitropolsky, *Asymptotic methods in the theory of non-linear oscillations*, India:Hindustan publishing corp., 1961.

[67] G. C. Verghese and V. J. Thottuvelil, "Aliasing effects in PWM power converters," in Power Electron. Specialists Conf., 1999, vol. 2, pp.1043-1049.

[68] F. Wang, H. Zhang and X. Ma, "Analysis of slow-scale instability in boost PFC converter using the method of harmonic balance and floquet theory," *IEEE Trans. Circuits Syst. I, Reg. Papers*, vol. 57, no. 2, pp. 405-414, Feb. 2010.

[69] A. Demir, "Floquet theory and non-linear perturbation analysis for oscillators with differential-algebraic equations," Int. Journal of Circuit Theory Appl., vol. 28, no. 2, pp. 163-185, Mar. 2000.

[70] S. K. Mazumder, "Stability analysis of parallel DC-DC converters," *IEEE Trans. Aerosp. Electron. Syst.*, vol. 42, no. 1, pp. 50-69, Jan. 2006.

[71] P. L. Chapman, "Time-invariant, switching-frequency-dependent DC-DC converter analysis without averaging," unpublished.

[72] Y. Chen, A. Davoudi, and P. L. Chapman, "Multifrequency modeling of a multiple-input DC-DC converter," in *IEEE Power Electron. Specialists Conf.*, 2008, pp. 4604-4610.

[73] P. Midya, and K. Haddad, "Two sided latched pulse width modulation control," in *IEEE Power Electron. Specialists Conf.*, 2000, pp. 628-633.

[74] S. C. Chapra, *Applied Numerical Methods with MATLAB for Engineers and Scientists*, 2nd ed. New York: McGraw-Hii, 2008.

[75] G. C. Verghese, M. Ilic-Spong, and J. H. Lang, "Modeling and control challenges in power electronics," in *Decision and Control IEEE Conf.*, 1986, vol. 25, pp. 39-45.

[76] B. P. Lathi, *Linear Systems and Signals*, 2nd ed. New York: Oxford University Press, 2005

[77] A. Davoudi, "Parametric average value modeling of PWM DC-DC converters," M.S. thesis, Dept. Elect. Eng., Univ. British Columbia, Vancouver, Canada, 2005.

[78] Y. Chen, "Dynamic modeling of multiple-input buck-boost converters," M.S. thesis, Dept. Elect. Eng., Univ. Illinois, Urbana-Champaign, IL, 2007.

[79] A. F. Witulski and R. W. Erickson, "Extension of state-space averaging to resonant switches and beyond," *IEEE Trans. Power Electronics*, vol. 5, no. 1, pp. 98-109, Jan. 1990.

[80] A. W. Green, "Modelling a push-pull parallel resonant convertor using generalised state-space averaging," *IEE Proc.* vol. 140, no. 6, pp. 350-356, Nov. 1993.

[81] J. Xu and C.Q. Lee, "Generalized state-space averaging approach for a class of periodically switched networks," *IEEE Trans. Circuits Syst I, Fundam. Theory and Appl.*, vol. 44, no. 11, pp. 1078-1081, Nov. 1997.

[82] B. Lehman and R. M. Bass, "Switching frequency dependent averaged models for PWM DC-DC converters," *IEEE Trans. Power Electron.*, vol. 11, no. 1, pp. 89-98, Jan. 1996.

[83] A. Emadi, "Modeling and analysis of multiconverter DC power electronic systems using the generalized state-space averaging method," *IEEE Trans. Ind. Electron.*, vol. 51, no. 3, pp. 661-668, Jun. 2004.

[84] A. Emadi, "Modeling of power electronic loads in AC distribution systems using the generalized State-space averaging method," *IEEE Trans. Ind. Electron.*, vol. 51, no. 5, pp. 992-1000, Oct. 2004.

[85] J. Mahdavi, A. Emaadi, M. D. Bellar, and M. Ehsani, "Analysis of power electronic converters using the generalized state-space averaging approach," *IEEE Trans. Circuits Syst. I, Fundam. Theory Appl.*, vol. 44, no. 8, pp. 767-770, Aug. 1997.

[86] P. T. Krein, *Elements of Power Electronics*, 2nd ed. New York: Oxford University Press, 2009.

BIOGRAPHICAL INFORMATION

Lei Niu received his Bachelor of Science in Electrical Engineering with a minor in Nuclear Engineering from University of Texas at Arlington, USA, in 2010. He is currently a graduate student in Electrical Engineering Department of the same institution. His research interests include power electronics, energy conversion systems, and sustainable energy.